FRIEDRICH-SCHILLER-
UNIVERSITÄT
JENA

High-resolution x-ray spectroscopy of fast-moving ions: towards intrinsic Doppler correction

DOCTORAL THESIS

to obtain the doctoral degree of natural sciences

doctor rerum naturalium (Dr. rer. nat.)

in the subject of Physics

written by

Felix Martin Kröger

born in the Grand Duchy of Luxembourg

Friedrich-Schiller-Universität Jena

Helmholtz Insitute Jena

2025

1st evaluator : Prof. Dr. Thomas Stöhlker
(Friedrich-Schiller-Universität Jena)

2nd evaluator : Prof. Dr. Andrey Surzhykov
(Technische Universität Carolo-Wilhelmina zu Braunschweig)

3rd evaluator : Priv. Doz. Dr. Wolfgang Quint
(Ruprecht-Karls-Universität Heidelberg)

Day of thesis defence : 26.11.2025

I dedicate this work to my beloved grandfather Heinz Kröger, my beloved grandmother Christa Boguschewski, and my dear friend Marcel Kölsch.

In thankful loving memory

Abstract

This work presents a new experimental approach for precision x-ray spectroscopy of highly-charged heavy ions in a storage ring. It deploys novel metallic magnetic microcalorimeters (MMCs) at 0° and 180° on either side of the electron cooler of the recently commissioned CRYRING@ESR at the FAIR/GSI facility. These detectors of the maXs-type combine the broad spectral coverage of semiconductor detectors with an energy resolution approaching that of crystal spectrometers. The new approach represents a breakthrough in two key aspects. First, it enables the elimination of hard-to-control systematic uncertainties that are imposed on the Doppler-shift of measured x-rays, and were always hampering heavy ion storage ring experiments. Second, it achieves an energy resolution that is improved by an order of magnitude compared to semiconductor detectors, which are typically used for x-ray spectroscopy over a broad spectral range. The measurement presented in this work was conducted in 2021, and investigated N, M→L and L→K transitions of U^{90+} ions, following radiative recombination of cooler electrons into U^{91+} ions decelerated at 10.225 MeV/u. It was the first successful coincidence measurement using MMC detectors at a storage ring, and achieved an energy resolution below 100 eV FWHM for photon energies ranging from a few keV to over 100 keV. Thus, the new experimental approach enabled, for the first time, an intrinsic Doppler correction in a heavy ion storage ring experiment, decoupling the correction from the hard-to-control systematic uncertainties, which are not expected to improve in the foreseeable future. In contrast, the systematic uncertainties of the new spectroscopy technique show potential of being reduced to below 1 eV with further investigation and refinement of the approach. Despite the low photon counts in the presented measurement — owing to it being the first time uranium was injected in the CRYRING, and to it being a first that U^{91+} was decelerated to 10.225 MeV/u and stored in a storage ring — the ion beam velocity, on which the Doppler correction depends, determined through the intrinsic method yields a statistical uncertainty that is of similar magnitude than the systematic uncertainty of the conventional method (deducing the term from the electron cooler voltage). Moreover, the new experimental approach provided the first theory-supported experimental insight into relative populations of excited states, as well as the branching ratio E1/M2 of the $1s2p\,^3P_2$ state in U^{90+}.

Zusammenfassung

Diese Arbeit präsentiert einen neuen experimentellen Ansatz für Präzisions-Röntgenspektroskopie schwerer Ionen an einem Speicherring. Bei diesem kommen neuartige Magnetische Metallmikrokalorimeter (MMCs) unter 0° und 180° am Elektronenkühler des kürzlich in Betrieb genommenen CRYRING@ESR der FAIR/GSI-Anlage zum Einsatz. Jene maXs-Typ Detektoren kombinieren eine breite spektrale Akzeptanz wie die von Halbleiterdetektoren mit einem hohen Energieauflösungsvermögen nahe dem von Kristallspektrometern. Der neue Experimentansatz stellt in zwei Bereichen einen Durchbruch dar. Erstens werden systematische Unsicherheiten im Zusammenhang mit der Doppler-Verschiebung der aufgenommenen Spektren eliminiert, die Schwerionenspeicherringexperimente schon immer erschwerten. Zweitens übertrifft die durch ihn erreichbare Energieauflösung die der Halbleiterdetektoren, die typischerweise für breitbandige Röntgenspektroskopie eingesetzt werden, um fast eine Größenordnung. Die im Kontext dieser Arbeit 2021 durchgeführte Messung untersuchte $\mathrm{N}, \mathrm{M}{\rightarrow}\mathrm{L}$ und $\mathrm{L}{\rightarrow}\mathrm{K}$ Übergänge in U^{90+}-Ionen, die auf strahlende Rekombination von Kühlerelektronen mit auf 10.225 MeV/u abgebremsten U^{91+}-Ionen erfolgten. Dies war die erste erfolgreiche Koinzidenzmessung mit MMC-Detektoren an einem Speicherring, und erreichte eine Energieauflösung von weniger als 100 eV FWHM für Photonenergien von wenigen keV bis über 100 keV. Damit erlaubte der neue Experimentansatz erstmals die Durchführung einer intrinsischen Doppler-Korrektur eines Schwerionenspeicherringexperiments, was diese von den nicht genau bestimmbaren systematischen Unsicherheiten, für die in naher Zukunft keine Verbesserung zu erwarten ist, trennte. Die systematischen Unsicherheiten der neuen Methode weisen hingegen Potential auf, nach eingehender Untersuchung und Feinschliff des neuen Ansatzes, auf unter 1 eV reduziert werden zu können. Trotz der niedrigen Photonenzählrate in der hier präsentierten Messung — da erstmals Uran im CRYRING, und als U^{91+} mit einer bisher unerreicht niedrigen Energie in einem Speicherring gespeichert wurde — weist die mit der intrinsischen Methode ermittelte Ionengeschwindigkeit, von der der Doppler-Korrekturfaktor abhängt, eine statistische Unsicherheit auf, die bereits nahe der systematischen Unsicherheit der üblichen Methode liegt, die den Korrekturterm anhand der Elektronenkühlerspannung ermittelt. Darüber hinaus gewährt der neue Experimentansatz eine erste theorieunterstützte experimentelle Einsicht in die relative Bevölkerung angeregter Zustände, sowie in das Verzweigungsverhältnis E1/M2 aus dem $1s2p\,{}^3P_2$ Zustand von U^{90+}.

Contents

1. Introduction

Our state of knowledge regarding atoms has come a long way from its philosophical origins in the 5^{th} Century BCE to the various atomic models, which over time were constantly refined. This thesis aims to contribute to incrementally expanding our knowledge in the field of atomic structure, electron-ion recombination, and Quantum ElectroDynamics (QED) by means of precision x-ray spectroscopy.

Motivation and scientific context

Some of the most important iterations of atomic models in the modern era were the models of: Joseph John Thomson (1904) [1], Ernest Rutherford (1911) [2], Niels Bohr (1913) [3, 4, 5], and its extension by Arnold Sommerfeld (1915/16) [6, 7, 8], and Erwin Schrödinger (1926) [9, 10, 11, 12] (see figure 1.1 for visualisations). Through E. Rutherford's studies (experimentally carried out by Hans Geiger and Ernest Marsden [13]), we learned that an atom consists of a very small, positively charged nucleus surrounded by a much larger 'cloud' of electrons [2]. Since this discovery, the electronic structure of atoms has been the focus of interest of atomic physics, while the nucleus has become subject of a branch separating itself from atomic physics, named nuclear physics.

When British physicist Paul Dirac derived his relativistic quantum-mechanical equation in 1928, it seemed to be the long-sought solution to describe the characteristics of bound electrons. However, in 1947, Willis Eugene Lamb Jr. and Robert Curtis Retherford found a splitting in contrast to the degeneracy of the $2s_{1/2}$ and $2p_{1/2}$ states in hydrogen (H) predicted by the solution of P. Dirac's equation [15]. As summarised in [16], it was this finding, together with the discovery of the anomalous magnetic moment of the electron [17], that led to the proposal of QED as a comprehensive description of the

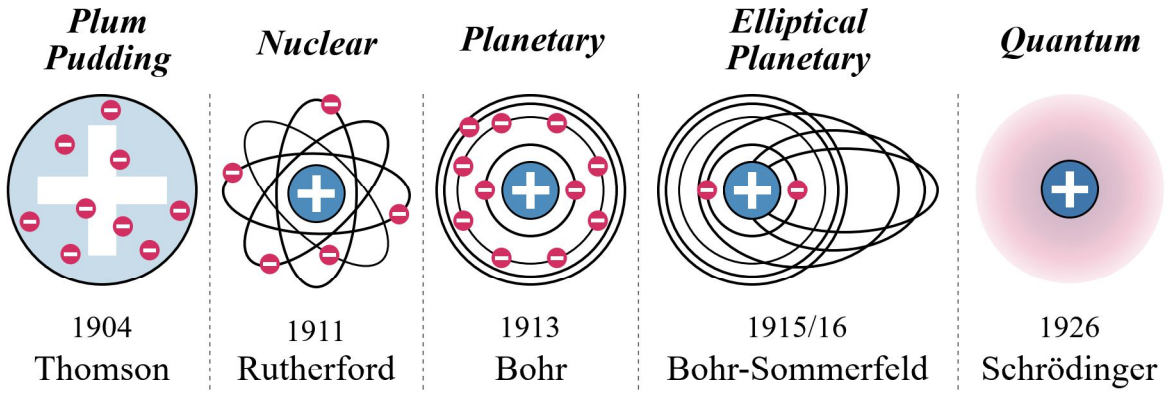

Fig. 1.1: Schematic visualisation of different atomic models, inspired by [14].

electromagnetic interaction by Hans Albrecht Bethe [18], Richard Feynman [19, 20], Julian Schwinger [21, 22, 23, 24] and Shin'ichirō Tomonaga [25, 26, 26]. This was followed up by several works of Freeman John Dyson [27, 28, 29]. In 1985, R. Feynman referred to QED as the 'jewel of physics' [30], and nowadays it is typically regarded as the best-tested quantum theory in the domain of relatively low electromagnetic field strengths, e.g. provided by low atomic number (low-Z) systems, due to the agreement with extremely precise measurements reported in e.g. [31, 32, 33, 34, 35, 36].

One of the current frontiers of atomic physics research is the study of QED in extreme electromagnetic fields. This is because experimental data are scarce in this domain [16], as they require difficult and expensive large-scale facility experiments. In this context, the investigation of heavy ions is of special interest, as their nuclei naturally provide very high-strength electromagnetic fields, surpassing field strengths achievable in high power lasers by several orders of magnitude. Figure 1.2, for example, shows a comparison of the electromagnetic field strengths at the lowest orbitals of H-like uranium (U) and the one reached by the CoReLS[1] ultra-high intensity laser, which achieved roughly $7 \cdot 10^{12}\,\frac{\mathrm{V}}{\mathrm{cm}}$ of field-strength in 2021 [37][2]. For high Z, where the parameter αZ approaches 1 ($\alpha \approx 1/137$ being the fine-structure constant), the electric field strengths experienced by the most strongly bound electrons, i.e. the K-shell electrons, are near or above the

[1]Center for Relativistic Laser Science (CoReLS) at the Gwangju Institute of Science and Technology (GIST), Cheomdangwagi-ro 123, Buk-gu, 61005 Gwangju, South Korea.

[2]Value given as peak intensity of the best focal spot: $P_\mathrm{d} = 1.4 \cdot 10^{23}\,\frac{\mathrm{W}}{\mathrm{cm}^2}$, corresponding to $E = \sqrt{377\,\Omega \cdot P_\mathrm{d}} \approx 7 \cdot 10^{12}\,\frac{\mathrm{V}}{\mathrm{cm}^2}$, the $377\,\Omega$ being the ratio of the electric and magnetic field, respectively E and H.

'Schwinger limit'[3] of $E_S = \frac{m_e^2 c^3}{e\hbar} \approx 1.32 \cdot 10^{16} \frac{V}{cm}$ (see figure 1.2), m_e denoting the electron mass, c the speed of light, e the elementary charge, and $\hbar$ the reduced Planck constant. Approaching this limit, the frequency of QED effects, e.g. spontaneous electron-positron pair production, increases noticeably. Above this limit, real particles can be created instead of virtual ones, causing a vacuum to collapse. Hence the study of the electronic structures of heavy ions allows the deduction of QED phenomena.

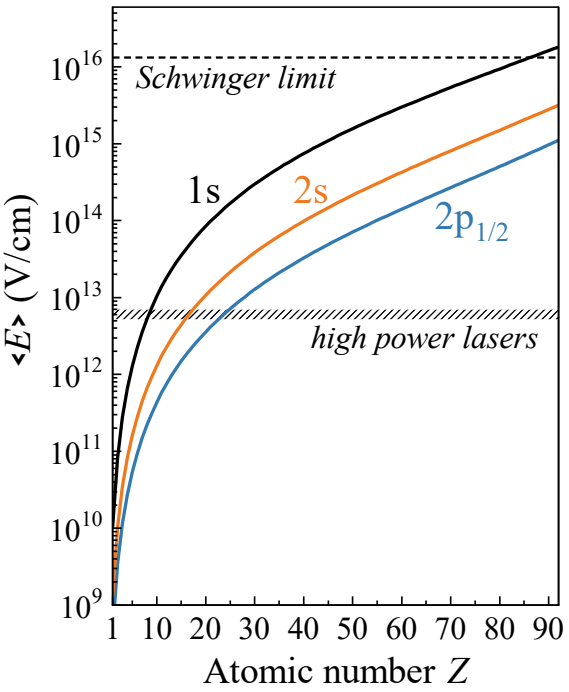

Fig. 1.2: Expectation value of the electrical field strength at the lowest orbitals of H-like ions as a function of the atomic number Z (full lines) [41]. Also shown is the field strength around which interaction between the ion and the vacuum can occur, called Schwinger limit (dashed line), the range of accessible field strength of high power lasers (hatched area), e.g. the CoReLS laser from 2021 [37].

H-like heavy ions represent the simplest systems, and helium-like (He-like) heavy ions (i.e. with two bound electrons) the simplest multi-electron systems to investigate strong-field bound-state QED effects. The latter case additionally offers the possibility to study electron-electron interactions in the presence of strong electromagnetic fields [42]. Since the strength of QED contributions scales roughly with Z^4 [43], uranium, the heaviest naturally occurring stable element, can be considered the perfect testing ground at highest field strengths to probe state-of-the-art higher-order QED calculations. This motivated the element choice of this work, which presents a spectroscopic study of

[3] In 1936, Werner Karl Heisenberg and Hans Heinrich Euler explored in [38] non-linear behaviour of a strong electromagnetic-field in a vacuum, discussing the formation of matter out of energy in vacuum, or if the energy is not sufficient, the polarisation of the vacuum by virtual particles. In 1951, J. Schwinger developed the corresponding field strength limit, above which an electromagnetic-field interacts with the vacuum [39], or, in other words, where the vacuum can literally be brought 'to a boil' [40].

He-like uranium (U^{90+}).

Information about the atomic structure and dynamics of few-electron heavy ions is commonly accessed experimentally via x-ray spectroscopy of characteristic transitions. Such heavy ion experiments are typically conducted at storage rings of accelerator facilities, as only those provide the most heavy few electron ions in high enough numbers, compared to e.g. Electron Beam Ion Traps (EBITs)(see e.g. [44]). At these large-scale facilities, intense beams of heavy ions are prepared in a specific charge state and electronic configuration by means of charge-changing collisions with stationary stripper foils and/or dedicated gas targets, and/or through in-flight recombination with free electrons at electron coolers[4].

In precision spectroscopy experiments of fast-moving emitters (e.g. ions in a storage ring), it is crucial to precisely correct for shifts in the energy of measured photons, caused by the Doppler effect[5]. Only then it is possible to deduce the energy which the emitted photons had in the emitter frame, from the energy values, measured in the laboratory frame at a certain observation angle. The uncertainty of the Doppler correction depends on the exact knowledge of the ion beam velocity and the geometric alignment of the detector with the ion beam (i.e. the observation angle). However, usually there is only one method available to precisely determine the ion beam velocity in case of highly-charged heavy ion storage ring experiments. The conventional method deduces the ion velocity, and hence the velocity-dependent Doppler factor, from an estimate of the acceleration voltage experienced by the electrons of an electron cooler. The issue is, that this introduces a systematic uncertainty for which an improvement is not to be expected in the foreseeable future. The other dependency of the Doppler correction is the exact knowledge of the observation angle. While the related systematic uncertainty could be minimised by using observation angles of 0° or 180°, typically, the view ports and space around storage rings are defined during their design, so the available experimental angles are limited (worldwide, rings for heavy ion x-ray spectroscopy are scarce). A later change is costly and operation-disrupting, and therefore rare (typically, new large scale experiment opportunities arise only by redesign (e.g.

[4]An electron cooler is an instrument of a storage ring, and will be explained in detail in section 3.4.
[5]The phenomenon of an observed shift in wave frequency due to relative motion between the emitting wave source and the observing system is named after Christian Doppler, who described it in 1842 [45].

Conseil Européen pour la Recherche Nucléaire (CERN)[6]) or new facility conceptions (see the 'Facility for Antiproton and Ion Research in Europe' (FAIR) below). Therefore, the additional method-inherent uncertainty had to be accepted in x-ray spectroscopy experiments in the past. For the past decades, the combination of these two hard-to-control systematic uncertainties (linked to the voltage-dependent velocity determination and the observation angle) was one of the main bottlenecks of this kind of experiment.

Another issue was the shortcomings of established x-ray spectroscopy techniques in terms of the detector energy resolution or insufficient spectral range coverage. In heavy ion x-ray spectroscopy, the most used detector family is that of semiconductor detectors. Among other things, they provide a broad spectral range. However, at photon energies relevant to K shell transitions in heavy ions (up to roughly 100 keV), their energy resolution is limited down to a few hundred eV Full Width at Half Maximum (FWHM). In contrast, crystal spectrometers achieve far superior energy resolutions (of just a few eV, e.g. [46], or even less than 1 eV [47, 48]), but are limited in their spectral range, making them solutions for only very specific applications. Also their working principle necessitates precise knowledge and stability of the geometry of the experimental setup, which can be impracticable to achieve for non-permanent setups at storage rings.

To carry out the measurement for the work presented in this thesis, a new experimental approach was used to overcome the limitations caused by the hard-to-control systematics and the shortcomings in terms of detector energy resolution. For the experiment, novel Metallic Magnetic microCalorimeter (MMC) detectors were deployed [49]. These have been developed within the Stored Particles Atomic physics Research Collaboration (SPARC) [50], and were specifically tailored to perform precision x-ray spectroscopy of highly-charged heavy ions. They combine a high resolution comparable to those achievable with crystal spectrometers with the broad spectral range of semiconductor detectors. Moreover, the experiment used a coincidence measurement technique, which has not been previously done with these types of detectors, allowing efficient reduction of background radiation. The measurement took advantage of the excellent x-ray spectroscopy conditions provided by the newly available experimental environment of

[6]At CERN, the Large Electron–Positron collider (LEP) was decommissioned in 2000, and replaced by the Large Hadron Collider (LHC).

FAIR[7]: the CRYRING@ESR[8]. This newly commissioned storage ring allows positioning of the detectors at 0° and 180° around the electron cooler, which minimises the systematic uncertainty linked to the detection-setup geometry.

Thesis focus

The goal of this work is to utilise novel MMC detectors in a first dedicated high precision measurement. Exploiting their unique combination of high bandwidth, energy resolution and fast signal rise time, and taking advantage of the new experimental environment provided by the CRYRING@ESR, allows to conduct the first ever intrinsic Doppler-correction in an x-ray spectroscopy storage ring experiment. This eliminates the biggest source of systematic uncertainty, which is hard to control and not expected to improve in accelerator-driven spectroscopy research in the foreseeable future. Moreover, this work presents two studies, enabled by the new experimental approach. They allow first insights into relative state populations and transition behaviours in He-like uranium through investigation of $\mathrm{N, M \rightarrow L}$ and $\mathrm{L \rightarrow K}$ transition spectra with state-of-the-art resolution. The results show that the here presented approach allows to overcome former limitations, bringing atomic physics research one step closer to the 1 eV threshold required to probe 2nd order QED effects in the heaviest atomic systems.

Thesis structure

Chapter 2 presents the theoretical background of the motivation by providing an overview of the development of the ideas of electronic structure, their theoretical treatment, including bound-state QED and nuclear processes in few-electron heavy ions, and the corresponding corrections to the binding energies. Chapter 3 describes the physical basics relevant for heavy ion x-ray spectroscopy, starting from theoretical aspects on photon emission and absorption, x-ray detection, the beam production and cooling mechanism at storage rings with the related radiative recombination and cascades of electrons in stored ions, the Doppler shift and the spectral line profile. Chapter 4

[7]FAIR uses parts of the 'Gesellschaft für SchwerIonenforschung' (German for 'society for heavy ion research') (GSI) facility for the beam production. Both facilities share the same facility site and therefore address: GSI/FAIR, Planckstraße 1, 64291 Darmstadt, Germany.

[8]A storage ring named after its original accelerator facility in Stockholm, that contained among other things a CRYogenic electron-beam ion source and this storage RING (CRYRING) [51], that was brought to GSI as Swedish in-kind contribution to FAIR and connected to GSI's 'ExperimentierSpeicherRing' (German for 'experimental storage ring') (ESR).

establishes a picture of the recent status in this experimental field by providing a description of recent heavy ion x-ray spectroscopy experiments conducted at GSI. First, the facility, including beam guidance and beam lifetime, as well as the ESR storage ring used in the previous experiments are discussed. Next, the most recent measurements on He-like uranium at two different ESR experiment positions are presented: at its electron cooler and gas target. Chapter 5 presents the new experimental approach, and its first application for a spectroscopic measurement of He-like uranium conducted in 2021 at the CRYRING@ESR storage ring of the FAIR facility. The chapter starts with a description of the experimental environment at FAIR. Then follows a section which describes the experimental setup used in the measurement. Then, it concludes with a detailed discussion regarding the experiment's beam time, raw data analysis, resulting photon spectra, and a comparison of the latter with a spectrum of a previous measurement, which was conducted with a semiconductor detector at the ESR storage ring at the GSI. Finally, in chapter 6, details on the data analysis and a discussion of the results are presented. The first result section discusses the experimental findings regarding the ion beam velocity, and hence the Doppler factor. The sections that follow present first theory-supported experimental insights into: i) relative M, N shell populations, allowing to test a theoretical model for RR into excited states and the subsequent electron cascades, and ii) the branching ratio of the $2p_{3/2}$ $^3P_2$ state, enabling a first verification of a theoretical prediction for a heavy He-like system. Finally, chapter 7 summarises the thesis' findings and provides an outlook on future activities based on the results.

2. Electronic structure of H- and He-like heavy ions

This chapter presents the development and current state-of-the-art theoretical determination of the electron binding energy and the treatment of QED and nuclear effects. It ends on a short discussion on the spectroscopic investigation of QED effects in H- and He-like heavy ions, presenting the influence of the presence of a second electron on the electronic structure and dynamics, and their research status.

2.1 From Rydberg's formula to Dirac's theory

The electronic structure of atomic systems can be investigated by means of photon spectroscopy. Already in the 1500's, alchemists knew that different salts provide differently coloured flames when burned [52]. However, a first theoretical understanding of the structure of emission lines was only gained through the works of Johann Jakob Balmer in 1885 [53] and Johannes Robert Rydberg in 1889/1890 [54, 55], investigating detected spectra. Building on the work of J. J. Balmer, regarding finding an expression to calculate the wavelength λ for hydrogen, J. R. Rydberg found a generalised formula for all spectral lines presented in:

$$\pm\frac{n}{N_0} = \frac{1}{(m_1+\mu_1)^2} - \frac{1}{(m_2+\mu_2)^2}, \tag{1}$$

with $n = \frac{1}{\lambda}$ being the wave number per unit distance, which is the inverse of the wave length and proportional to the frequency, $N_0 = 109721.6\,\mathrm{cm}^{-1}$ an empirical constant that is same for all series [55], equivalent to the later called Rydberg constant, m_1 and m_2 denoting variable integers, and μ_1 and μ_2 constants which are characteristic for a

series. Since at that time, neither the electron nor the general structure of atoms was discovered, it was not possible to address the physical basis of the emission line patterns described by the Rydberg formula. As comprehensively summarised in [56], Richard Laming hypothesised conceptually that chemical properties of atoms are determined by an indivisible quantity of electric charge, which he elaborated on in his publications between 1838 and 1851, e.g. in [57]. Yet, the electron itself was only discovered in 1897 by J. J. Thomson [58], who then published his atomic model in 1904 [1], describing an atom to be constituted of a number of negatively charged electrons within a positively charged sphere (illustrated in figure 1.1). As later explained by N. Bohr in his book [59], Walter Ritz addressed a physical explanation of the atomic origin of the spectral laws, ascribing them to 'atomic magnetic fields' interacting with the atom's electrons [60]. Though his explanation did not arrive at a sufficient interpretation, he also presented a general law, later known as the 'Rydberg-Ritz combination principle', which, based on J. R. Rydberg's formula, allows finding the wave number of a new spectral line by adding up or deducting the wave numbers of two other spectral lines. This law made it possible to successfully predict several spectral lines. However, soon after, in 1911, a new epoch in the development of atomic structure ideas began with the discovery of the atomic nucleus by E. Rutherford and the publication of his atomic model [2], describing atoms to consist of a positively charged nucleus, surrounded by negatively charged electrons (illustrated in figure 1.1).

In E. Rutherford's working group, N. Bohr continued the study of the Rutherford atomic model, and soon came up with his own model, published in 1913 in his famous trilogy 'On the constitution of atoms and molecules' [3, 4, 5] (see [61] for a summary). According to N. Bohr's later assistant and collaborator Léon Rosenfeld (working with N. Bohr between 1930-1962), N. Bohr had recalled later in life, that when he came across the work of J. R. Rydberg treating the Balmer formula, things fell into place for him, as reported in [62]: *"As soon as I saw Balmer's formula", he told me more than once, "the whole thing was immediately clear to me".*

Similar to the work of John William Nicholson in 1912 [63], the Bohr atomic model used a quantisation to explain the spectral phenomena. However, N. Bohr's was the first atomic model relating the emitted radiation to the transition of electrons from electron states defined as 'orbits' (not to be confused with orbitals), by doing, as N. Bohr called it, 'quantum-jumps' to another level. As a general formula for all series of hydrogen,

his planetary model described the frequency of emitted light to be determined by:

$$\nu = \underbrace{\frac{2\pi^2 m_\mathrm{e} e^4}{h^3}}_{=:R\cdot c} \left(\frac{1}{\tau_2^2} - \frac{1}{\tau_1^2} \right), \tag{2}$$

with m_e being the electron mass, e the elementary charge, h the Planck constant, and τ_i respective electron orbit states, also known as quantum number n of the respective energy level. Thus, he found an expression for the, up to this time, empirically chosen Rydberg constant R and Rydberg frequency, which was observed to be $f_\mathrm{R} = R \cdot c \approx 3.29 \cdot 10^{15}\,\mathrm{s}^{-1}$. When he calculated the Rydberg frequency with his expression, it yielded $\approx 3.1 \cdot 10^{15}\,\mathrm{s}^{-1}$, which was in the experimental uncertainty of the constants used for his calculation [3]. With that, N. Bohr provided an atomic model which described the electronic structure around a nucleus (illustrated in figure 1.1), thereby extending on the Rutherford atomic model, while being coherent with the radiation laws established by J. J. Balmer and J. R. Rydberg.

In 1915/1916, A. Sommerfeld implemented special relativity into N. Bohr's model of hydrogen, and included the azimuthal quantum number, introduced by Hendrik Lorentz and Albert Einstein, as shown in [64]. His contribution allowed the description of the so-called 'fine structure splitting' phenomenon of hydrogen, and proposed that electron paths in N. Bohr's planetary atomic model can be elliptic, resulting in the Bohr-Sommerfeld atomic model [6, 7, 8] (illustrated in figure 1.1). However, despite the great success of this model, two shortcomings became evident shortly after its publication, namely that there was no theoretical foundation for the ad-hoc assumption of non-radiating, quantised electron orbits, which contradicts classical electromagnetism, as well as a soon-to-be-discovered property of the electron, the spin. However, all of these ideas were brought together through the introduction of quantum mechanics.

The development of quantum mechanics was preceded by many problems stemming from mostly two issues: the wave property of electrons, and/or their spin. As summarised in [64, 65], without awareness and knowledge of the latter, e.g. E. Schrödinger rejected his wave equation which he first derived in the relativistic form, since without the electron spin, the non-relativistic approach seemed to provide better results. In the end, E. Schrödinger published his non-relativistic wave equation and established quantum mechanics in several works in 1926 [9, 10, 11, 12]. From this, in 1926, various physicists

including Oskar Klein, and Walter Gordon, Vladimir Fock, Louis De Broglie, Wolfgang Ernst Pauli, and Frans H. van den Dungen and Théophile de Donder, independently derived the relativistic form of E. Schrödinger's equation (for more information see [64]), which he previously discarded, today known as Klein-Gordon equation [66, 67], applicable to describe the kinematics of spin-zero particles. Around the same time as E. Schrödinger, George Uhlenbeck and Samuel Goudsmit published a visual model of the spinning electron in [68]. With that, the search began for a combined quantum mechanical wave equation for a spinning electron. For the non-relativistic electron, in 1927 Charles Galton Darwin [69], and Wolfgang Ernst Pauli [70] found a wave equation, followed by the examination of the relativistic case by Hendrik Anthony Kramers, Pascual Jordan, Eugene Wigner,Yakov Frenkel, Dmitri Ivanenko, and Lev Landau (for more information see [64]). However, before they succeeded, in 1928 P. Dirac arrived at the equation [71]. His quantum mechanical theory allowed to describe, among other things, the interaction of a charged particle with an electromagnetic field, also including relativistic effects, and provided a consistent treatment of the electron spin. Assuming the source of the electromagnetic field to be a point-like infinitely heavy nucleus, the solution of his equation delivers for an electron bound to its nucleus the total energy:

$$E_{n,\kappa}^{\mathrm{Dirac}} = m_{\mathrm{e}}c^2 \sqrt{1 + \frac{(\alpha Z)^2}{\left(n - (|\kappa| + \sqrt{\kappa^2 - (\alpha Z)^2}\right)^2}}^{-1}, \tag{3}$$

with n being the principal quantum number, and κ the angular momentum-parity quantum number with $\kappa = l + 1$ when $\kappa < 0$, and $\kappa = l$ when $\kappa > 0$, where l is the angular momentum [16]. Thus follows for the Dirac point-nucleus binding energy of an electron in a H-like atom (see e.g. formula 17.1 in [72]):

$$E_{n,\kappa,\mathrm{bin}}^{\mathrm{Dirac}} = E_{n,\kappa}^{\mathrm{Dirac}} - m_{\mathrm{e}}c^2, \tag{4}$$

2.2 Bound-state QED and nuclear effects on the binding energy

However, as first experimentally observed by Willis Eugene Lamb Jr. and Robert Curtis Retherford in 1947 [15], there was a deviation from the theoretical prediction, described in detail in the series of publications [73, 74, 75, 76]. In their experiment, they

created hydrogen atoms in the excited meta-stable $2p_{1/2}$ state through electron impact ionisation. Then they exposed these hydrogen atoms to static microwave radiation, adjusted with an electromagnetic field, thus exciting the $2p_{1/2}$ electrons to anomalous Zeeman-splitted $2p_{3/2}$ states. When hitting a resonant frequency, the measured current of $2p_{1/2}$ dropped. Thus, they found that the $2s_{1/2}$ state was about $f = 1000\,\mathrm{MHz}$[1] higher than the $2p_{1/2}$ state, instead of degenerated, as expected by the Dirac solution. This deviation from the solution of P. Dirac's equation with the assumptions described in section 2.1 became known as the Lamb shift (LS), later found to be caused by QED and nuclear effects[2]. When taking into account these effects, the electron binding energy of a H-like system becomes (see e.g. [77]):

$$E_{n,\kappa,\mathrm{bin}}(Z) = E^{\mathrm{Dirac}}_{n,\kappa,\mathrm{bin}}(Z) + E^{\mathrm{LS}}_{n,\kappa}(Z). \tag{5}$$

For a hydrogen-like system, assuming that the description of QED and nuclear structure is complete, so that the Standard Model describes all relevant effects comprehensively, follows the current description [16]:

$$\begin{aligned} E_{n,\kappa,\mathrm{bin}}(Z,A) = {} & E^{\mathrm{Dirac}}_{n,\kappa,\mathrm{bin}}(Z) \\ & + E^{\mathrm{QED(1)}}_{n,\kappa}(Z) \\ & + E^{\mathrm{QED(2)}}_{n,\kappa}(Z) \\ & + E^{\mathrm{QED(O>2)}}_{n,\kappa}(Z) \\ & + E^{\mathrm{Nuc}}_{n,\kappa}(Z,A) \\ & + E^{\mathrm{Rec}}_{n,\kappa}(Z,A) \\ & + \underbrace{\mathrm{X}}_{=0\ (?)}\ , \end{aligned} \tag{6}$$

with $E_{n,\kappa}(Z,A)$ describing a bound electron energy level, being composed first of all by $E^{\mathrm{Dirac}}_{n,\kappa}(Z)$ denoting the Dirac energy, and the following corrections terms: $E^{\mathrm{QED(1)}}_{n,\kappa}(Z)$ for the first-order QED effects, $E^{\mathrm{QED(2)}}_{n,\kappa}(Z)$ for the second-order QED effects, and $E^{\mathrm{QED(O>2)}}_{n,\kappa}(Z)$ for QED effects of the orders higher than 2. Note that, in view of the current state of QED investigations, QED terms of higher order than 2 are only relevant

[1] In [76] refined to 1058.27 MHz for H: $E = h \cdot f \approx 4.14 \cdot 10^{-15}\,\mathrm{eV\ s} \cdot 1058.27\,\mathrm{MHz} = 4.38\,\mu\mathrm{eV}$.

[2] Note that in literature the Lamb shift is sometimes just referring to QED effects, since the nuclear effects are only relevant for high-Z systems, while for low-Z systems they are negligible small compared to the other contributions, i.e. for hydrogen as used in the experiment of Lamb and Retherford. However, in this work, it refers to both: QED and nuclear effects.

for $Z \leqslant 10$ (see [77]), and are therefore not further discussed as this work focuses on He-like uranium. Finally, $E^{\mathrm{Nuc}}_{n,\kappa}(Z, A)$ describes corrections for the nuclear effects, and $E^{\mathrm{Rec}}_{n,\kappa}(Z, A)$ for the recoil effects. The 'X' is assumed to be zero if the Standard Model is correct. However, if in the far future a complete description of QED and nuclear structure should not only be assumed but achieved, any deviation measured from known terms, also of higher order than shown, would indicate an existence of 'new Physics beyond the Standard Model'. This, however, would presuppose the measurement of a difference beyond the experimental and theoretical uncertainties of the mentioned QED and nuclear contributions, as well as of terms of higher orders. At the moment, the technological and scientific challenge is still to achieve an experimental sensitivity for the second order QED effects and their uncertainties.

In the following section, the correction terms will be discussed in detail, divided in QED and nuclear effects. Note that the explanations of the Lamb shift that follow are based on the descriptions in the publication of Paul Indelicato [16] from 2019. His work provides a detailed overview of the development and current state of theories and experiments regarding the description, and the investigation of the Lamb shift in highly-charged heavy ions.

First order one-electron QED correction terms

The first-order QED effects can be divided into two processes (illustrated in figure 2.1).

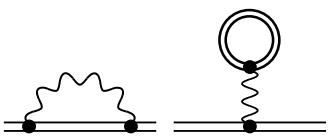

Fig. 2.1: Feynman diagrams of first-order one-electron QED effects: left) self-energy, right) vacuum polarisation, inspired by [16].

The self-energy accounts for a shift in the electron binding energy, due to constant emittance and absorption of virtual photons in and from the vacuum. As described qualitatively in [78], the virtual photon interactions result in an oscillatory motion of the electron on its bound path. This jitter has as a consequence, that for the electron, the effective nuclear potential is slightly smeared, effectively differing from the actual one, reducing the electron's binding energy. This effect is stronger the smaller the distance is between bound electron and nucleus. As summarised in [16], the evaluation to all orders of $Z\alpha$ for self-energy is based on [79, 80]. For the 1s

level at medium and high-Z, the first high-precision evaluation of the self-energy was performed by Peter J. Mohr [81, 82]. An extension to super-heavy elements was done by Kwok-Tsang Cheng and Walter R. Johnson [83], and the evaluation for different n, l, j levels other than the 1s level was the subject of numerous works [84, 85, 86, 87, 88].

The vacuum polarisation considers the difference in nuclear field-strength experienced by an electron and hence a shift in the electron binding energy, due to nuclear field induced spontaneous electron-positron-pair fluctuations. As described qualitatively in [78], their creation and subsequent annihilation in the vacuum generates a dielectric medium, and thus leads to a polarisation of the vacuum (see [89]). This medium increases the nucleus potential for close-by electrons (increasing their binding energies), while screening it for those further away. The vacuum polarisation can be determined by an expansion in $Z\alpha$, and then treated in two parts (see [77]). The dominant part can be treated according to [89], considering the electron-positron-pair to the leading order in $Z\alpha$, and the remaining part in all $(Z\alpha)^n$, for $n \geqslant 3$, according to [90]. Note that according to the Furry theorem [91] terms where n is even do not contribute.

The sum of the first-order QED corrections $E_{n,\kappa}^{\mathrm{QED}(1)}(Z)$ is given by:

$$E_{n,\kappa}^{\mathrm{QED}(1)}(Z) = \frac{\alpha}{\pi}\frac{(\alpha Z)^4}{n^3}F_{n,\kappa}^{(1)}(\alpha Z)m_e c^2, \tag{7}$$

with $F_{n,\kappa,Z}^{(1)}(\alpha Z)$ being a slowly varying function of αZ, for which the lowest-order contribution can be evaluated as done in e.g. [92, 93].

A treatment of this correction term by a low-Z approximation is presented in [18] and in the 2010 CODATA paper [94].

Second order one-electron QED correction terms

Contrary to light systems, the second order QED effects become more important in heavier systems. Those effects are composed of different constellations, of SE and VP effects (see figure 2.2 for some examples).

The sum of the second-order QED corrections $E_{n,\kappa}^{\mathrm{QED}(2)}(Z)$ includes all of those two-loop

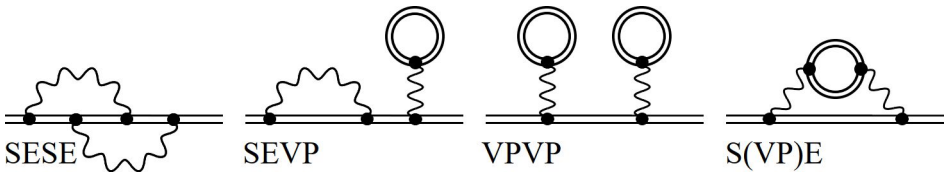

Fig. 2.2: Examples of Feynman diagrams for second-order one-electron QED effects, inspired by [77].

corrections, and is given by:

$$E_{n,\kappa}^{\mathrm{QED}(2)}(Z) = \left(\frac{\alpha}{\pi}\right)^2 \frac{(\alpha Z)^4}{n^3} F_{n,\kappa}^{(2)}(\alpha Z) m_e c^2, \tag{8}$$

Similar to $F_{n,\kappa}^{(1)}(\alpha Z)$, $F_{n,\kappa}^{(2)}(\alpha Z)$ is also a slowly varying function of αZ, for which the lowest-order contribution can be evaluated as done for SE in e.g. [95, 96].

Compared to the first-order QED effects, the various second-order QED diagrams, seen in figure 2.2, are not evaluated to that same degree yet. The full SESE contribution calculation for the 1s state and high-Z elements was also performed by Vladimir A. Yerokhin et al. [97]. A few years later, V. A. Yerokhin et al. evaluated the SEVP, VPVP, and S(VP)E contributions for the 1s, 2s, $2p_{1/2}$ and $2p_{3/2}$ levels for $1 \leqslant Z \leqslant 100$ [98].

Nuclear corrections

Besides first- and second-order QED effects, effects related to the properties of the nucleus also have to be taken into account, represented in eq. 6 by $E_{n,\kappa}^{\mathrm{Nuc}}(Z, A)$, which is composed of four effects:

$$E_{n,\kappa}^{\mathrm{Nuc}}(Z, A) = E_{n,\kappa}^{\mathrm{Vol}}(Z, r_{\mathrm{RMS}}) + E_{n,\kappa}^{\mathrm{Sha}}(Z, A) + E_{n,\kappa}^{\mathrm{Def}}(Z, A) + E_{n,\kappa}^{\mathrm{Pol}}(Z, A), \tag{9}$$

with $E_{n,\kappa}^{\mathrm{Vol}}(Z, r_{\mathrm{RMS}})$ representing the nuclear volume correction, $E_{n,\kappa}^{\mathrm{Sha}}(Z, A)$ the nuclear shape correction, $E_{n,\kappa}^{\mathrm{Def}}(Z, A)$ the nuclear deformation correction, and $E_{n,\kappa}^{\mathrm{Pol}}(Z, A)$ the nuclear polarisation correction term.

The first term $E_{n,\kappa}^{\mathrm{Vol}}(Z, r_{\mathrm{RMS}})$ in the nuclear correction formula 9 takes into account that the nucleus is of finite size, instead of point-like, as assumed in equation 3. To determine this effect, calculations usually use available compilations for the radii, originating from findings from experiments with muonic atoms, electron scattering, and atomic x-ray or

laser spectroscopy [99, 100]. Note that in the literature, the nuclear radii r_{Nuc} are often given in form of the nuclear root mean square-radius (RMS), which translates into the following [101]:

$$r_{\mathrm{h.d.}}^2 = \frac{5}{3} r_{\mathrm{RMS}}^2 - \frac{7}{3} a^2 \pi^2, \tag{10}$$

where $r_{\mathrm{h.d.}}$ describes the half-density radius, a describes the diffuseness parameter, which is a constant calculated from the surface thickness parameter $t = 4 \cdot \ln(3) \cdot a$, at which the nuclear potential has decreased from 90% to 10%.

The second term $E_{n,\kappa}^{\mathrm{Sha}}(Z, A)$ in formula 9 accounts for the actual shape of the nucleus, employing widely used charge distribution models, like e.g. the two-parameter Fermi-model for the spacial distribution:

$$\rho(r) = \frac{\rho_0}{1 + e^{\frac{(r - r_{\mathrm{h.d.}})}{a}}}, \tag{11}$$

where ρ_0 is a normalisation constant, and the shape is defined by the above mentioned half-density radius $r_{\mathrm{h.d.}}$, and diffuseness parameter a. For an improved description of the nuclear charge density distribution the following models have been used: the Sum Of Gaussians (SOG) in [102] and Fourier-Bessel in [103, 104].

The third term $E_{n,\kappa}^{\mathrm{Def}}(Z, A)$ in formula 9 considers the influence of the nuclear deformation, which also uses the Fermi-model (11), however, it replaces the half-density radius parameter $r_{\mathrm{h.d.}}$ with $r_{\mathrm{h.d.}}(1 + \beta_2 Y_{20}(\theta, \phi) + \beta_4 Y_{40}(\theta, \phi))$, where β_2 is the quadrupole and β_4 the hexadecapole deformation parameters, and Y_{lm_l} denotes a spherical harmonic. This replacement provides an effective, angular-dependent charge distribution, which is then averaged over all directions in order to determine either an average charge distribution, or higher-order multipole distributions, as explained in [105]. The values for the β parameters come from different experimental findings, e.g. [106, 107, 108]. For ^{238}U the charge distribution cannot have nuclear moments beyond the monopole term, as the nuclear spin is zero. Therefore Steven A. Blundell et al. [109] performed a spherical average of the charge distribution, and a general formalism for this effect was later provided by Yury S. Kozhedub et al. [110].

The fourth and last term $E_{n,\kappa}^{\mathrm{Pol}}(Z, A)$ in formula 9 covers the nuclear polarisation. It takes into account that, in highly charged ions, the nucleus interacts with bound electrons, especially when it is in the $1s$ state, leading to a perturbation of the nucleus, resulting

in a small change of the nuclear charge distribution [16]. The evaluation of this effect is difficult as it is necessary to have information on the internal nuclear structure, e.g. on the excited states, and so on. Evaluations of the nuclear polarisation in lead and uranium can be found in [111, 112].

The final correction term to the Dirac energy $E^{\mathrm{Rec}}_{n,\kappa}(Z, M_{A,Z})$ in formula 6 takes the nuclear recoil into account. This correction considers that the nucleus is not infinitely heavy, as assumed previously, but the nucleus has instead a finite mass $M_{A,Z}$. At the lowest order, the nuclear recoil of a one-electron ion is treated, as explained in [113, 114, 115], by replacing formula 3 with:

$$E^{\mathrm{Dirac}}_{A,Z} = \left(\frac{M_{A,Z}}{M_{A,Z} + m_e} - 1\right) \cdot \left(E^{\mathrm{Dirac}}_{n,\kappa}(Z) - m_e c^2\right) \tag{12}$$

and adding the relativistic reduced mass correction:

$$E^{(1)}_{n,A,Z} = -\frac{(\alpha Z)^4}{8n^4}\frac{m_e}{M_{A,Z}} m_e c^2. \tag{13}$$

Two-electron systems

Due to the second electron, a He-like system is a complex three-body problem. To calculate the energy levels of such a system, first of all, the one-body energies calculated with formula 3 can be added for each individual electron. In addition, electron-electron interaction has to be taken into account, as well as corresponding QED corrections, described in detail in [16]. The method to consider the electron-electron interaction differs for low-Z and high-Z ions. For heavy ions, where the nucleus-electron interaction strongly dominates, a treatment is discussed e.g. in [116, 117, 118, 119].

First-order two-electron QED corrections

The corrections to the binding energy discussed for H-like systems can also be applied to He-like ions. To the first order, besides the VP and SE corrections, also the one-photon exchange correction (illustrated in figure 2.3) has to be taken into account and should be calculated in the rigorous QED formalism. A method to treat the one-photon exchange correction can be found in [120, 121].

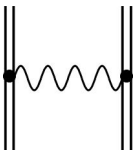

Fig. 2.3: Feynman diagram of the one-photon exchange.

Second-order two-electron QED corrections

When it comes to second order QED effects, the second electron in a He-like system adds constellations including the one-photon exchange. Figure 2.4 shows two examples for the two-photon exchange (also referred to as the non-radiative QED part [119]), the screened self-energy and the screened vacuum-polarisation, respectively. A method to treat these second-order QED corrections is discussed in great detail in [116, 119].

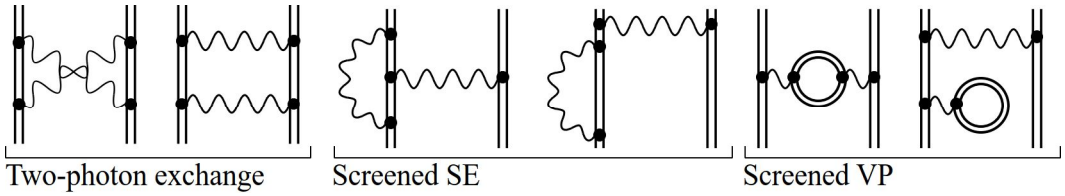

Fig. 2.4: Feynman diagrams of second-order two-electron QED effects, composed of different constellations of the first order QED effects. From left to right, two example diagrams are corresponding to: the two-photon exchange, the screened self-energy and the screened vacuum-polarisation, respectively. The figure is inspired by [116].

2.3 Spectroscopic interest in H- and He-like heavy ions

The influence of QED effects scales with the field strength, so it is strongest for heavy ions, with an approximated scaling of Z^4 (see table 2.1 and [43]). Therefore, highly-charged heavy ions are ideal test beds for the investigation of strong-field bound state QED effects. This is typically done through x-ray spectroscopy experiments, studying the electronic level structure and electronic dynamics (transition behaviours) of heavy ions. The experiment presented in this work investigated the N, M→L and L→K transitions of He-like uranium (for details see chapter 5). Compared to H-like systems, the second electron in He-like systems induces electron-electron interaction in addition to electron-nucleus interaction, changing the electronic structure and therewith the electronic transition behaviour. Table 2.2 presents theoretical predictions for the mentioned electron-electron interaction, together with predictions for the ionisation potential and contributions due to bound-state QED and nuclear effects for the ground-

state of He-like uranium, to provide an overview of the relative magnitude of these different contributions to the ionisation potential (and hence binding energy).

Table 2.1: Approximate Z-scaling behaviours of different physical properties [43].

Physical property	Scaling behaviour
Atomic radius	Z^{-1}
Ionisation potential	Z^2
Transition energy	Z^2
Lamb shift	Z^4
Fine-structure splitting	Z^4
Hyperfine splitting	Z^3

Table 2.2: One- and two-electron ionisation potential contributions and corresponding corrections for the ground-state of He-like uranium in eV, inspired by [122].

One-electron contributions		Two-electron contributions	
Dirac	-132279.92 [121]		
		1st order non-QED e-e-interaction[a]	+2265.87 [119]
		2nd order non-QED e-e-interaction[b]	-14.16 [119]
Self-energy	+355.05 [121]	Two-photon exchange	+1.30 [119]
Vacuum polarisation	-88.60 [121]	Screened SE+Screened VP	-7.10 [119]
Nuclear size	+198.81 [121]		
2nd order QED	-1.57 [121]		
Nuclear recoil	+0.46 [121]		
Nuclear polarisation	-0.20 [121]		

[a]This value was calculated using Relativistic Many-Body Perturbation Theory (RMBPT).
[b]This value was calculated using RMBPT including two Breit interactions but no retardation.

Figure 2.5 shows the electronic level structure of H-like and He-like uranium. In this figure, it becomes evident that their level structures are contrasted. Indeed, for each L shell state of the H-like system, two close-by energy states exist for the He-like system. These close-by states depend on the total angular momentum J (defined for multi-electron low-Z systems through LS-coupling and high-Z systems through jj-coupling) of the two electrons, as well as their respective spins (defining the multiplicity $M = 2S + 1$). Note that in this work, the electronic states are named according to the notation of the electronic configuration and the respective term symbol ${}^{M}L_{J}$.

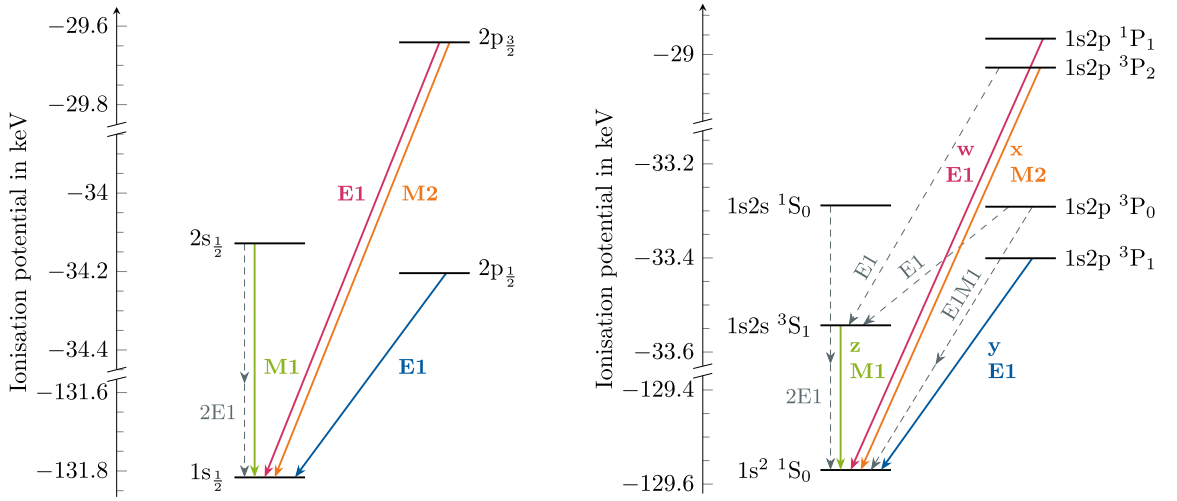

Fig. 2.5: Theoretical level scheme of the ionisation potentials of: left) H-like uranium [77], right) He-like uranium [118].

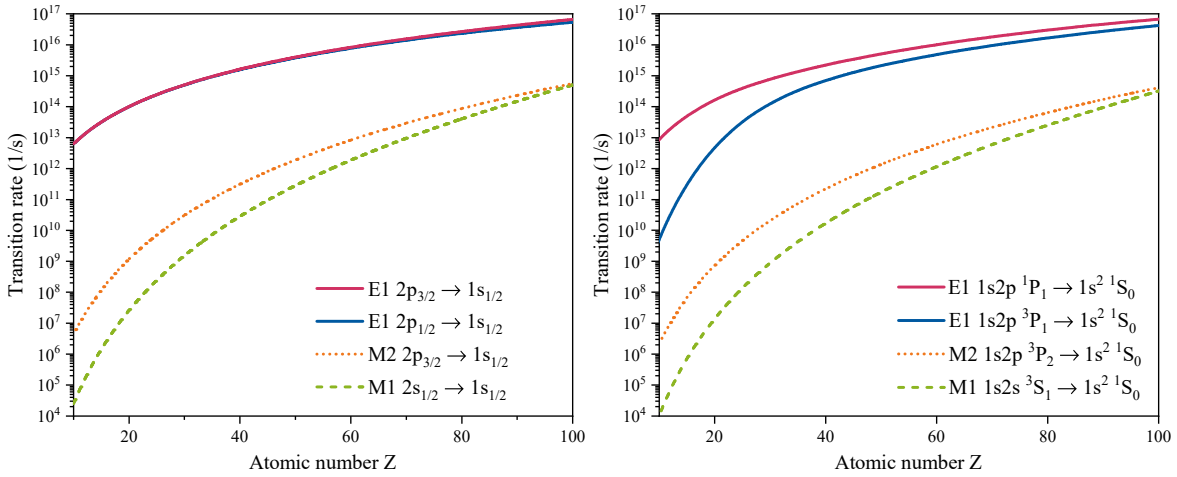

Fig. 2.6: Theoretical single-photon transition rates of most relevant L→K shell transitions as a function of the atomic number Z of: left) H-like systems, relying on [123, 124, 125] for M2, and on [126] for the others, right) He-like systems, taken from [127].

Figure 2.6 depicts the relevant single photon transition rates from the L shell into the K shell for both systems as a function of Z. Although most of the transition rates are of similar magnitude for both the H- and He-like systems, the E1 transition rate from the 1s2p ^{3}P$_1$ energy state of the He-like system drops for lower Z by several orders of magnitude more rapidly compared to the E1 transitions in the H-like system. This additional rate drop comes from the fact that the E1 transition would go from a triplet into a singlet state, called 'forbidden' transition, as it can only occur in the rare event of

an electron spin flip. A strong nucleus-electron interaction favors such flips. In general, for high-Z ions where the nucleus-electron interaction dominates over the electron-electron interaction (leading to a domination of jj-coupling over LS-coupling), the influence of the latter on the transitions within the electronic structure is reduced. Thus, with higher Z the electronic transition behaviour within the He-like system approaches the transition behaviour characteristic within the H-like system. This is apparent in the right-hand panel of figure 2.6, where the $1s2p\,^3P_1 \rightarrow 1s^2\,^1S_0$ E1 transition rate (blue line) within the He-like system approaches the transition rate of the $2p_{1/2} \rightarrow 1s_{1/2}$ E1 transition for higher Z (blue line) of the H-like system.

Electronic level structures are typically investigated through spectroscopy of radiative transitions. However, to this day, measurements probing heavy He-like systems are very rare, since they usually require complex large scale facility experiments (see section 3.3). For example, figure 2.7 shows recent Kα (i.e. L$\rightarrow$K)-transition measurements (previous to the measurement presented in this work) and their deviations against state-of-the-art theory as a function of Z. There have been many Kα -transition measurements in the low- and medium-Z region for He-like systems (see [16] for a summary). In contrast, for high Z, only for $Z = 59$ [128] and $Z = 92$ [129, 130] a few data points exist. Consequently, for the line position determination in those studies, theoretical Kα transition values were used as an energy reference for the others, or the excited state populations and the resulting relative line intensities were assumed [131]. In this context, accurate measurements of high-Z systems are of particular interest, as a possible Z-dependency of these deviations is subject to vigorous debate [16, 132, 133, 134, 135, 136, 137, 138, 139, 140]. Since QED effects scale with Z^4 (see table 2.1), the possible systematic deviation between experimental and theoretical data was expected to be largest for heavy ions. The measurement presented in this work, however, already allowed to contribute to that debate (see [131]). For details on that topic, see the PhD thesis of my co-worker Philip Pfäfflein [141].

Spectroscopic investigations of electronic dynamics originating from a state are usually conducted via measurements of all photons emitted from radiative transitions of that state, if possible. The intensity and timing information of all originating transitions then allows to benchmark transition rate, and therewith state population, theories. However, while transition rates between bound states are of great interest for testing the validity of atomic structure calculations, many of them (especially the rates of

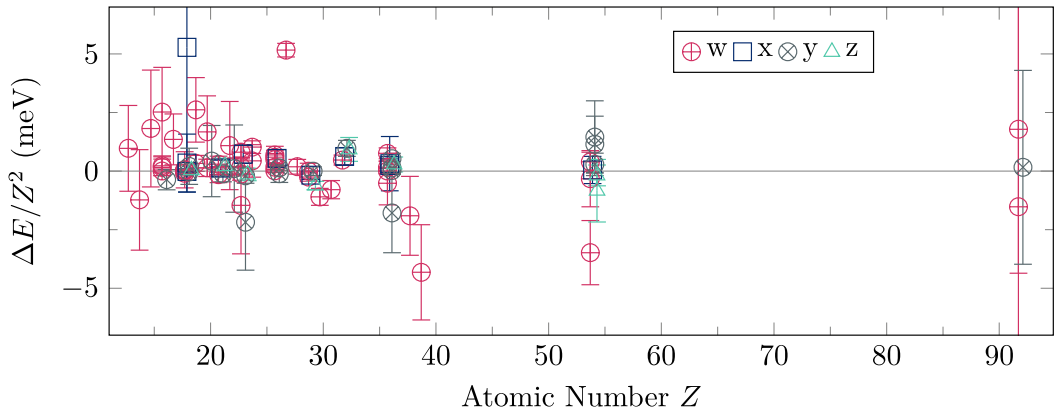

Fig. 2.7: Normalised differences between experimental data taken from [16] and references therein, and theoretical data by [116] for Kα transitions in He-like systems as a function of the atomic number Z, edited from [131].

transitions from states near the nucleus, that are the most the most interesting ones for QED investigations) are not directly measurable for heavy systems. This is due to the fact that in high-Z systems the fastest transitions have rates in the range of $10^{16}\,\mathrm{s}^{-1}$, making a direct study via lifetime measurements not feasible. Instead, there are methods that allow indirect access to this information. For example, for H-like systems, this was demonstrated for the $2p_{3/2}$ state in [142]. For He-like systems, there has been debate about the decay of the $1s2p\,^3P_2$ state [143, 144], which was predicted by [127]. However, for heavy systems, due to the limitations with regards to the energy resolution of suitable detectors and systematic uncertainties of the required x-ray spectroscopy storage ring experiments, no experimental data were available, until now.

3. Basics of heavy ion x-ray spectroscopy

This chapter explains the basics of x-ray spectroscopy of highly-charged heavy ions. Spectroscopy is defined as the study of the absorption and emission of radiation by matter [145], as well as the energy-resolved investigation of interactions between particles (e.g. electrons and ions) with one another. This analytical technique enables e.g. the probing of the electronic structure of atoms by means of photon detection. Radiative transitions involving the inner shells of high-Z systems have energies in the x-ray regime up to about 100 keV. The spectroscopy methods dedicated to this energy range are distinctly different from the ones typically used in the regime of visible light.

3.1 Photon emission and absorption

Heavy ion spectroscopy makes use of the phenomena that when charges, in this case free electrons, are captured into a bound state, or de-excite from an excited into a lower lying energy bound state is most likely (see section 3.5) accompanied by the emission of a photon with characteristic energy equivalent to the exact energy difference. Hence, the collection of emitted photons allows to record a spectrum, which contains information on the electronic structure of the involved atoms. In the context of this work, the process of RR photon emission is most relevant to describe the electron-ion interaction within the electron cooler, as well as the subsequent de-excitation of a captured bound electron. The photon absorption discussed in the following, is most relevant to describe the interaction of a photon with the detection system.

When a photon hits matter, it transfers its energy either via absorption or incoherent

scattering to a bound electron (or very rarely to a nucleus), which can be described as the inverse process to recombination or de-excitation. When the necessary energy difference to an excited state is met, the electron is raised to this higher energy level. If the energy exceeds the ionisation energy, the electron is ionised, so it leaves its bound state (keyword: photoelectric effect [146]). The probability that photon absorption or incoherent scattering occurs is expressed by the respective specific interaction cross section. A detector system makes use of the absorption process, and eventually converts the energy deposited by a particle into a measurable signal (through various methods, differing for the detector kinds). Figure 3.1 shows for example the interaction cross section of a detector absorber made of gold as a function of the photon energy. Note that pair production starts at an energy of $E_{\mathrm{pp}} = 2 \cdot E_{\mathrm{e,rest}} \approx 1022\,\mathrm{keV}$, and becomes the dominant process with increasing energy. The detection of photons can be accomplished

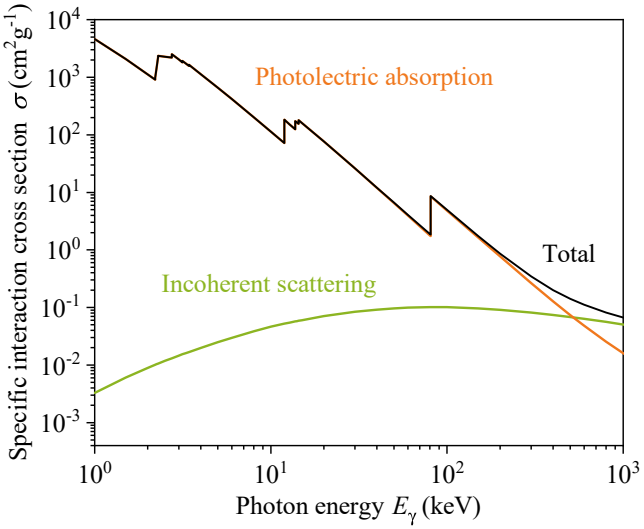

Fig. 3.1: Cross section of specific interaction processes of a photon with gold (Au) as a function of the photon energy, data taken from E_γ [147]. The figure is inspired by [78].

by different types of detectors, depending on the energy and on properties related to the experimental goal, including resolution, energy range covered, or photopeak efficiency. In case of heavy ions, the energies of the emitted electron transition photons lie in the region of several keV to over one hundred keV, so the detectors need to provide high enough stopping power, and hence high quantum efficiency, to allow detection of x-ray radiation of even rare processes and events, with sufficient photon counts. The remaining intensity of a photon beam when it enters a solid state material can be calculated for a given penetration depth x by using the Beer–Lambert law:

$$I(x) = I_0 e^{-\mu x} \tag{14}$$

with I_0 being the incident photon beam intensity and μ the absorption coefficient. With this formula, one can calculate the quantum efficiency ϵ of a detector. This is an important parameter for detector characterisation, as it describes the ratio of the detected photons I_d to the total amount of incident photons I_0:

$$\epsilon = 1 - \frac{I_\mathrm{d}}{I_0}. \tag{15}$$

The photopeak efficiency is another detector characteristic parameter, relevant in this work. It describes the ratio of the photon number in a photon peak (of certain energy) to the number of photons of this energy emitted by the source (here the uranium ions). Next follows a discussion about detection systems suitable to measure x-rays.

3.2 X-ray detection

To detect and measure an x-ray photon's energy, compatible detectors can be categorised into two major types.

On the one hand, there are crystal-spectrometers, which use crystal lattices cut to a specific lattice-plane orientation in order to scatter photons at different angles, onto a position sensitive detector system. Each respective position refers to a scattering angle corresponding to a specific frequency (in accordance to Bragg's law [148]), which is directly proportional to the photon's energy. With this method, resolutions below 1 eV FWHM can be achieved, however, due to its narrow spectral range from several tenth of eV up to several tenth of keV, the choice of calibration sources having a prominent line close to the photon energy of interest is limited (as summarised in [78]).

On the other hand, there are intrinsic detectors, like semiconductor or microcalorimeter detectors, which determine the photon's energy by absorbing the photon and thus generating/activating a proportional amount of information carriers. The resolving power of an intrinsic detector at a certain energy is characterised by the resulting FWHM value of a measured peak at this energy. If the centers of two peaks are separated by a distance smaller than this value, those peaks can not be distinguished. Therewith, the resolution is defined as the minimum distance between two peaks, so they are considered to be differentiable. For example, the intrinsic FWHM energy

resolution of semiconductor detectors can be estimated using [149]:

$$\Delta E_{FWHM} \approx 2.35 \cdot W(E_\gamma, T) \cdot \sqrt{F(E_\gamma, T) \cdot \frac{E_\gamma}{W(E_\gamma, T)}}, \tag{16}$$

with $W(E_\gamma, T)$ being the average energy required to produce an internal electron-hole pair, $F(E_\gamma, T)$ the so-called 'fano factor'[1], E_γ the respective energy of the measured photons, and T the detector operating temperature. For example, in case of a germanium-based detector with a fano factor of $F = 0.11$, at $T = 77.4\,\mathrm{K}$ where the energy required to generate a electron-hole-pair is $W = 2.8\,\mathrm{eV}$, results in a resolution of 100 eV at 6 keV photon energy [150]. Another example for the energy resolution of a germanium-based detector is 500-600 eV at 122 keV photon energy (see [144]). Since semiconductor detectors can even be built to several cm of thickness, they can theoretically reach up to very high quantum efficiencies between 40% and 100%, depending on crystal thickness and the photon energy [144]. However, their limited resolution is insufficient to improve on current QED investigations, which motivated the development of a novel kind of microcalorimeters that were used in the experiment presented in this work.

Microcalorimeters are intrinsic detectors applied for x-ray spectroscopy, measuring the energy of an absorbed particle via its caused temperature change. They are composed of an absorber, representing the detection surface, which is connected to a sensor, able to translate heat into an electric signal. To achieve a sensitivity to (meaning a beneficial signal-to-noise ratio for) small temperature rises (as due to the absorption of a photon), the heat capacity of the absorber has to be small. The heat capacity depends on the absorber's volume, and specific heat capacity (a characteristic parameter of materials that is temperature-dependent) that decreases for decreasing temperatures. Therefore, microcalorimeters need to be operated at very low temperatures to measure x-rays (some well below 100 mK). If a photon hits such a detector, it deposits[2] its energy into

[1] The fano factor is a material-specific statistical term describing the measure of the mean variance of a counting process.

[2] An absorbed photon induces the release of an energetic electron from the absorber material through the photoelectric effect. Due to electron-electron scattering, the free electron loses its energy within the material, until the mean energy of the athermal electrons is reduced to about 0.1 eV, where their energy loss is dominated by generation of phonons[3]. The phonons thermalise through interaction with conduction electrons, but eventually return most of their energy with further thermalisation of the phonon and electron systems to the electrons, since the heat capacity of electrons is larger compared to the one of phonons at low temperatures. When the local electron temperature approaches 1 K, the energy is distributed by a few cubic µm [151].

the absorber material, eventually converting it into heat according to the first law of thermodynamics:

$$\Delta T \simeq \frac{E_\gamma}{C_{\mathrm{tot}}}, \tag{17}$$

with C_{tot} being the total heat capacity of the detector, consisting of the one of the absorber, and the one of the temperature sensor. The specific heat capacity of metal is composed of the contributions of phonons[3] C_{p}, and due to the thermal conductivity of a free electron gas in metal C_{e} (which scale at very low temperature $T \ll \Theta_{\mathrm{D}}$ with $C_{\mathrm{e}} \propto T$ and $C_{\mathrm{p}} \propto (T/\Theta_{\mathrm{D}})^3$, respectively. The parameter Θ_{D} being the material-dependent Debye-temperature [153], at which all phonon modes are excited).

There are different microcalorimeter types, which, over the last decades, saw steady improvement regarding their energy resolution (see figure 3.2). While they all have the above described general working principle in common, they differ in their heat-to-signal conversion methods, because they use different thermometer sensor types (varying in their applicability and limitations). There are, for example, semiconductor thermistor microcalorimeters [154, 155, 156], and transition-edge-microcalorimeters using superconducting Transition-Edge-Sensors (TES) [157].

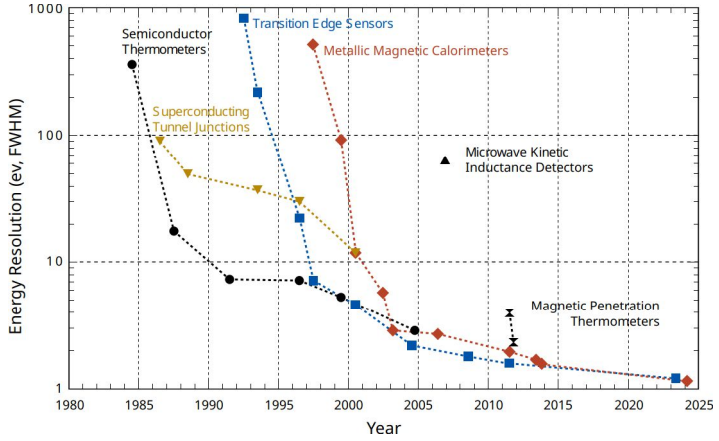

Fig. 3.2: Development of cryogenic x-ray spectroscopy detector systems, taken from [158], extended by [159, 160] by [161].

Figure 3.2 shows that the resolution of modern microcalorimeter detectors is 1 to 2 orders of magnitude higher compared to the resolution of semiconductor detectors, coming close to the one of crystal spectrometers. Depending on the microcalorimeter

[3]Phonons are a type of quasi-particles, describing vibrations within an elastic lattice. While photons are quantised light waves, similarly phonons can be interpreted as quantised sound waves [152].

type, they offer a broad spectral range, as was used for the experiment of this work (see section 5.2.4), comparable to the one of semiconductor detectors, making them promising tools for x-ray spectroscopy.

3.3 Preparation of ion species of interest

The production of highly-charged heavy ions requires the reduction of bound electrons, also called 'electron stripping'. In accelerators, this is accomplished by collisions of ions with designated stripper targets that the beam is passing through. Such a target can be a small gas-filled chamber, or a thin foil of a material of choice, typically a metal. A projectile electron can collide with a target electron, respectively with a target nucleus (even if less likely due to the relative big electronic orbital sizes). If the collision energy exceeds the binding energy of the bound electron, the collision induces the ionisation of the electron. However, for an effective production, the mere surpassing of the ionisation threshold does not suffice. Certain conditions have to be met, that reduce the likelihood an ionised projectile ion immediately re-captures another electron. This can be achieved by stripping at energies, at which a form of the Bohr adiabatic criterion is fulfilled, which states that a projectile loses all electrons with orbital velocity smaller than the projectile's velocity. This stripping criterion inspired various follow-up studies. To roughly estimate the velocity necessary to strip away electrons up to a certain charge, one can for example apply the widely used semi-empirical variation by Hans-Dieter Betz et al. [162], based on the work of Walter Henry Barkas [163] to determine the velocity minimum:

$$Z_{\mathrm{p}}^{\star} = Z_{\mathrm{p}}(1 - e^{-x}), \tag{18}$$

with $x = Z_{\mathrm{p}}^{-2/3}\, v/v_0$, where $Z_{\mathrm{p}}^{\star}$ denotes the effective charge, $v_0 = 2.2 \cdot 10^6 \frac{\mathrm{m}}{\mathrm{s}}$ is Bohr's velocity, and v the ion velocity [164]. In this work, $Z = 92$, and $Z_{\mathrm{p}}^{\star} = 91$, so $v = 92.15\, v_0 = 0.676\, c$, with c denoting the speed of light. For a non-relativistic estimate, this is reasonably close to the actual velocity used to produce U^{91+} in the experiment of this work, which was roughly $v = 89.146\, v_0 = 0.651\, c$ at a kinetic energy of $E_{\mathrm{kin}} = 295\,\mathrm{MeV}/u$.

Nowadays, to determine the requirements of the targets to produce a certain ion beam species with arbitrary charge, there are different estimation theory codes, that take into account the various ionisation and capture cross sections. For example, ETACHA [165], GLOBAL and CHARGE [166], which are implemented in the program

LISE++ [167]. Those tools are used to predict charge state distributions, allowing for effective preparations regarding beam production. Due to numerous accelerator studies and experiments for beams below several GeV/u in the last decades, the effective production of ion species is well understood. Recently, in the context of the Gamma Factory project [168, 169], we published results [170] for the production of the first partially stripped lead ($^{208}Pb^{81+}$) ion beam at 5.9 GeV/u (stored at 526.5 TeV in the LHC [171] at CERN). This showed, that even at this extreme energy, used never before to produce non-bare ions, a reasonable agreement could be found between prediction and experimental findings.

Meanwhile, there also are EBITs, which are able to breed even heavy highly-charged ions in a laboratory, e.g. [44]. However, for measurements of QED effects a high ion intensity is usually necessary, which, up to now has only been feasible at accelerator facilities, which in addition, also allow to filter out ions of a specific charge state. EBITs allow diverse complementary studies, since they have the advantage of being able to be operated in local laboratories, independent of beam time schedules at large facilities.

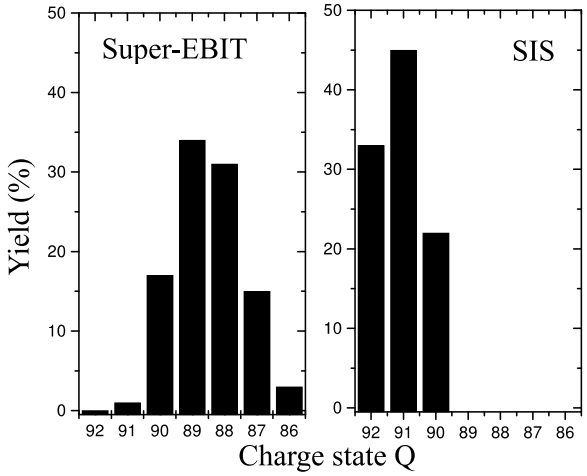

Fig. 3.3: Comparison of the charge state distributions in the production of highly-charged uranium: left) using the Super-EBIT with electron current of 200 mA and 198 keV energy [44], right) using the SIS18 accelerator ring at GSI with equivalent collision energy of 360 MeV/u after passing through a copper-foil. The depiction is edited from [144].

3.4 Electron cooling

The electron cooler was invented by Gersch Izkowitsch Budker, and had its first application in 1966 at the NAP-M ring, in Novosibirsk, for the storage of a proton beam [172, 173]. The idea of electron cooling is to use the Coulomb interaction between ions and electrons, in order to reduce the velocity spread and beam emittance, and thus damping the phase and transverse oscillations (the latter is also called 'betatron

oscillations'), but without reducing the velocity average, so without energy loss of the ions [172]. This is realised by overlapping the ion beam in an electron cooler with an electron beam. The emittance of moving particles in longitudinal and transversal direction can be interpreted as arbitrary three-dimensional movement (discussed in [144]), so that a temperature can be ascribed to a particle beam. In case of a stored ion beam, its increasing emittance leads to a rise in temperature, so the beam becomes hotter due to e.g. interaction with the rest gas. When ions of that beam are successively entering the zone of an electron cooler, they are moving parallel to the cold electron beam, and since their velocity spread is of the same order, their temperatures are proportional to their masses. Due to Coulomb interaction, the ions consecutively collide with cooler electrons, adopting the velocity of the electrons, hence becoming cooler, resulting in the same average velocity. In transversal direction, the achieved temperature balance of the ion beam depends on the temperature of the electron-cooler cathode, which e.g. in case of the ESR at GSI, depicted in the left-hand panel of figure 3.4, lies around 1300 K (≈ 0.1 eV), while in longitudinal direction, the acceleration of the electrons at the cathode decrease their momentum spread, which is then also transferred to the ions. Overall this cooling process allows to decrease the momentum spread of an ion beam by several orders of magnitude (discussed in [143, 144]), as e.g. in case of the ESR electron cooler from $\frac{\Delta p}{p} \sim 10^{-3}$ to better than $\frac{\Delta p}{p} \sim 10^{-5}$ for the example of bare uranium (see right-hand panel of figure 3.4) [174, 175]. To avoid the electron beam temperature from rising, it is renewed continuously, which is why at one end, the electrons end up in a collector (see the left-hand panel of figure 3.4).

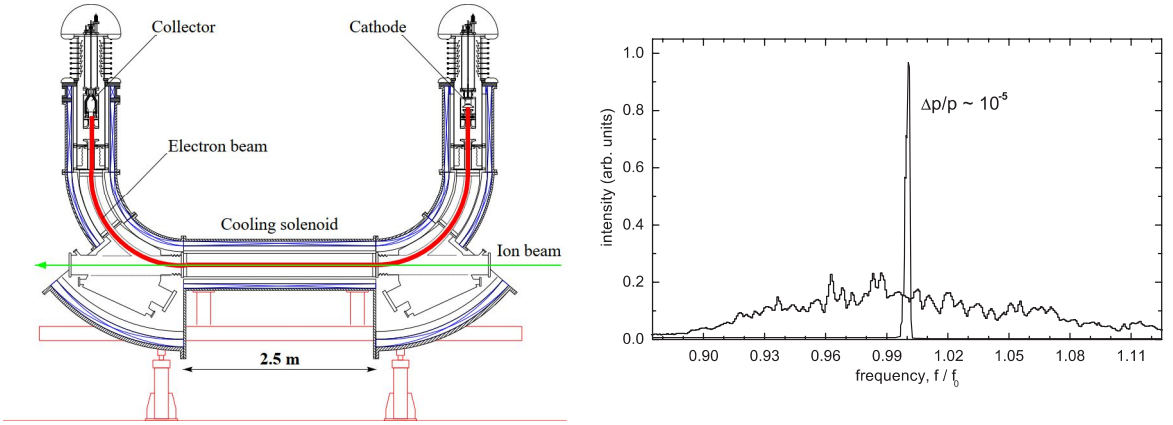

Fig. 3.4: Left) Electron cooler of the ESR edited from [144]. Right) Data from Schottky frequency measurement of a cooled (narrow peak), and uncooled U^{92+} beam, taken from [143].

To determine the net acceleration voltage experienced by cooler electrons, which then imprint their velocity on the ion beam, the voltage applied at the electron cooler needs to be corrected for the space charge potential (see [176]) of the electron beam. This is done e.g. in an approximate way in the calculator available [177]. The following formula then allows to convert net acceleration voltage U into a value for the ion beam velocity β:

$$E_{\mathrm{kin}} = q \cdot U_{\mathrm{EC}} = (\gamma - 1) \cdot m_{\mathrm{e}}c^2 \quad \underset{\Leftrightarrow}{\left(\gamma = \frac{1}{\sqrt{1-\beta^2}}\right)} \quad \beta = \sqrt{1 - \left(\frac{m_{\mathrm{e}}c^2}{m_{\mathrm{e}}c^2 + e \cdot |U_{\mathrm{EC}}|}\right)^2}, \tag{19}$$

with e denoting the elementary charge, m_{e} the electron mass, and U_{EC} the voltage applied at the electron cooler. Photon measurements at electron coolers are limited regarding the lowest energy measurable. This is due to Bremsstrahlung background, emitted from cooler electrons [144]. The specific energy depends on the applied voltage, according to the first half of formula 19.

3.5 Recombination and decay cascades at electron coolers

In general, the capture of a free electron into a bound state of an ion is most likely[4] accompanied by the emission of a photon, called Radiative Recombination (RR) [144] (schematically illustrated in figure 3.5).

The energy of the emitted photon corresponds to the energy difference between the kinetic energy the electron had before (with respect to the ion), and its binding energy after RR, hence resulting in the formula:

$$\hbar\omega = E_{\mathrm{kin,e}} - E_{\mathrm{bin,e}}, \tag{20}$$

with ω being the angular frequency of the photon, $E_{\mathrm{kin,e}}$ the kinetic energy of the captured electron prior to the recombination, and $E_{\mathrm{bin,e}}$ the binding energy of the

[4]Another free electron capture process is the Dielectronic Recombination (DR) [178], where the captured electron's energy is transferred to a different bound electron, that transitions up into an excited state. However, this requires the energy to match the characteristic excitation energy. Hence, if such resonance is not purposely achieved or coincidentally favoured by the experiment, DR is typically less likely than RR.

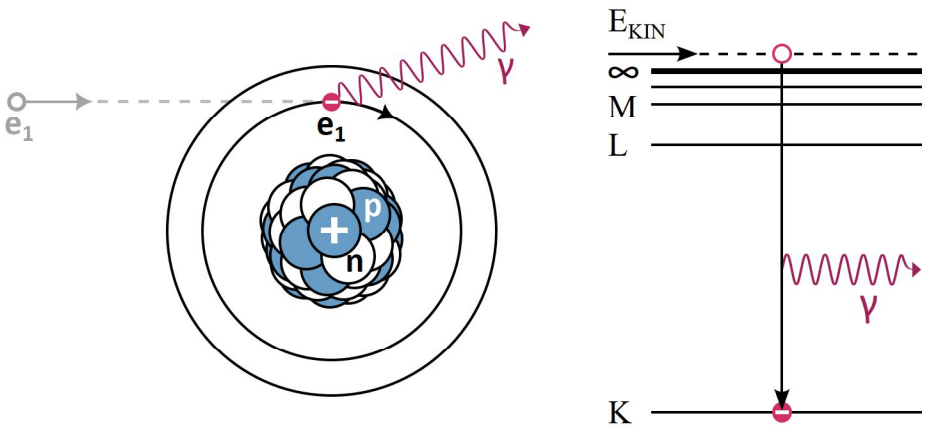

Fig. 3.5: Left) Conceptual illustration of the RR process in the ion rest frame. Right) Schematic depiction of the RR process in regards to energies.

recombined electron in its bound state. The following explanation of the RR treatment is based on the descriptions in the thesis of Alexandre Gumberidze [122], where the development of the theoretical treatment is summarised. Many studies investigating the theoretical determination of RR cross sections showed that this can be achieved very accurately by applying the principle of detailed balance on existing results of the photoionisation [179]. This goes back to its first treatment in 1923 by H. A. Kramers [180]. He derived an expression to determine the recombination cross section, into a fixed n-state:

$$\sigma_n^k(E) = \frac{32\pi}{3\sqrt{3}}\alpha^2 a_0^2 \frac{Z^4 R_y^2}{nE(n^2E + Z^2R_y)}, \tag{21}$$

with a_0 denoting the Bohr radius and R_y the Rydberg constant. The cross section scales for low energy electrons $E \ll E_{n,l}$ with $\sigma_n^k \propto Z^2/(nE)$, and for high energy electron $n^2E \ll Z^2R_y$ with $\sigma_n^k \propto 1/n^3$. Despite formula 21 being derived based on semiclassical physics, it allows the description of the main features of RR. It was later found that RR cross sections predicted by H. A. Kramers' formula and by quantum mechanical treatment agree within 20% (the biggest deviations were found for low n-states). As summarised in [179, 181], H. A. Kramers' work was followed by several studies of RR using quantum mechanics [182, 183, 184, 185]. In 1930, Martin Stobbe [186] found a general quantum mechanical formulation to determine the RR cross section for an arbitrary nl-state, using the non-relativistic dipole approximation. In 1957, H. A. Bethe and Edwin Ernest Salpeter showed that H. A. Kramers' formula can be reproduced on quantum mechanical foundation in the limit of high-n states [72]. A compact analytical formula to calculate state selective RR cross sections for capturing free electrons into

bare ions was given in 1992 in [187]:

$$\sigma_{n,l}(E_\mathrm{e}) \approx \frac{E_{n,l}}{E_e}\sigma(n,l), \tag{22}$$

with $\sigma(n,l)$ being the reduced RR cross section, determined by:

$$\sigma(n,l) = \frac{\pi^2}{3}\alpha^2 a_0^2[(l+1)\cdot c_{l+1}^2(n,l) + l\cdot c_{l-1}^2(n,l)]. \tag{23}$$

In 1995, an exact relativistic formulation was given by Jörg Eichler et al. in [188], building on the work of Akira Ichihara et al. [179], which takes into account the effect of moving bound and free electrons on the nuclear Coulomb field, as well as retardation effects caused by electron-photon interaction:

$$\frac{d^2\sigma_\mathrm{RR}(E',\theta')}{dE'd\Omega'_\mathrm{ph}} = (2j_b+1)(\frac{\hbar\omega'}{m_\mathrm{e}c^2})^2\frac{1}{\beta^2\gamma^2}\frac{d^2\sigma_\mathrm{ph}(E',\theta')}{dE'd\Omega'_\mathrm{el}}, \tag{24}$$

with σ_ph denoting the cross section of photoionisation in the projectile frame, $(2j_b+1)$ the number of angular momentum projections μ_b in the bound state b and over the circular polarisation λ, $\beta = v/c$ the velocity and $\gamma = {}^1/\sqrt{1-\beta^2}$ the Lorentz factor.

RR in electron coolers

The following explanation of the RR in electron coolers is based on the descriptions in the habilitation thesis of Thomas Stöhlker [144], where the RR process in electron coolers is summarised. As described in section 3.4, to cool a stored ion beam in a storage ring, it passes through an electron cooler, where it is overlapped by an electron beam with the same velocity in the same direction. This can result in the exceptional case, that if RR takes place, it happens with relative collision energy of quasi 0 eV.

To estimate the rate λ_RR by which RR occurs for an ion, the non-relativistic dipole approximation of M. Stobbe can be used [186, 189]:

$$\lambda_\mathrm{RR} = \frac{\rho_\mathrm{e}}{\gamma^2}\cdot\frac{l_\mathrm{cooler}}{l_\mathrm{ring}}\cdot\alpha_\mathrm{RR}, \tag{25}$$

with ρ_e the density of the electron beam, l_cooler the length of interaction zone within the cooler and l_ring the total length of the storage ring, γ the Lorentz factor, and α the

rate coefficient, resulting from the convolution of the ion beam velocity v and the RR cross section σ_{RR}:

$$\alpha_{\mathrm{RR}} = \int f(v) \cdot v \cdot \sigma_{\mathrm{RR}}\, d^3v. \tag{26}$$

In case of a low energy approximation after M. Stobbe, and assuming a Maxwell-potential, this coefficient can be simplified into the following expression [190, 189]:

$$\alpha_{\mathrm{RR}} = 3.02 \cdot 10^{-13} \frac{Z_{\mathrm{p}}^2}{\sqrt{k_{\mathrm{B}} T_\perp}} \left[ln\left(\frac{11.32 \cdot Z_{\mathrm{p}}}{\sqrt{k_{\mathrm{B}} T_\perp}} \right) + 0.14 \cdot \left(\frac{\sqrt{k_{\mathrm{B}} T_\perp}}{Z_{\mathrm{p}}^2} \right)^{\frac{1}{3}} \right], \tag{27}$$

with $T_\perp$ being the transversal electron temperature in unit of eV, and k_{B} the Boltzmann constant. Figure 3.6 shows the RR rate for different ions, compared to dipole approximation predictions.

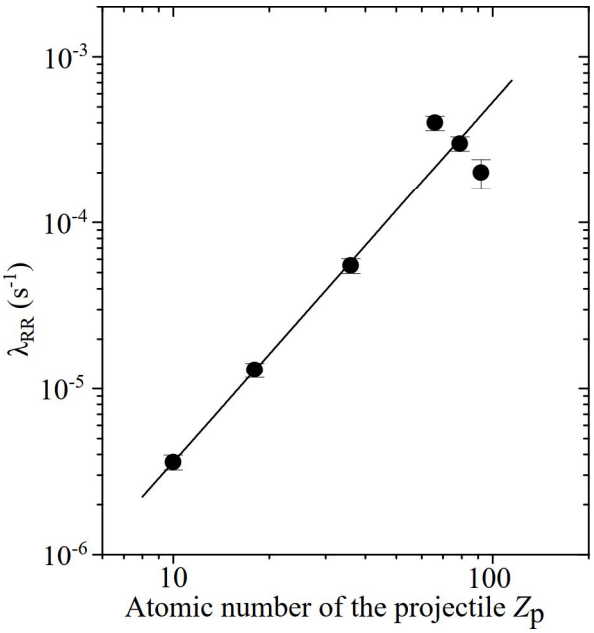

Fig. 3.6: Comparison of the RR rate of cooler electrons for different ions with the dipole approximation as a function of the atomic number Z_{p}, edited from [144].

This occasional electron capture can be exploited, so that, besides its cooling capability, the electron cooler provides an ideal environment to investigate ion-electron interactions. This was done in the experiment of this work.

For the interpretation of the measured spectra (see upcoming results discussion), it should be noted that they share some typical, well-known features, which are characteristic for measurements at electron coolers. Despite the large quantity of available electron states, these spectra tend to only show some specific transitions very prominently, while others are not observable, or comparably negligible. This pattern can

be explained by the interplay of the capture process under the condition of such coolers, and the radiative relaxation behaviour of bound electrons, which follows the selection rules. In [144] the RR process into bare uranium ions was simulated with a relative kinetic energy of 0.2 eV as a function of the quantum numbers n and l, according to [191] using the solution of the approximation from M. Stobbe [186], so a dipole approximation without any other assumptions. Figure 3.7 shows the resulting RR cross section from [144]. According to this widely used theory for RR, at very low relative

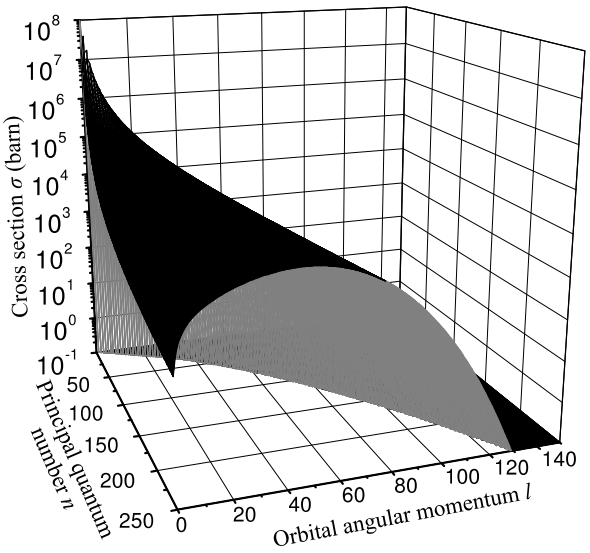

Fig. 3.7: Simulated population characteristics of RR of cooler electrons in bare uranium ions, using a dipole approximation with kinetic energy of 0.2 eV, edited from [144].

energy this recombination occurs into electron states with up to very high quantum number n, with a broad distribution regarding the orbital angular momentum quantum number l, for which is known that $l \leqslant n-1$. Note, that at higher collision energies, high n and l states are no longer important compared to the lower n, l states. The cascade of an electron from an outer (high l) state is strongly dominated by one-photon transitions. Due to the high initial shell n in which the electrons are captured, and following the selection rules, results in most electrons reaching, at some point in their cascade, the state with highest corresponding l in a respective shell n. From that point forward, they can only cascade via states with highest respective l, the so-called Yrast[5]-cascade, as depicted schematically in figure 3.8.

[5]As explained in [192] the word 'Yrast', is the superlative from the old Norse verb hvfirla (to whirl), so means 'whirlingest', and was originally introduced to describe the nuclear energy level, with least energy at that angular momentum.

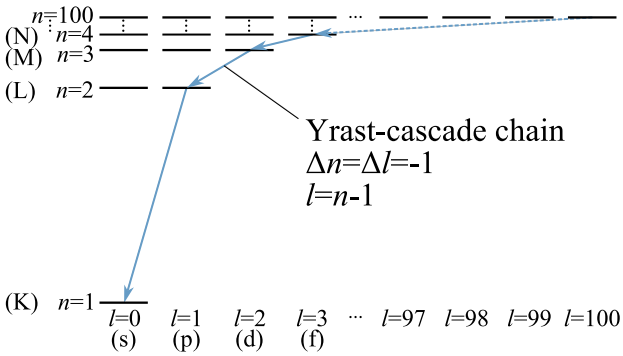

Fig. 3.8: The most prominent cascade transitions of captured cooler electrons have highest angular momentum in each shell. This characteristic pattern is called Yrast-cascade typically occurring at an electron cooler.

3.6 Doppler shift

The interpretations of x-ray spectra measured from fast moving ions rely on the determination of the Doppler shift that affects the photon energies. This effect is described by the Doppler factor f_{Doppler}:

$$E_{\gamma,\text{emit}} = E_{\gamma,\text{lab}} \cdot f_{\text{Doppler}} = E_{\gamma,\text{lab}} \cdot \gamma(1 - \beta\cos(\theta)) = E_{\gamma,\text{lab}} \cdot \frac{1 - \beta\cos(\theta)}{\sqrt{1-\beta^2}}, \qquad (28)$$

with γ being the Lorentz factor, $\beta = \frac{v}{c}$ the relativistic velocity of the emission source, which in this case is the projectile ion, and θ the observation angle in the laboratory system relative to the ion beam path.

Equation 28 shows that the Doppler factor, and therewith the emission energies of RR photons in the reference frame of the ion, can be reconstructed by determining the ion velocity and the exact observation angle as accurately as possible. The influence of uncertainties in their estimation on the result becomes visible by the derivation of equation 28 [144]:

$$\left(\frac{\Delta E_{\gamma,\text{emit}}}{E_{\gamma,\text{emit}}}\right)^2 = \left(\frac{\beta\sin(\theta)}{1-\beta\cos(\theta)} \cdot \Delta\theta\right)^2 + \left(\gamma^2 \cdot \frac{\cos(\theta) - \beta}{1 - \beta, \cos(\theta)} \cdot \Delta\beta\right)^2 + \left(\frac{\Delta E_{\gamma,\text{lab}}}{E_{\gamma,\text{lab}}}\right)^2. \qquad (29)$$

Figure 3.9 shows that the contributions to the total uncertainty caused by β and θ are inversely related. At 0° and 180° observation angles, e.g., the uncertainty due to the geometry is minimal, so the overall uncertainty is depending on the accurate knowledge of the ion beam velocity. In case the observation angle is $\theta = \arccos\beta$, the uncertainty due to the ion beam velocity is minimal and the overall uncertainty depends on the exact knowledge of the geometry [144].

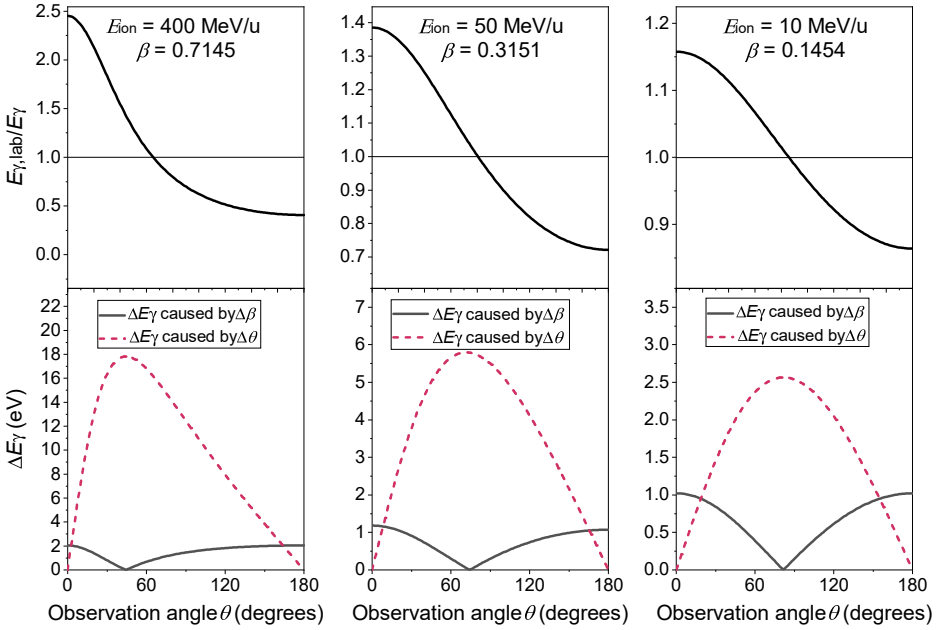

Fig. 3.9: Top) Relative Doppler shift as a function of the observation angle, bottom) Associated uncertainty of the Doppler correction of a transition with $E_{\gamma,\mathrm{emit}} = 100\,\mathrm{keV}$ photon energy in the emitter system as a function of the observation angle. The uncertainty contribution due to ion beam velocity $\Delta\beta$ is a black line and due to observation angle $\Delta\theta$ a red dashed line. The figure is taken from [193].

The most used conventional method for the Doppler correction in x-ray spectroscopy experiments using heavy highly-charged ions, estimates the ion beam velocity via the high voltage applied to the electron cooler voltage divider (see e.g. [194]). A correction of the electron beam space charge potential gives the net acceleration voltage experienced by the cooler electrons, imprinting their velocity on the ion beam. However, this typically used method introduces a systematic uncertainty, due to the unknown contact potential between the surfaces of the cathode and the collector of the electron cooler. The found beta value can then be used in formula 28 to find the Doppler factor. Alternatively, the ion beam velocity can be determined approximately using the Schottky-frequency and an estimate of the length of the beam path (see e.g. [195]). However, the latter is usually not precisely known and therefore this method can not generally be applied for a precise correction of the Doppler shift.

In Laser-Induced Fluorescence (LIF) spectroscopy the Doppler shift can be determined by using the super-imposed (to the ion beam) laser to excite ground-state electrons into excited states (the laser is tuned to hit a resonance) [196]. The fluorescent photons emitted by the ions in direction of the ion beam are then detected. Once the resonance

is found, the known laser wavelength allows to deduce the Doppler shift. Due to the high energy required to excite K shell electrons of heavy ions, instead this method excites electrons into excited Hyperfine-states. Hyperfine-splitting occurs due to the interaction of the nuclear magnetic moment $\mu_I = g_I \mu_N I$, where g_I denotes the nuclear g-factor and μ_N the nuclear magneton, with the total angular momentum of an electron J, so that they couple with each other resulting in the total angular momentum of the ion $F = I + J$. The measurement allows to determine the shift of a state relative to its unperturbed energy [197]. However, this method is only applicable in case of an ion species with nuclear spin I different from 0. Since the measurement presented in this work used a uranium isotope (^{238}U) with even proton and even neutron number, it's nuclear spin is $I = 0$, and the LIF method is not applicable.

Besides these methods, there also is an exceptional case, which does not require Doppler correction of the ion beam velocity for the determination of the photon peak energies. The condition is met when the photon detectors are positioned around the beam line at exactly 0° and 180°. Because using these angles not only eliminates the uncertainty from a slight misalignment of the detectors as described previously, but the cosines in formula 28 become 1 and -1 respectively for the data of each of the detectors. With that, the problem can be simplified to formula 30, allowing to determine the photon energy of each peak in the emission frame through the obtained photon peak pair (for the 0° and 180° detector, respectively) in the laboratory frame, identified to come from the same transition, neglecting the Doppler factor as a whole.

$$\sqrt{E_{\gamma,\mathrm{lab}}(0) \cdot E_{\gamma,\mathrm{lab}}(180)} = E_{\gamma,\mathrm{emit}} \tag{30}$$

While this case is ideal and therefore preferable regarding the Doppler correction, these positions are often not available in highly-charged heavy ion experiments and therefore not universally applicable. In fact, at the experimental facility GSI, only the recent implementation of a new storage ring (see section 5.1.1) in the context of the FAIR facility (see section 5.1) enabled this positioning.

It should be noted, that while the Doppler shift has an obstructive role in modern measurement methods, this is not generally the case. In so-called 'Doppler-tuned spectroscopy' the observation angle is varied, so a line of interest is shifted by the Doppler effect across a steep and well-known absorption edge of a filter material [198].

The spectral features are then determined by the change in count rate, which a detector behind the filter foil detects. This allows the determination of the emission spectrum from a beam. However, it also requires exact knowledge of the the observation angle, beam velocity, and the absorption spectrum of the filter. In this experimental method the achievable resolution is limited by the shape of the absorption edge.

3.7 Spectral line profile

In x-ray spectroscopy, several characteristic influences define the spectral line profile (shape) of a recorded photon spectrum. One influence is the response function that is characteristic for the used detector. In case of this work, the detector response function can be described by a Gaussian profile (see [131]), which is given by:

$$G(x, \sigma) = \frac{e^{-x^2/2\sigma^2}}{\sigma\sqrt{2\pi}}, \tag{31}$$

with σ denoting the standard deviation. In case of photon spectra, x is the photon energy E. Another influence on the line profile arises from the finite lifetime of excited states. An excited state of an ion can be seen as resonance [199]. Its finite resonance width is given by:

$$\Gamma_j = \frac{\hbar}{\tau_j} = \hbar \cdot R_{\mathrm{tr,tot},j}, \tag{32}$$

with τ_j being the state's lifetime, and $R_{\mathrm{tr,tot},j}$ the total rate of spontaneous decay transitions originating from the state j. The finite lifetimes of excited states in heavy ions (see section 2.3) results in 'natural broadening' of the spectral transition peaks (i.e. of the energy distribution of the photons). This (energy) peak broadening is related to the lifetime through Heisenberg's energy-time uncertainty principle $\Delta E \cdot \Delta t \geqslant \frac{\hbar}{2}$, which therefore determines the minimum linewidth a peak can have. Due to the exponential decay of excited states, a spectral line corresponding to a state decay (i.e. transition) can be described through a 'Lorentzian profile':

$$L(x, \Gamma_{\mathrm{tr}}) = \frac{\Gamma_{\mathrm{tr}}}{\pi(x^2 + \Gamma_{\mathrm{tr}}^2)}, \tag{33}$$

with Γ_{tr} denoting the peak's FWHM, that is known as the natural linewidth of the Lorentzian peak and can be determined through:

$$\Gamma_{\mathrm{tr},i\to f} = \Gamma_i + \Gamma_f, \tag{34}$$

where i and f denote the initial and final state of the transition.

In the measurement presented in this work, the detector response function and natural broadening are relevant. Therefore, a spectral line can be described by the convolution of a Gaussian and Lorentzian profile, yielding a so-called 'Voigt profile':

$$V(x,\sigma,\Gamma_{\mathrm{tr}}) = \int_{-\infty}^{\infty} G(x',\sigma) * L(x-x',\Gamma_{\mathrm{tr}})\,dx' = \frac{\mathrm{Re}(w(z))}{\sigma\sqrt{2\pi}}, \tag{35}$$

with $w(z)$ being 'Faddeeva function' (see [200]) and $z = \frac{x+i\Gamma_{\mathrm{tr}}}{\sigma\sqrt{2}}$ [201]. Figure 3.10 shows examples of the different profiles.

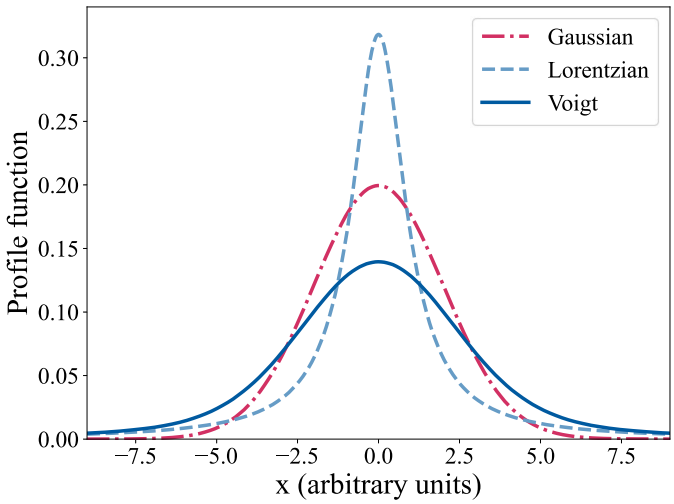

Fig. 3.10: Comparison of the Gaussian, Lorentzian and Voigt profile with $\Gamma_{\mathrm{tr}} = 1$ and $\sigma = 2$.

Moreover, another influence on the shape of an incident spectrum is due to the fact that moving ions imprint their momentum distribution onto their emitted radiation resulting in Doppler-broadening and a Doppler-shift (depending on the observation angle in the laboratory frame). However, for the measurement presented in this work there is no relevant Doppler-broadening, because the cooling process reduces the relative ion momentum spread to a level of about 10^{-5} (see section 3.4).

4. Previous x-ray spectroscopy experiments at GSI

This chapter presents previously conducted spectroscopy experiments at GSI in recent years, investigating electron transitions in order to study the electron structure and dynamics of heavy ions and related QED and nuclear effects. First, the GSI facility and its ESR storage ring are introduced. This is also relevant for the experiment of this work, in which the GSI was responsible for the beam production. These introductions are followed by a discussion of the most recent heavy ion x-ray spectroscopy experiments at the ESR's gas target and electron cooler.

4.1 Experimental environment at GSI

Since 1975, the GSI facility accelerates ion beams in Darmstadt, Germany. For this, it uses an ion source that feeds the linear accelerator UNIversal Linear ACcelerator (UNILAC), followed by an ion synchrotron SIS18[1] and the ESR storage ring (see figure 5.1). What makes this facility unique, is its capacity and the available know-how regarding the acceleration, as well as deceleration and cooling of all elements, including exotic ion species up to the heaviest ones, and importantly, with arbitrary charge. Hence, it was the facility used to produce the highly-charged uranium beam for the x-ray spectroscopy measurement presented in this work (for details on the beam production, see section 5.1). While e.g. CERN is able to accelerate heavy ions to even greater energies, this is typically done with fully stripped particles, since the CERN infrastructure has been focused on high-energy experiments regarding nuclear

[1] SchwerIonenSynchrotron (German for 'heavy ion synchrotron') with a maximum magnetic rigidity of 18 Tm (SIS18).

and particle physics investigations, instead of atomic physics ones. First steps towards few-electron ions in the LHC were coordinated for the first time in 2020 [171] by the Gamma Factory collaboration [168] (for information on my contribution see e.g. [170]). Currently, the 'Facility for Antiproton and Ion Research in Europe' (FAIR facility) is under construction next to the GSI. Thus, the GSI does not only continue to provide interesting experimental opportunities, but is also responsible for the first steps of ion beam preparation for FAIR@GSI, enabling new experimental endeavors in this scientific field, e.g. as is shown by the measurements presented in this thesis.

4.1.1 Ion beam guidance and lifetime

The ion beam is kept on its trajectory by various magnets. Quadrupole magnets are used to focus the beam, thus reducing its emittance (a smaller emittance leads to an increase in beam lifetime). Dipole magnets allow to guide the charged beam. Each of those is adjusted for a small range or a single specific charge state at their respective position in the ring (defined by their magnetic rigidity[2]), so they guide only those ions with the charges of interest on the ideal trajectory. If a charge changing process is purposefully induced and exploited, the magnets following in the path are adapted accordingly to either guide the charge previous to the collision (e.g. in case of some experiments) or the new charge (e.g. in case of stripper targets). As a consequence, all ions with charges that differ from the charge of choice, experience a different deviation in the next magnetic field compared to the desired ions at this position. Eventually, this results in them leaving the ion beam and colliding with the surrounding wall of a vacuum tube. Consequently, the first dipole magnet passed by the ion beam, after exiting the electron cooler, is able to filter out ions that changed their charge, which allows to conduct measurements under coincidence conditions (for more details see 5.2.3).

While the ion beam energy is gradually ramped up to allow stripping, ionisation is typically the dominant charge-changing process. However, after deceleration, the energy does not suffice anymore to ionise the strongly-bound electron in U^{91+}, so that electron capture (Non-Radiative electron Capture (NRC) and Radiative Electron Capture (REC) from rest gas molecules and Radiative Recombination (RR) of cooler electrons) is the

[2]The magnetic rigidity of a charged beam perpendicular to an idealized homogeneous dipole magnet is [202]: $B\rho = \frac{p}{q}$, and defines the 'stiffness' of the beam, i.e. its resistance to be diverted through the Lorentz force imposed by the magnetic field B. The parameter ρ denotes the gyroradius, i.e. the radius of the circular motion, and p and q are the particle's momentum and charge, respectively.

dominant process reducing the ion count and hence beam lifetime. Thus, the total charge changing rate in a storage ring is composed of the RR rate $\lambda_{\mathrm{RR,cooler}}$ within the electron cooler (formula 25) and the following charge-changing rate through collisions between the ions and the residual gas [203]:

$$\lambda_{\text{rest gas}} = \frac{1}{\tau} = \rho \cdot \sigma_{\text{cap}} \cdot f, \tag{36}$$

with τ being the lifetime, ρ the effective particle density (in particles/cm^2), σ_{cap} the sum of the NRC and REC cross sections (NRC strongly dominates at few tenths of MeV/u), and f the circulation frequency. Therefore, it is crucial for experiments involving decelerated beams in storage rings, to have the highest possible vacuum (the ESR is able to achieve a vacuum lower than 10^{-10} mbar), so that the projectile beam can be stored for the maximum length of time, before it vanishes. To establish such vacuum conditions, the beam path of the accelerator facility is guided within vacuum tubes, which are equipped with numerous vacuum pumps and heating sleeves (which allow pre-heating (i.e. baking) the tubes and accelerator elements), among other things. The vacuum establishment in one of the various sections of a storage ring can take a substantial amount of time (from a few hours to several days) depending on various factors, like e.g. the section's volume, and the efficiency of the used pumps.

4.1.2 ESR storage ring

As summarised in [204], the ESR storage ring plays an important role for the investigation of the heaviest ions in the highest charge-states since its commissioning back in the early 1990s [205]. The storage ring enables the carrying out of challenging experiments to study QED effects in strong fields, through investigation of e.g. DR, the 1s Lamb shift, as well as of hyperfine-splitting, with brilliant, electron-cooled beams. It also allows studies on the borderline of atomic and nuclear physics. Ions can be stored, with charge states up to bare ions and energies between 4 and 500 MeV/u depending on the requirements posed of an experiment [143]. Meanwhile, another heavy-ion storage ring has started operation at the HIRFL[3], in China. However, this ring primarily offers research opportunities for medium-heavy ions and exotic nuclei [206], while the ESR is still the only storage ring worldwide providing access within a certain energy range

[3]Heavy Ion Research Facility in Lanzhou (HIRFL) at the Institute of Modern Physics, Nanchang Road 509, 730000 Lanzhou, China.

to arbitrary charge-states of all naturally occurring elements below their production energy, up to fully stripped decelerated uranium.

4.2 Measurement at the ESR electron cooler

An electron cooler is primarily an instrument in a storage ring used for beam cooling, i.e. for reducing the divergence, eventually increasing the storage time. At the same time, its unique zone of interaction between electron and ion beam provides the opportunity to observe charge-changing processes that occur under this special condition of overlapping free electrons and ions with quasi no relative velocity towards one another. An illustration of the ESR electron cooler can be found in the left-hand panel of figure 3.4

4.2.1 Spectroscopy of H- and He-like uranium

In 2003, an x-ray spectroscopy experiment on H- and He-like uranium was conducted at GSI, detecting $\mathrm{N,M} \rightarrow \mathrm{L}$ and $\mathrm{L} \rightarrow \mathrm{K}$ x-rays after RR processes in the ESR electron cooler [122, 207, 208]. The experiment had a very similar setup to the experiment of the work presented here, however, it was conducted at the ESR storage ring using a semiconductor detector. The detector was a segmented Ge(i)-detector which consisted of four individual strips, from which the first three were placed in angles of 0.35°, 0.53° and 0.74° towards the interaction zone respectively, in front of stainless steel windows shielding the ESR vacuum. The measurement was conducted under coincidence condition, using a gas-filled MultiWire Proportional Counter (MWPC) behind the first dipole magnet, behind the electron cooler. The achieved energy resolution was about 700 eV FWHM at roughly 170 keV x-ray energy for all strips. This experiment allowed to investigate the electron-electron interaction in strong fields [122, 207], the ground-state lamb shift in H-like uranium [122, 208], the 'Balmer-like'[4] spectrum of H-like uranium and RR into L-shell sublevels [209, 210], as well as state-selective RR into H- and He-like uranium [209, 211].

[4]Balmer-transitions are defined as the transitions into the L shell of hydrogen atoms. Hence, for other atoms, those transitions are often referred to as 'Balmer-like' transitions.

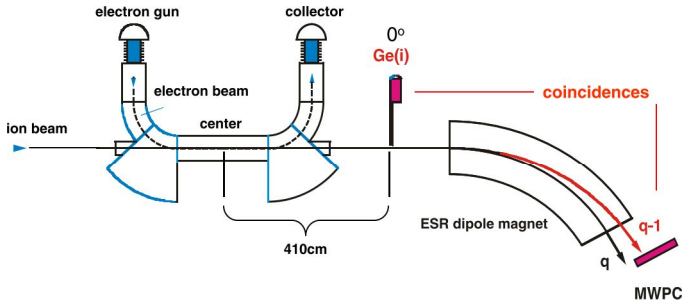

Fig. 4.1: Schematic illustration of the experimental setup at the ESR electron cooler, taken from [212].

4.3 Measurements at the ESR gas target

A gas-target is an instrument dedicated for collision experiments at storage rings. On the inside of such a machine, a beam of gas is created perpendicularly to the ion beam axis. Ions passing through the gas beam can interact with gas particles (in the same way as with rest gas particles, but under defined conditions), emitting radiation that can be detected at different observation positions, which are determined by certain view ports in the vacuum chamber, around the zone of interaction. The challenge with gas-jet targets lies in the production of a gas beam with highest possible density, to increase the interaction probability between ions and gas particles, while keeping interference of the gas with the vacuum in the storage ring to a minimum. Figure 4.2 shows an illustration of the ESR gas-jet target.

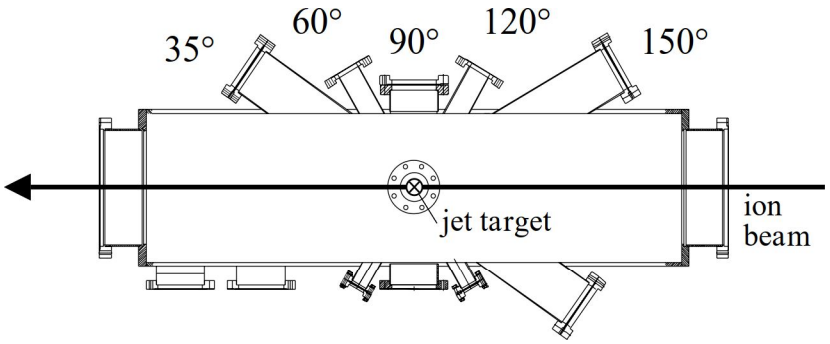

Fig. 4.2: Top down view on a schematic illustration of the ESR gas jet target, edited from [143].

4.3.1 Crystal spectroscopy of H-like gold and He-like uranium

In the last decades there were prominent x-ray spectroscopic experiments conducted at the ESR gas targets using crystal spectrometers. In 2012, a setup using Si(220) crystals was deployed in the FOcusing Compensated Asymmetric Laue (FOCAL) geometry (discussed in [213]). It had a curvature radius of 2 m, combined with a position-sensitive

germanium strip detector [214, 215, 46, 216]. In the target chamber, H-like gold (Au^{79+}) ions, stored at $\beta = v/c = 0.47136$, were brought in collision with a crossing jet of krypton atoms. On either side, perpendicular to the ion-beam path, a FOCAL spectrometer was positioned to detect Lyman radiation, coming from electrons transitioning to the ground state after they were captured in an excited state of gold, forming Au^{78+}. Figure 4.3 shows the experimental setup, as well as a schematic illustration of the photon path within one of the FOCAL setups relative to the interaction zone. The setup was created for energies between 30–120 keV [217]. It allowed to measure photon energies of roughly ±10 keV around a central energy of 63 keV, and achieved an energy resolution of roughly 60 eV FWHM at 63 keV photon energy in the beam time [215]. This enabled a measurement of the ground state Lamb shift in heavy H-like ions (Au^{78+}), achieving a statistical uncertainty of 2.2 eV [46].

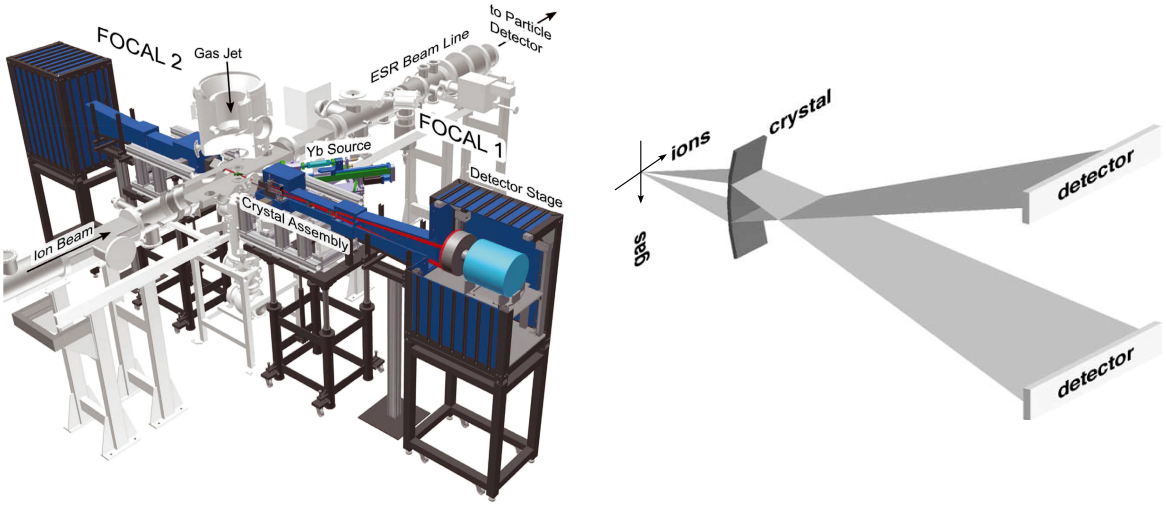

Fig. 4.3: Left) Schematic illustration of the FOCAL experiment at the ESR gas target, taken from [216]. Right) Geometrical working principle of the FOCAL crystal spectrometer, explained in detail in [213], edited from [217].

In 2021, a twin high-resolution crystal spectrometer made of cylindrically bent germanium (220) crystals was deployed, having a curvature radius of 2 m, combined with a CCD camera of 2048 × 2048 pixels each, at the ESR gas target. In the target chamber, H-like uranium ions, stored at an energy of 41.03 MeV/u, were brought in collision with a crossing jet of nitrogen atoms. Figure 4.4 shows a schematic illustration of one of the spectrometers in front of the gas target chamber. The two setups were built for the measurement of the $1s2p\,^3P_2 \rightarrow 1s2s\,^3S_1$ intra-shell (i.e. of a transition within the same shell, here in n = 2 shell, resulting in $\Delta n = 0$) transition in He-like uranium. They were

positioned perpendicular to the ion-beam path to detect x-rays originating after H-like uranium ions captured an electron. The experimental findings allowed to determine the energy of the studied intra-shell transition of He-like uranium with an accuracy of 37 ppm [42]. The spectrometers (which have an instrumental energy resolution of about 0.7 eV FWHM) covered a spectral range of roughly 80 eV and achieved an energy resolution of about 2.7 eV FWHM [48].

In addition, the same approach using He-like uranium stored at 30.16 MeV/u, and Li-like uranium stored at 39.29 MeV/u, to form Li-like, or Be-like uranium by electron capture, respectively, allowed to disentangle and investigate electron-electron interaction terms and one-electron higher-order QED effects without any nuclear radius related uncertainty [42].

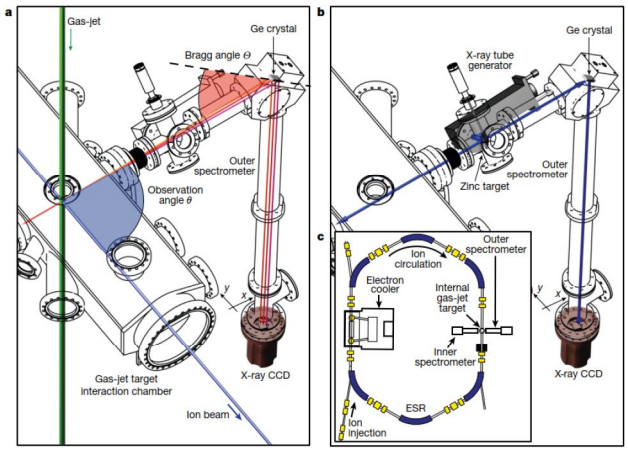

Fig. 4.4: Schematic illustration of: a) the experiment at the ESR gas target, using crystal spectrometers, b) the same experiment, additionally having a zinc target installed at an x-ray tube, c) of the ESR (with top-down view) showing the position of the two detectors. This figure is taken from [42].

5. X-ray spectroscopy of He-like uranium at CRYRING@ESR

The x-ray spectroscopy experiment for the work presented in this thesis was conducted using stored H-like uranium ions at the CRYRING@ESR in 2021. Its goal was to measure N, M $\rightarrow$ L and L $\rightarrow$ K transitions x-rays, emitted when cooler electrons, captured via RR into excited states of uranium ions, cascade down into the ground-state. First, the experimental environment and setup are presented, followed by an overview of the beam time and an explanation of the raw data analysis and corrections. Finally, a comparison of a resulting photon spectrum to one previously measured at the ESR (explained in section 4.2.1) is made.

5.1 Experimental environment at FAIR

Currently, the FAIR is under construction next to the GSI. This new facility uses the GSI infrastructure for beam production and will provide an additional synchrotron called SIS100[1], as well as several storage rings. The SIS100 accelerator will allow to reach energies up to roughly 10 GeV/u in case of U^{92+} [218]. One of the additional storage rings connected to the ESR has already been installed and was first commissioned in 2020: the CRYRING@ESR. The description below presents the beam preparation procedure at the GSI to eventually store H-like uranium ions in the CRYRING@ESR for the measurement.

At the source, uranium was ionised (typically by electric discharge of a vacuum arc-type ion source [219]). The so created lowly-charged U^{4+} ions were extracted from the source

[1]SchwerIonenSynchrotron (German for 'heavy ion synchrotron') with a maximum magnetic rigidity of 100 Tm (SIS100).

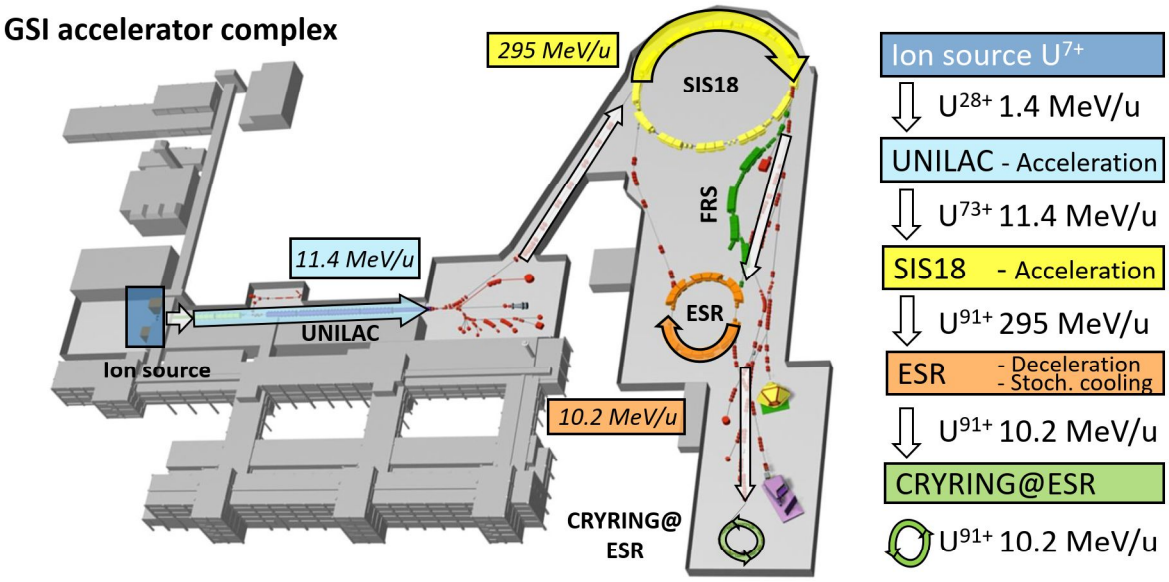

Fig. 5.1: Ion beam production chain at the GSI accelerator facility.

into a high current injector, in which they were accelerated towards a gas stripper with an energy of about 1.4 MeV/u, allowing the stripping of more electrons. The resulting U^{28+} ions were injected into the linear accelerator UNILAC. Here, they were accelerated to 11.4 MeV/u. Dipole magnets guided the charged beam from the UNILAC through a transfer channel, where the beam is passed through another stripper foil to increase its charge again. The created U^{73+} ions were then injected into the heavy ion synchrotron SIS18. In the SIS18, the beam with an intensity of about $1{\cdot}10^9$ particles (at injection) was accelerated to an energy of roughly 295 MeV/u. Next, the beam was guided through another transfer channel, where it was stripped to create U^{91+} before injection into the ESR. In this storage ring, the beam was decelerated down and cooled by the ESR electron cooler, creating a beam of 10.225 MeV/u U^{91+} ions. Finally, these ions were injected via another transfer channel into the CRYRING@ESR. This reduced the the beam intensity to a low number of roughly $(1\text{-}2)\cdot10^6$ particles (at injection). In the CRYRING@ESR the beam was cooled by the electron cooler, around which the setup for this experiment has been installed (see [220] for more details).

5.1.1 CRYRING@ESR storage ring

The CRYRING was optimised for energies reaching from ∼14 MeV/u down to 300 keV/u or lower. Originally, it was operated at the Manne Siegbahn Laboratory[2] in Stockholm between 1992 and 2009 [221, 222]. However, it was used for experiments with ions of much lower Z, or if heavy, of lower charge states. This is the reason why no x-ray experiments were conducted, contrary to the present work. The integration of the CRYRING into the FAIR facility, attached to the ESR (hence the name of CRYRING@ESR), also allows to cover experiments in the previous energy gap between the ESR and Highly charged Ion TRAP (HITRAP) [223, 224] capabilities (see figure 5.2). Like the ESR, also the CRYRING@ESR is uniquely providing access within

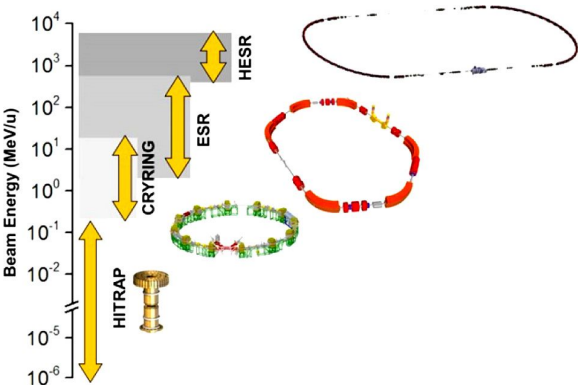

Fig. 5.2: Overview of the ion storage facilities at the GSI/FAIR, taken from [225].

a certain energy range to arbitrary charge-states of all naturally occurring elements below their production energy. Thus, the FAIR facility, also containing the upcoming 'HochEnergieSpeicherRing' (German for 'high energy storage ring') (HESR), will be able to provide intense beams of highly charged ions and exotic nuclei in the entire energy range from 5 GeV/u almost to resting state (see figure 5.2). In addition to covering an additional energy range, the CRYRING@ESR also offers other advantages. Most important, for this experiment, are the ultracold electron cooler and the surrounding view ports at 0° and 180° (the ESR storage ring at GSI does not provide this angle constellation due to a lack of view ports and space for detectors), as well as the excellent ultrahigh vacuum conditions of $< 10^{-11}$ mbar. With such a vacuum, ion beam lifetimes between 3 s and 15 min are achievable. Another practical advantage is its compactness: its circumference of 54.17 m is half of the 108.36 m of the ESR (see figure 5.3).

Thus, the CRYRING's integration into the GSI environment as part of the FAIR project, in combination with the ESR, and the availability of exotic nuclei and heavy bare, one-

[2]Manne Siegbahn Laboratory, Stockholm University, Frescativägen 24, 10405 Stockholm, Sweden.

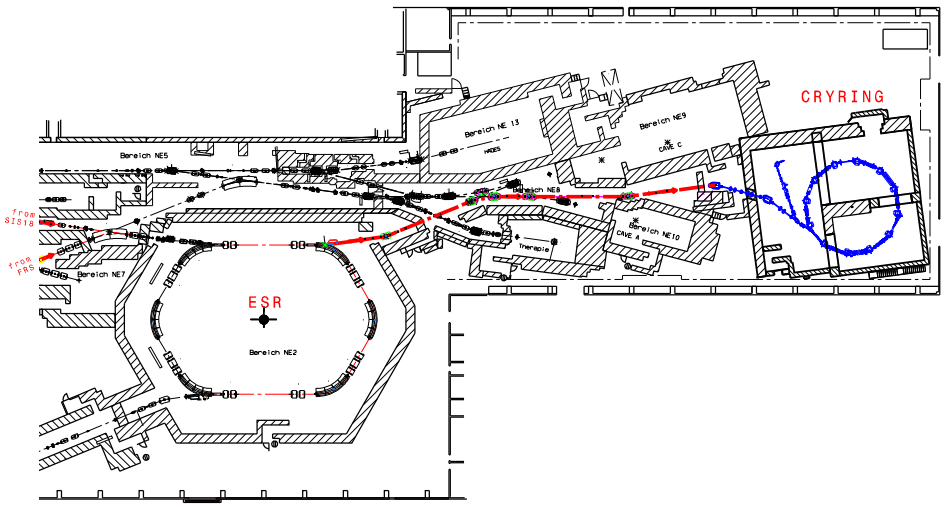

Fig. 5.3: Technical drawing of the ESR and CRYRING@ESR storage rings at GSI, taken from [204].

and few-electron ions, opened up new research opportunities (e.g. the work presented in this thesis).

5.2 Experimental setup at the CRYRING@ESR

Since the CRYRING@ESR has not been previously used for x-ray spectroscopy experiments with heavy highly-charged ions, the preparation of its electron cooler for such experiments had to be conducted from scratch during the course of this work. Figure 5.4 shows the resulting setup, which is described in the sections that follow (also see [220]).

Two quasi-identical[3] detection setups were placed at either side of the electron cooler of the CRYRING@ESR in front of the view ports of the adjacent dipole magnets, at 0° and 180°. Two window chambers with calibration source holders were attached to the view ports via bellows. The construction frames were placed at 3.5 m distance from the centre of the electron cooler, and were holding two detectors each: a Ge(i) semiconductor detector contained in a cryogenic storage dewar (visible in orange color in the lower panel of figure 5.4), as well as an MMC contained in a cryostat (visible in grey color in the upper panel of figure 5.4). The semiconductor detector had a monitoring function for the beam setup. Last but not least, a particle detector downstream of the

[3]The Computer Aided Design (CAD) model of the experiment preparation (figure 5.4) shows a different cryostat at the 0° view port, where eventually a cryostat similar to the one at 180° was used.

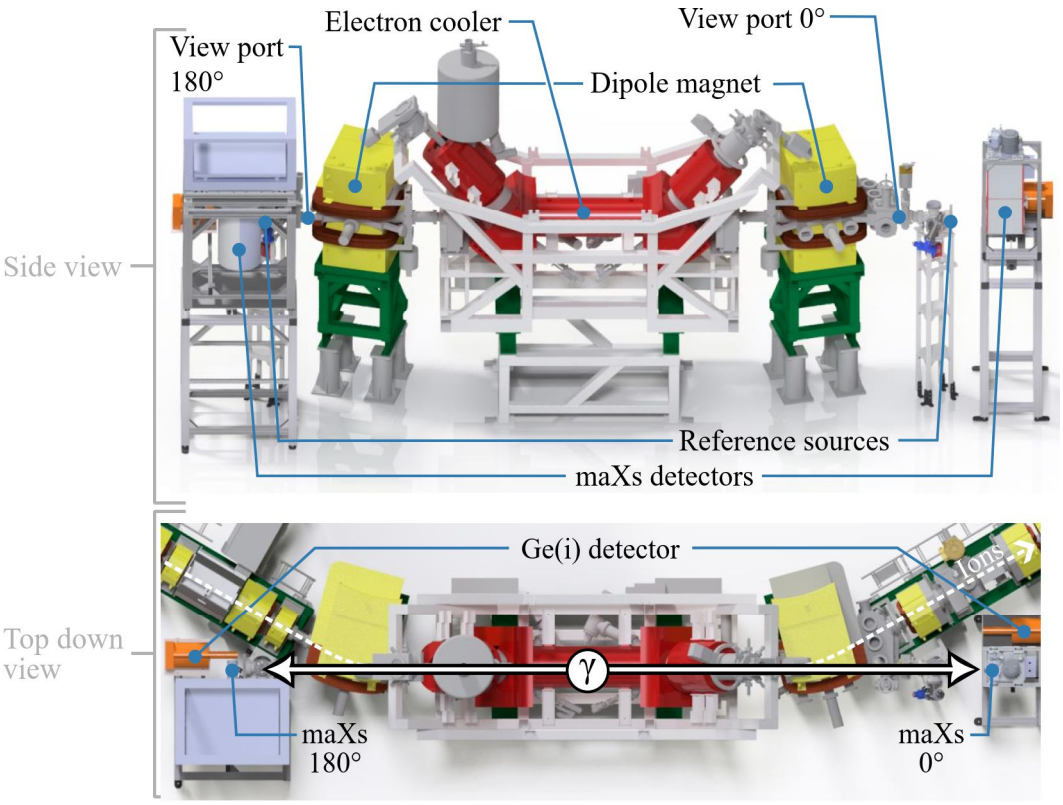

Fig. 5.4: Top) Experimental setup at the CRYRING@ESR electron cooler deployed for our measurement. Bottom) Top-down view on the setup, to illustrate the ion beam path (white dashed line) and the path of the photons emitted during cooler electron capture (white full lines).

ion path was used to set coincidence conditions.

5.2.1 X-ray windows and window chambers

Initially, the view ports of interest (at 0° and 180°) were not equipped with appropriate windows. For the purpose of x-ray spectroscopy, 100 µm thick beryllium windows of about 30 mm diameter were chosen. This material has a high stability, even in the shape of thin foil, and still allows photons of only few keV to traverse. However, changing view port windows can be a time-consuming process. While the view ports can be shut by valves (also called 'shutters'), they do not prevent the insertion of air into the storage ring (from between a new window and the valve). Thus, the exchange of a window breaks the vacuum of the corresponding storage ring segment, which then has to be re-established. This can take several days, which is a critical amount of time considering the scarce beam time. To enable a fast exchange of windows at these view ports between

experiments, two dedicated window chambers had to be constructed to separate the windows from the CRYRING@ESR vacuum [226, 220]. Chambers between a valve and a window reduce the vacuum breaking to a small volume. Equipped with necessary vacuum construction equipment, the chambers allow a quick renewal of their vacuum before valve opening. It should be noted, that installations like window chambers are usually provided by the user facility. However, at the time, the CRYRING@ESR had only just been implemented. Thus, the setup had to be designed and constructed in the context of this work.

The main requirement regarding the chambers was first and foremost, that the chambers had to be available with a reasonable time and effort due to the strict installation schedule posed by the facility. So only non-custom made chamber elements had to be involved. Moreover, the design requirements for the chambers stipulated the smallest possible volume to minimise the additional space between the interaction zone and the detector. This design allowed maximising the the solid angle covered by the detector. The chambers should still allow to connect a window flange, an adapter-flange for the temporary fixation of a turbo-pre-pump for low vacuum, an ion getter-Non-Evaporable Getter (NEG)-combi pump (delivered by SAES[4]) and a vacuum gauge for probing (see left-hand panel of figure 5.5). Each chamber was equipped with heating jackets for the chamber and pumps (see right-hand panel of figure 5.5).

The combi pump is a combination of a NEG pump and an ion getter pump. This NEG pump is made of cartridges consisting of discs made of a getter material, so of porous alloy or powder mixture which bonds gas molecules using metallic surface sorption. To activate such a pump, it has to be heated to over 500°C, after which the coating material readily forms stable compounds with active gases, even at room temperature and without the need of electric power. The disc and cartridge are designed to create a potentially large surface area in a small volume, where gas molecules can bond. An ion getter pump or Sputter Ion Pump (SIP) ionises a gas in an attached vessel and applies a high voltage (up to 7 kV in case of the used pumps [227]). This accelerates these gas ions, which then collide with the solid electrode made from a getter material, which spreads small fractures of the electrode into the chamber. This induced sputtering of the getter material can then trap gas molecules via chemical bonding, or by covering and thus pinning them to the chamber's wall. Due to the latter attribute, this pump

[4]SAES Getters S.p.A., Viale Italia 77, 20045 Lainate (Milan), Italy.

can even be used effectively for noble gases.

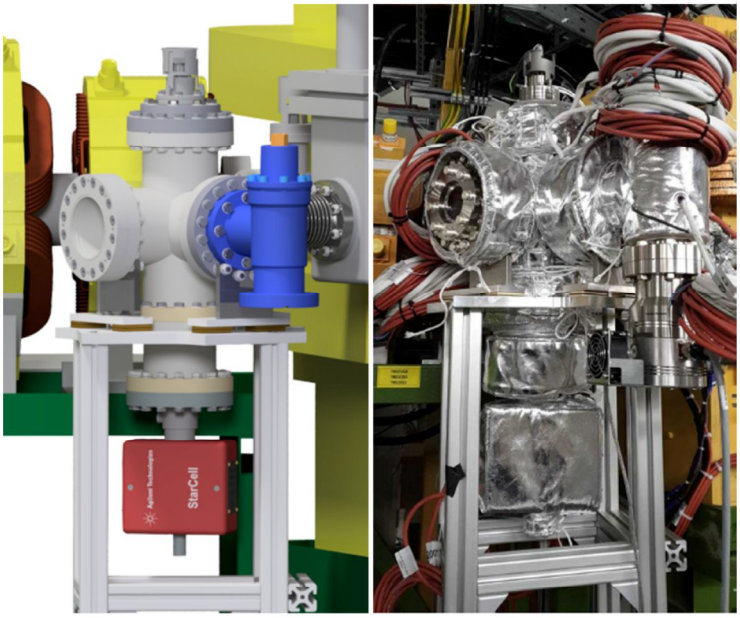

Fig. 5.5: Window chamber at 180° at the CRYRING@ESR: left) CAD model showing the vacuum gauge (dark grey), the turbo-pre-pump adapter-flange (dark blue) and the iongetter-NEG-combi pump (delivered by SAES[4]) (red), right) photo of the actual installed chamber, covered by heating jackets, with mounted window flange.

The window chambers were connected to the view ports via a bellow. It had to be ensured that their substructures still allowed aligning the chambers during the installation, while providing great stability to reduce an uneven distribution of gravitational leverage on the adaption flange. To further improve stability, the construction was bolted to the ground and connected to the CRYRING@ESR support structure. After successful installation (under exceptional difficulties due to the Covid-19 crisis) at the CRYRING@ESR, the first heavy ion test beam was run using lead ions in 2020 [228]. Following commissioning in 2020 and the measurement of this present work in 2021, the window chambers became a permanent installation at CRYRING@ESR.

5.2.2 Calibration sources

The use of energy-sensitive x-ray detectors typically requires radioactive gamma reference sources to calibrate the energy axis of the x-ray detector and to monitor their performance over time. The sources were located on movable sliders within lead-shielded boxes, mounted at each chamber, between the windows and the cryostats containing the detectors. The remote controlled sliders allowed to move one of four prepared positions in front of the detectors: one empty frame and three with pre-installed calibration sources. Figure 5.6 depicts the CAD model of a mounted calibration box at 180°, and a photograph of one of the open boxes.

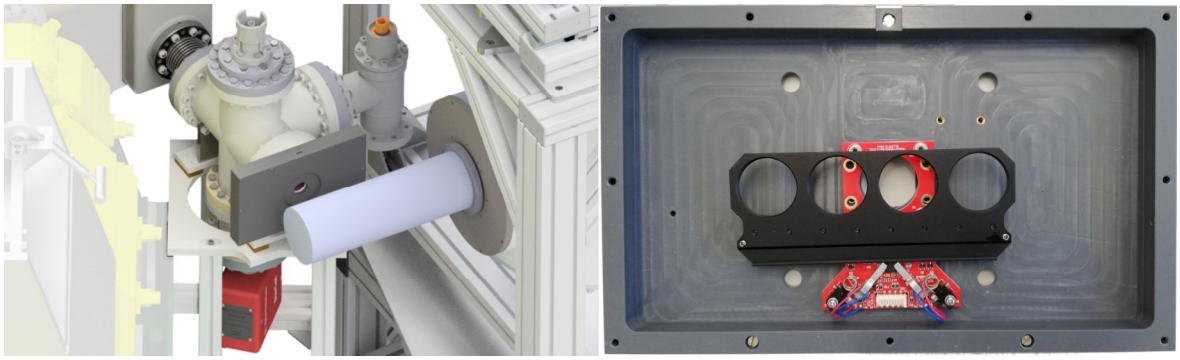

Fig. 5.6: Left) CAD model of the calibration source holder at 180°, edited from [220]. Right) Photo of an open calibration box and the remote-controlled source holder frame. Note that the closing lid was equipped with a layer of lead to shield the calibration source radiation when the empty frame position was used.

The empty frame position was used for measuring the x-ray radiation emitted in the cooler section (including the x-rays from U^{90+}) during beam storage in the CRYRING@ESR. After the beam vanished and before a new injection cycle started, the various other positions were used to collect photons from the calibration sources. Their known emission patterns serve as a reference to calibrate the spectra by using some of their characteristic emitted photon peaks. The calibration measurements were done in each injection cycle, to collect the calibration data under the same experimental conditions (e.g. temperature, and background), so with similar detector gain factor (see section 5.3.3 for more information). The choice of calibration sources depended on whether or not they emit photons of energies near to the peaks of interest. Since this experiment aimed to investigate a broad energy range (from few keV to around 100 keV), the calibration of the low energy region (from of $L \rightarrow K$ transitions) and high energy region (from $N, M \rightarrow L$ transitions) were done separately. The used calibration sources and their corresponding emission lines and escape peaks[5] are listed in table 5.1. The sources were equipped with various foils to filter out, or reduce the intensity of unwanted photons. For more information on the calibration process see [141, 220].

[5]Escape peaks are created by incomplete energy deposition of photons in the absorber material, so when an incoming photon excites an absorber atom, and results in relaxation into the ground-state, accompanied by the emission of a photon exiting the detector. An escape peak's energy corresponds to the original photon energy minus the energy of the escaped photon [229].

Table 5.1: List of calibration sources and their corresponding emission lines used to calibrate the peaks in the N, M→ L and L→ K transition energy regions. The ⋆ symbol marks cobalt (Co) lines that are escape peaks of the 122.1 keV emission instead.

		N, M → L		L → K	
Sources	Symbol	0°	180°	0°	180°
Cadmium	$^{109}_{48}$Cd	-	-	-	88 keV
Americium	$^{241}_{95}$Am	26.3 keV	26.3 keV	26.3 keV	-
		59.5 keV	59.5 keV	59.5 keV	59.5 keV
Cobalt	$^{57}_{27}$Co	14.4 keV	14.4 keV	122.1 keV	122.1 keV
		53.1 keV⋆	53.1 keV⋆	136.5 keV	-
		55.3 keV⋆	55.3 keV⋆	-	-

5.2.3 Coincidence enabling particle counter

To use a coincidence measurement method, a particle counter that detects the down-charged ions responsible for the photon emission, is needed behind the electron cooler. For this task, the CRYRING@ESR particle detector was used, which was a novel installment directly behind the dipole magnet next to the electron cooler, downstream of the ion path (see [230, 231]). The detector was a Channel Electron Multiplier (CEM) with extended dynamic range, able to account for up to 10 MHz incidence rate in single particle counting mode, with a pulse duration of $\sim$ 5 ns. To avoid direct exposure to hard radiation, it was combined with a preceding stainless steel plate, on which the down-charged ions impinged. Hence, the CEM detected secondary electrons, that were emitted from the plate [230, 231].

5.2.4 Microcalorimeter detectors of type maXs

For the experiment of this work, novel MMC detectors were used (see description below). Note that the explanations that follow are based on the descriptions in the doctoral thesis of Daniel Hengstler [232], who played/plays an important role in the development of the detectors used in the presented work, and of Marc Oliver Herdrich [78], who has worked/is working extensively with the presented detector type in context of atomic physics experiments with highly-charged ions at accelerators and EBIT.

Metallic Magnetic Calorimeters

MMCs use a paramagnetic sensor that is located in a small magnetic field [151]. The sensor is made of a noble metal, doped with rare-earth element atoms, which in case of the used detectors, was erbium-doped silver (Ag:Er) (with $\Theta_{\mathrm{D,Ag}} \approx 227\,\mathrm{K}$ [233]). In this context, Er ($Z = 68$) gives three of its electrons for metallic bonds with Ag, thus substituting for Ag ($Z = 47$) at regular fcc lattice sites, resulting in Er^{3+} ions that have the electron configuration $[Kr]4d^{10}\,4f^{11}\,5s^2\,5p^2$. This inserts a magnetic moment into the sensor, coming from the partially filled f-orbitals of the Er ions [151]. At working temperatures below 100 mK, electrons only populate the lowest energetic doublet of Ag:Er, which is distanced by 25 K, to the next highest multiplet state [234]. Due to this isolated ground-state doublet, the doping atoms act like spin-$^1/_2$-systems. This is exploited through application of a low external magnetic field, that splits the described level into two energy levels, which are either parallel, or anti-parallel to the magnetic field (resulting in Zeeman-splitting). For the sensor, this leads to a doping induced macroscopic magnetisation:

$$M(B,T) = -\frac{\tilde{g}\mu_{\mathrm{B}}}{2}\frac{N_{\mathrm{spin}}}{V}\tanh\left(\frac{\tilde{g}\mu_{\mathrm{B}}B}{2k_{\mathrm{B}}T}\right), \tag{37}$$

with $\tilde{g}$ being the effective Landé g-factor, $\mu_{\mathrm{B}} = \frac{e}{2m_e}\hbar = 9.274 \cdot 10^{-24\mathrm{J}}/\mathrm{T}$ the Bohr magneton, N_{spin} the total number of available spin systems, k_B the Boltzmann-factor, V the sensor's volume, B the external magnetic field, and T the working temperature of the detector.

Thermal energy transferred from the absorber to the sensor can cause the spin of its Zeeman-systems to flip, leading to a decrease in the sensor's magnetisation. This variation of the magnetic flux is transmitted via pick-up coil to the Superconducting QUantum Interference Device (SQUID)[6]-based read-out electronics [236]. The absorber-sensor system is linked to a cold reservoir, that provides the low temperature necessary for the required small specific heat capacities (see section 3.2), and allows to return the detector to its working temperature after each energy deposition (absorption).

[6] A SQUID is a highly-sensitive measuring device for small magnetic fluxes (i.e. a magnetometer for weak magnetic fields). In this work, dc-SQUIDs were used that consist of two Josephson junctions (instead of e.g. one in rf-SQUIDs) connected in parallel within a closed superconducting loop (based on [235]).

Figure 5.7 depicts the described working principle.

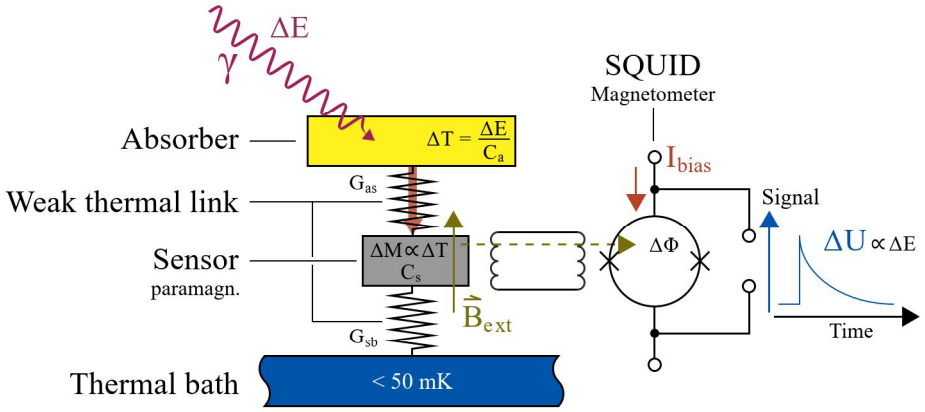

Fig. 5.7: MMC working principle, edited from [78]. From top to bottom, left to right: a photon is absorbed, creating heat. The change in T reaches the paramagnetic sensor (at which a magnetic field is applied), reducing its magnetisation. This magnetisation change is transmitted via coil to the SQUID Magnetometer, which then converts it into a voltage signal. The whole setup is connected to a thermal bath, guaranteeing the low temperature for the required heat capacities and to return the detector to its working temperature.

The fundamental optimal energy resolution of an MMC detector, taking into account thermodynamical noise [232, 237]:

$$\Delta E_{\mathrm{FWHM}} \approx 2 \cdot \sqrt{2 \cdot \ln(2)} \cdot \sqrt{4 k_{\mathrm{B}} T^2 C_e} \left(\frac{1}{c_{\mathrm{rs}}(1 - c_{\mathrm{rs}})} \frac{\tau_0}{\tau_1} \right), \tag{38}$$

for $\tau_0 \ll \tau_1$ and $c_{\mathrm{rs}} = {}^{C_{\mathrm{se}}}\!/\!_{(C_{\mathrm{e}} + C_{\mathrm{se}})} \approx {}^{1}\!/\!_{2}$, where C_{se} is the specific heat capacity of the sensor. The parameters τ_0 and τ_1 denote the signal rise and decay time, respectively. Formula 38 shows that the energy resolution is smallest for $c_{\mathrm{rs}} = {}^{1}\!/\!_{2}$, so when the heat capacity of the absorber and sensor are the same [232]. In addition, it is possible to tune the resolution by influencing the rise and decay time accordingly (however, with limitations and compromises, see [232]). While for microcalorimeters there is no statistical fluctuation, the finite resolution comes from energy-independent noise contributions, most importantly the thermal noise. This is another reason why the working temperature of microcalorimeters has to be very small (in orders of several mK).

Planar meander-shaped pick-up-coils (first used in [238]) under the sensors allow to read out their magnetisations. Figure 5.8 shows a schematic diagram of the sensor read-out

setup. The coils are linked in pairs to their own separate parallel input coil (noted with L_i in figure 5.8), which is near to the SQUID-based read-out electronics. Both pick-up coils contribute to the output signal with different polarities, so using them in parallel allows to reduce the influence of chip temperature variations, and of external magnetic fields (any external influence that simultaneously decreases the magnetisation of both pixels of a pair equally, generates two currents of opposite signs that cancel each other out) [232].

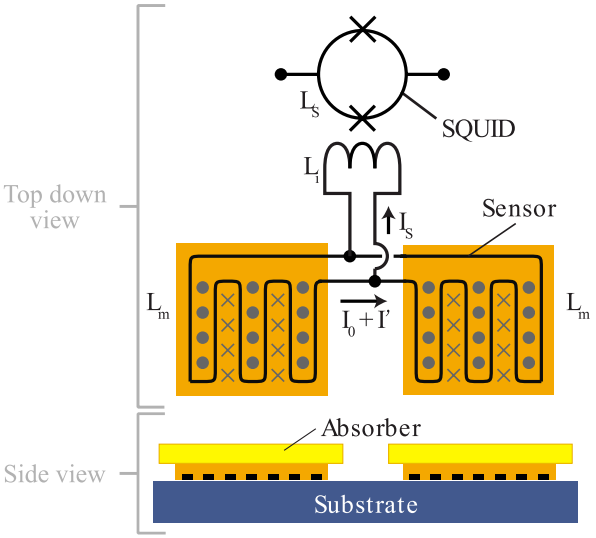

Fig. 5.8: Schematic diagram of superconducting sensor of two pixels, and read-out by a SQUID magnetometer, edited from [151, 232].

A signal from a pixel eventually induces a current through its input coil. This changes the flux in the sensor SQUID near to it, that is operated in voltage-bias mode. The flux change causes the current across the SQUID to drop. However, a single-stage dc-SQUID setup is prone to noise from the room temperature electronics (challenging the read out of small flux changes) and dc-SQUID-typical non-linear flux-to-voltage characteristics (even periodic depending on the flux change's magnitude) (for details see [232]). To improve the signal-to-noise ratio, a low-noise amplifier is necessary. The solution is to use a two-stage SQUID setup (see figure 5.9). The current drop across the first single SQUID is transmitted via another coil, inducing a change in magnetic flux, to a second-stage low-temperature series-SQUID-array. This array is operated with a bias current and in phase, so it acts like a single SQUID, amplifying a voltage drop proportional to the number of array-SQUIDs. The second-stage SQUID array is connected to room-temperature read-out and amplifier electronics.

To compensate for dcSQUID-typical non-linear flux-to-voltage characteristics, the setup uses a 'flux-locked-loop'. This means that a feedback resistance R_{fb} feeds the integrated

voltage change back to a coil near the first-stage single SQUID (see figure 5.9). This induces a compensating flux in the SQUID, so it is kept at its so-called 'working point' (the same point of the flux-to-voltage characteristics). Since the voltage drop across the feedback resistor is proportional to the flux change, it is digitised and saved as linearised output signal (see [232]).

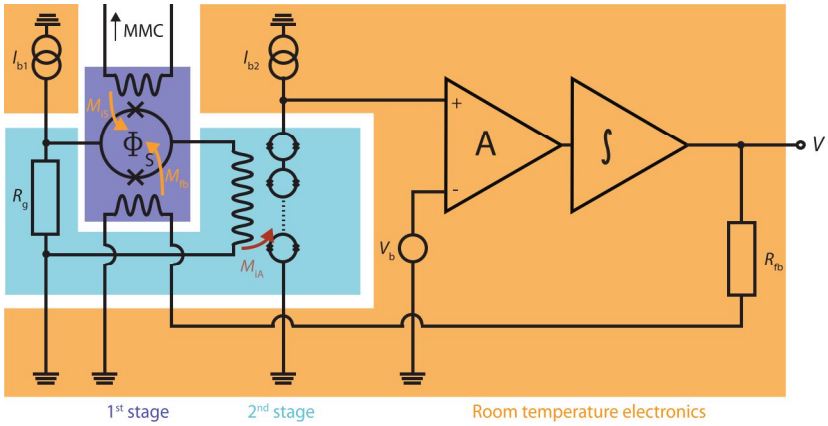

Fig. 5.9: Schematic diagram of the MMC two-stage read-out setup. The first-stage SQUID connected to the MMC detector is marked by a violet, the second-stage SQUID-array by a blue, and the room-temperature read-out-electronics by an orange background. The illustration is taken from [232].

MMCs of type maXs

The two MMC detectors deployed in the experiment of this work were of the type 'Micro-calorimeter Arrays for high resolution X-ray Spectroscopy (maXs)', standing for Micro-Calorimeter Arrays for High Resolution X-ray Spectroscopy [239, 232]. They were developed in collaboration between Heidelberg University and the Helmholtz Institute Jena [49, 240, 241, 242] as part of SPARC [50]. The underlying MMC technology combines a high energy resolution with a fast intrinsic rise time [243], as well as a broad spectral range. The unique combination of these characteristics make maXs-type detectors a particularly promising tool for a multitude of precision x-ray spectroscopy experiments, especially for high photon energies and broad spectral bandwidths that are challenging for crystal spectrometers. For the heat capacities, magnetisation and thermal noise to result in an acceptable signal-to-noise ratio, maXs detectors have to be operated at typical temperatures of $\leqslant 20\,\mathrm{mK}$. Therefore, each detector together with their two staged SQUID-readout electronics was embedded in a commercial ^{3}He/^{4}He

dilution cryostat, delivered by 'Bluefors'[7] (see figure 5.10). Operation of the cryostat required a unit for the gas handling, connected to the control system. The several hundred kg heavy cryostat was mounted in a frame at beam path level (reported in [244, 141]).

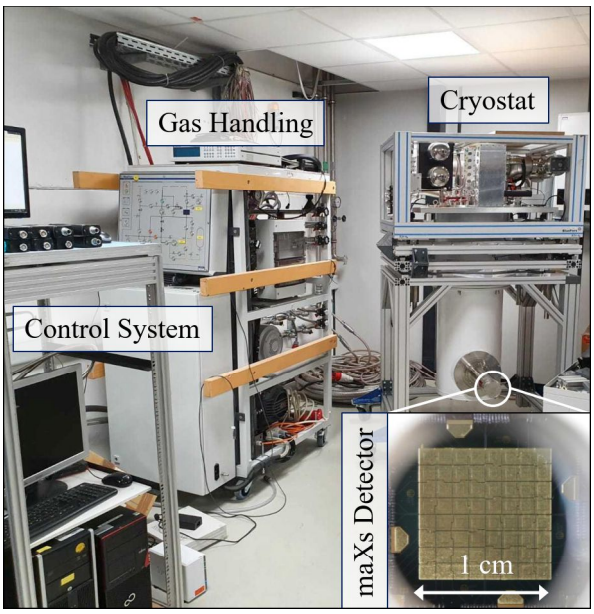

Fig. 5.10: Setup to operate a maXs-detector, edited from [193].

In general, the maXs detector system features a modular design, which allows the installation of different detector heads, optimised for specific experimental requirements with respect to active area, photopeak efficiency, and spectral resolution. While a small detector volume with a correspondingly small heat capacity is e.g. beneficial for the signal-to-noise ratio and higher resolution (section 3.2), a larger absorber enables a larger solid angle coverage and provides a superior photopeak efficiency. Figure 5.11 shows the simulated photopeak efficiency for gold absorbers of different thicknesses as a function of the absorbed photon's energy. The selected balance of this trade-off distinguishes the various detectors of the maXs family [239].

For the experiment of this work, 'maXs-100' detectors were used [245], prepared with absorbers, tailored for spectroscopy of transitions into the K shell in heavy ions close to 100 keV photon energy (around 50 eV FWHM at 100 keV incident photon energy design value). They are made of electro-deposited gold (with $\Theta_{\mathrm{D,Au}} \approx 162\,\mathrm{K}$ [233]), due to its high thermal conductivity, easy micro-manufacturability, and high stopping power for photons. The absorbers had a thickness of 50 µm, providing an acceptable photopeak

[7]Bluefors Oy, Arinatie 10, 00370 Helsinki, Finland.

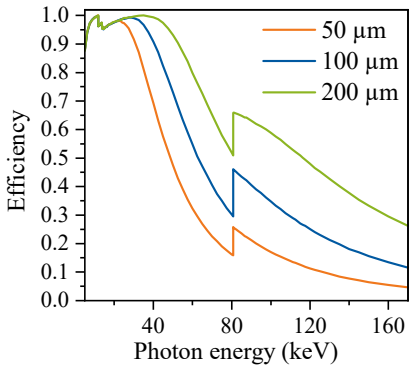

Fig. 5.11: Photopeak efficiency of gold absorbers of different thickness.

efficiency of $\sim 15\,\%$ and $\sim 20\,\%$ for the 180° and the 0° detector, respectively, for 100 keV x-rays in the emitter frame. The small absorber volume is achieved by reduction of its area, however, this also reduces the solid angle covered by the detector. To compensate the small detection area, the detector was composed of a 8×8 grid of practically 64 small detectors, each with an absorber of lateral dimensions of $1.25 \times 1.25\,\mathrm{mm}^2$, forming an effective detection area of $1\,\mathrm{cm}^2$. Since each pixel of a pixel-pair only generated either positive or negative signals (see description above), the 64 pixels shared in pairs one output cable. The 32 cables of one detector were connected to the data acquisition system (detailed description below).

5.2.5 Data acquisition system

To achieve a high resolution with the detectors, it is crucial to apply sophisticated pulse shape algorithms and various corrections to the measured data. The raw data analysis for the present work required to read out and store the complete trace of the detector pulses. Hence, the digitalisation of the detector signals differed from the analogue-electronics based Data AcQuisition (DAQ) system for semiconductor x-ray detectors, which was previously established in our group. There, the pulse shape analysis, both for energy and timing information, was performed on the hardware level. The new DAQ system required the inclusion of 'SIS3316' 16-bit digitisers from 'Struck Innovative Systeme'[8] [246] into the Multi Branch System (MBS)-based DAQ infrastructure of GSI [247], as we reported in [248]. Equipped with Analog-to-Digital Converter (ADC) chips, these Versa Module Eurocard (VME)-based cards each provide 16 analog input channels. Per channel, the module is able to generate a trigger signal

[8]Struck Innovative Systeme GmbH, Harksheider Str. 102, 22399 Hamburg, Germany.

with firmware-included constant fraction discrimination[9]. Per detector, the 32 cables from the 64 pixels (section 5.2.4) were connected to two 16-ADC-channel SIS3316 systems. These modules offer a sampling rate of 125 Megasamples per channel per second. However, to reduce the data volume, a mean value was determined over 16 samples. In addition to the two SIS3316 modules, a third was used to provide a channel for the CRYRING@ESR particle detector. All three modules were put into a VME crate, together with other modules, described in the following. The main module of the DAQ system was a RIO4 PowerPC (PPC) VME processor board. It was responsible for the configuration and readout of all other modules and directed the communication with the user and file saving. Adjacent to the RIO4 module, a TRIVA module was installed, which is as Trigger Synchronizing Module (or Master Trigger Module), able to start and stop the DAQ process. The next module was a VME Universal LOgic Module (VULOM) serving as dead-time locker and trigger priority encoder. Together, the TRIVA and VULOM module manage the acceptance and rejection of trigger signals from the rest of the DAQ system. In addition, the VULOM can act as Scaler and trigger generator. The setup also contained two ECC-NIM-ECL converter (ENV) modules. A VETAR2 module was used to enable access to the GSI/FAIR campus timing system (called 'White rabbit' [251, 252]). Figure 5.12 shows a schematic diagram of the DAQ system (which was identical for both setups at 0° and 180°). For configuration and readout of the VME-modules the standalone library framework `nurdlib` [253, 254] was used. While communication and data exchange between VME modules is done via the VMEbus backplane, the functions of the respective modules (e.g. saving counted data signals, or connecting a timestamp) are triggered by a trigger signal via external cabling. In the following, the trigger signal paths are explained with aid of figure 5.12.

Signals coming from the detectors or the experimental environment (1) are recorded by the detectors or instruments (2), and fed to the DAQ (black arrow). If a Struck module identifies an MMC signal to be an actual detection by crossing a certain threshold, a trigger signal (red arrow) is sent out (3). When it reaches the TRIVA module and is accepted (4), it triggers the data readout of the modules over the VMEbus backplane to the RIO4 (5). This induces a 'trigger accepted' signal (green arrow), which is sent

[9] A constant fraction discriminator divides a signal into two identical copies: one delayed and another inverted and reduced to a constant fraction. The zero crossing of their sum defines a precise trigger time of the original signal, independent of rise time and amplitude [249]. The principle was first implemented by an analog circuit in [250].

back (6) through the preceding modules to the Struck modules (7), which transmit the collected data from their buffers (via backplane), and to the VETAR2 module (8), which assigns a timestamp (via backplane). The data are then saved by the RIO4 (9).

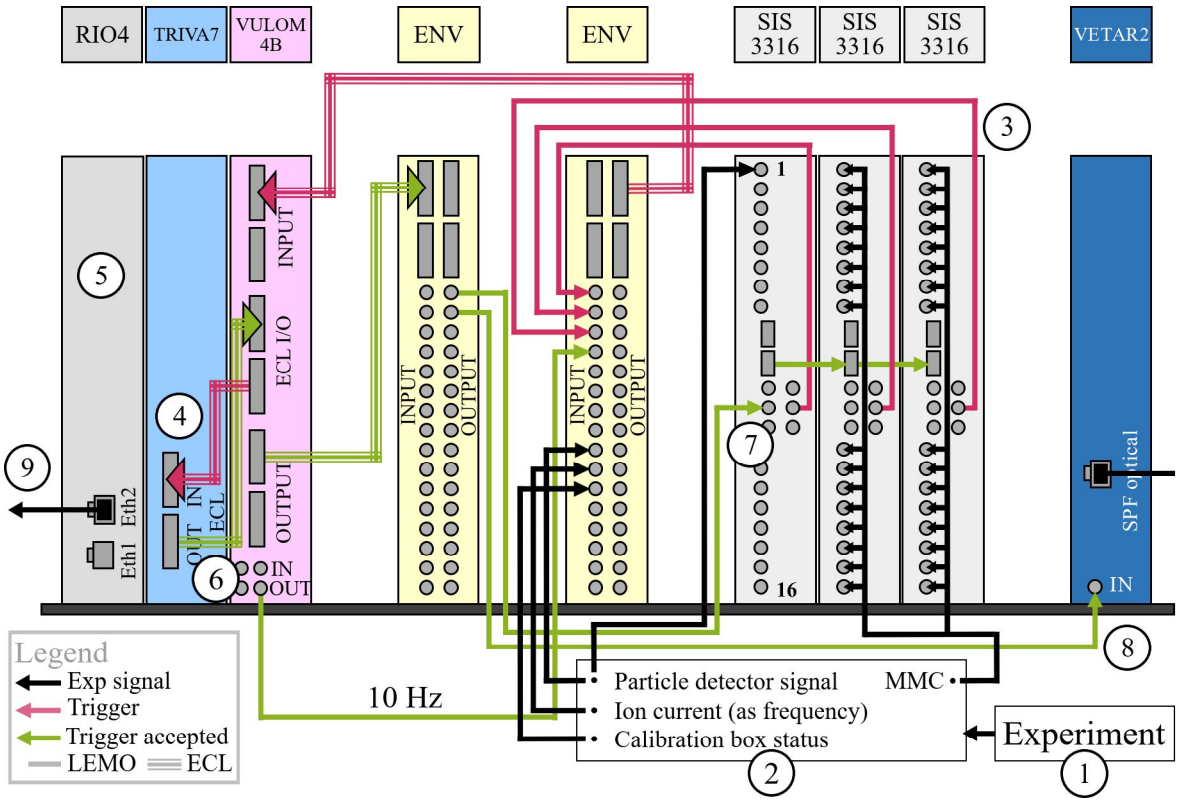

Fig. 5.12: Schematic diagram of a VME-based DAQ system for one of the MMC detectors.

It should be noted that the two Ge(i)-detectors, used for monitoring at the beginning of the experiment, had separate DAQ systems. Those also contained a RIO4 module. However, instead of the SIS3316 modules, a scaler, a Time-to-Digital Converter (TDC), and an ADC module were used. They were also integrated into the software environment of the MBS and used the `Go4` framework [255] for visualisation.

5.3 Spectroscopic measurement of helium-like uranium in 2021

In this section, the description of the beam time for the experiment of this work, and the raw data analysis with corresponding corrections, are presented. It concludes with

a (visual) comparison of a raw data analysed spectrum to a spectrum of a previous x-ray spectroscopic measurement, investigating the $\mathrm{N, M \rightarrow L}$ and $\mathrm{L \rightarrow K}$ transitions in heavy ions shown in section 4.2.1.

5.3.1 Beam time and experiment execution

Originally, the beam time for the experiment of this work was scheduled for 2020. Due to the Covid-19 crisis, however, it was delayed until 2021, as were many beam times at GSI. In 2020, a test experiment with lead ions Pb^{81+} was conducted instead, using Ge(i)-detectors in front of the then newly installed vacuum chambers, leading to the results we published in [228, 256].

In 2021, the x-ray spectroscopy experiment investigating the $\mathrm{N, M \rightarrow L}$ and $\mathrm{L \rightarrow K}$ transitions of helium-like uranium was conducted at the CRYRING@ESR. It's beam time followed the great success of the ESR measurement allowing to successfully investigate the $1s2p\,^3P_2 \rightarrow 1s2s\,^3S_1$ intra-shell transition in He-like uranium [42] (described in section 4.3.1). The CRYRING@ESR measurement was the first production run of the new GSI beam control system storing uranium ions in the CRYRING@ESR. The CRYRING storage ring was never before used to store uranium. In addition, it was unprecedented that U^{91+} was decelerated to 10.225 MeV/u and stored in a storage ring. Due to these circumstances, in spite of the great effort of the accelerator facility team, the two weeks of beam time were very challenging regarding the beam production and storage (see figure 5.13).

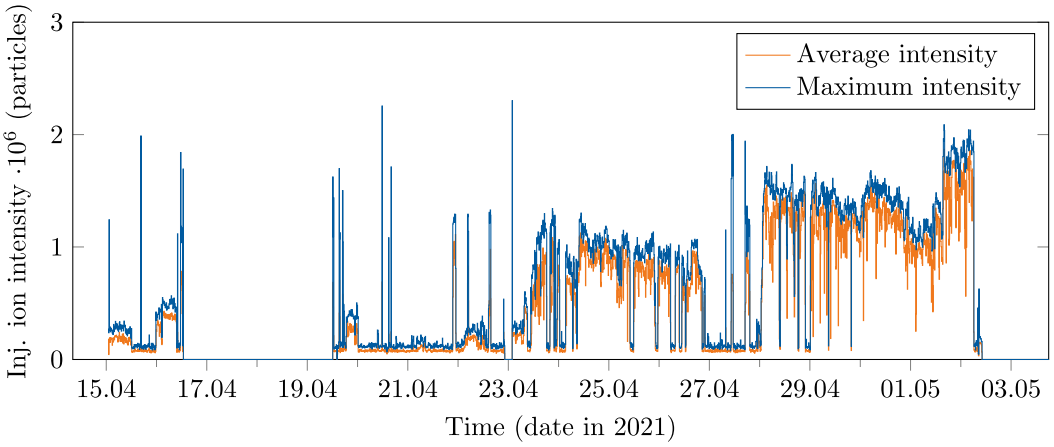

Fig. 5.13: Ion beam injection intensity in the CRYRING@ESR as a function of time, during the uranium beam time at the GSI facility in 2021.

The uranium ions were accelerated and stripped, using the UNILAC/SIS18 accelerators and stripper targets, to produce hydrogen-like uranium at 295 MeV/u. This resulted in a beam intensity of up to 10^9 ions per injection in the ESR, where the beam was cooled and decelerated down to 10.225 MeV/u. Next, the beam was transferred to the CRYRING@ESR, where, in the best case, an intensity of (1 to 2) $\cdot 10^6$ ions per injection was achieved (see [230]). There the beam was continuously cooled with an electron cooler voltage of 5634.5 V, generating an electron current of 30.5 mA, such that a lifetime of 7 to 8 s could be achieved for the ion beam. The injection cycle was determined to be approximately 55 s. Since after 25 s the stored beam was virtually gone, the remaining time could be used to conduct remote controlled calibration of the maXs detectors.

Obtaining low-resolution x-ray spectra with the Ge(i) detectors allowed to assess proper experimental conditions before starting a long accumulation of photon counts via MMCs. These detectors were then replaced by the maXs-detectors in front of the view ports (see figure 5.4). The quick signal rise time and timing capabilities of maXs detectors allowed, for the first time, a coincidence measurement with an MMC detector, achieving a time resolution of below 400 ns FWHM [220, 257] (illustrated by the black horizontal lines in figures 5.16 and 5.17 in section 5.3.3). This was made possible by using the CEM detector of the CRYRING@ESR as an additional particle counter detector, and by saving whole signal traces for the subsequent raw data analysis.

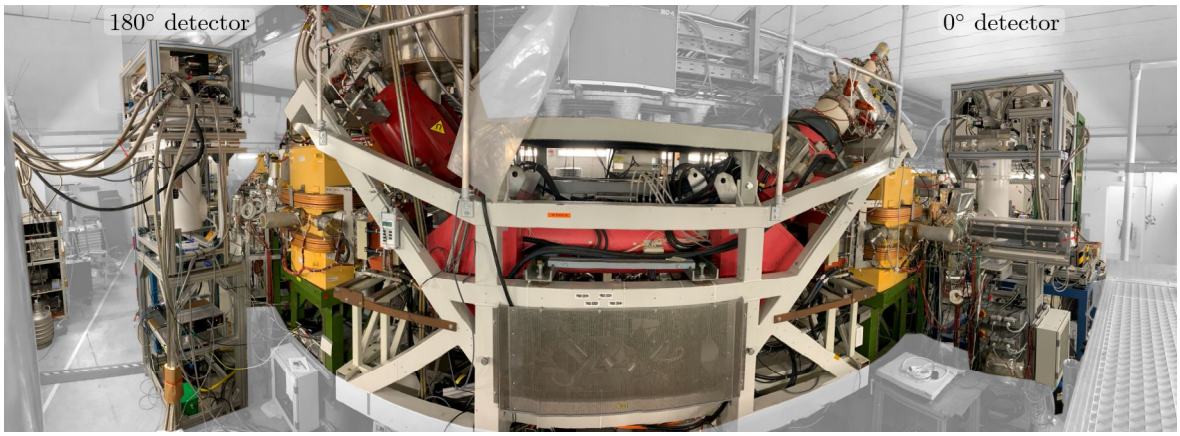

Fig. 5.14: Photograph of the setup installed at the CRYRING@ESR electron cooler during beam time in 2021. The picture is edited from [220].

While the described circumstances and challenges resulted in low x-ray counts, it was still possible to conduct the described x-ray measurement with success. Note that the

intensity achieved in the last few days was crucial for this success (see figure 5.13).

5.3.2 Pulse shape analysis

The following introduction to the raw data analysis is based on the description given in the thesis of M. O. Herdrich [78], who developed and established the analysis in our working group.

The signal traces obtained by the beam time in 2021 have to be processed by a pulse shape analysis, to extract signal amplitudes and timing information. Nowadays, this is done digitally, for MMC-signals often by application of an 'optimal filter' (see [237]). This digital filter uses a discrete Fourier-transformation of the detector signal and its detected noise for processing. Finally, it yields a finite response for a signal (therefore also called 'finite impulse response filter' (FIR)) in form of a signal-to-noise-ratio weighted mean value, independent of the detector response gain.

An optimal filter is most efficient and reliable for stable, time-isolated signals. Thus, it is suitable for signals obtained under (ideal) laboratory conditions. However, it lacks resilience against the many disturbances at storage rings, e.g. vibrations caused by accelerator parts and scattering at high electromagnetic fields. The desire to be more independent of hard-to-control fluctuations motivated the implementation of an alternative analysis filter. This lead to the adaptation of a raw data analysis approach, originally developed for scintillator and semiconductor detectors in the context of the *R3B*-program of the GSI (see [258]).

In contrast to an optimal filter, the applied pulse shape analysis deconvolutes the response-signal directly in time-space (no Fourier-transformation), by first applying a Moving Window Deconvolution (MWD)-filter [259, 260]. This produces a rectangular signal of the same width than the chosen filter-window and the same amplitude than the original signal. Then, the application of a Moving Average Filter (MAF) follows to average the deconvoluted signal-amplitudes of the rectangular signal. Similar to the optimal filter, the combined MWD-MAF filter eliminates the detector signal-response function. However, it only assumes an exponential signal decay and does not normalise the contributions according to the signal-to-noise ratio, therefore, making it less dependent on the signal stability at the expense of resolution.

Despite the pulse shape analysis, further modules are contained in the raw data analysis approach, allowing, among other things, the application of temperature correction and automated energy calibration. Together with some necessary filters, those elements are described in more detail below.

5.3.3 Photon spectra, filters and corrections

The raw data measured by the two MMC detectors exhibit every photon energy measured by the detectors over the beam time. However, the peaks of interest, coming from the electron transitions under investigation, are hidden by calibration photons and background noise from different sources. Therefore, the data were reduced only to those collected while the empty frame position was in use (during beam storage). The background noise was efficiently reduced by application of coincidence conditions. For that, first the traces of the MMC and CEM detectors and the according timestamps were used to investigate the signal arrival time of each photon and subsequent down-charged ion (see upper panels of figures 5.16 and 5.17). Then, a coincidence window was estimated for each detector and set to filter only for photon signals detected with a plausible delay-time to the next particle counter hit (denoted by horizontal lines in the figures). However, since there were multiple contemporaneous particle counter signals for some photons, those would be counted multiple times. Therefore, a duplicate filter was applied, which removed the multiplicity of MMC signals, having identical energy and time-stamp, to single counts.

To identify the actual energy in units of e.g. eV, the spectral lines had to be calibrated. For that, the calibration source photons measured with temporal proximity, so ideally with the same detector gain factor, served as a reference. However, the detector response function sometimes varied due to a change of the detector temperature, caused mostly by vibrations, or instability of the cryogenic system. A rise of an MMC's temperature influences its initial magnetisability, which means that further detected photons cause a different magnetisation (creating an energy offset).

Therefore, it was important to first apply a temperature correction to all the data. For that, the aforementioned raw data analysis approach included a correction algorithm (see [78]), enabling the identification of temperature gradients and plateaus. The software then compensated the data accordingly (see [141] for details).

The lower panels of figures 5.16 and 5.17 show the spectra resulting from the filtered, temperature corrected, calibrated data. The applied electron cooler voltage of $U = 5634.5\,\mathrm{V}$, determined the limit of lowest measurable energy (described in section 3.4) to be roughly 5 keV, which in the spectra was shifted according to the respective Doppler shift. What was left, besides a small amount of background noise, were transition peaks from U^{90+}, and some fluorescence peaks from the lead (Pb) shielding, visible e.g. between 70 and 80 keV in figure 5.16. However, in the following data analysis, only transition peaks were used, which could unambiguously be identified with certain electronic transitions in U^{90+}. For more details on the applied raw data corrections, see [220, 141, 131].

5.3.4 Comparison to a spectrum of a previous measurement of He-like uranium at the ESR

The improvements achieved in this new measurement, compared to the latest experiment described in section 4.2, become obvious in the direct comparison of the resulting data. Figure 5.15 shows that some isolated peaks in the Balmer-like region became visible for the first time. The novel precise data allowed the application of a new method for the Doppler correction, which is discussed in the next chapter.

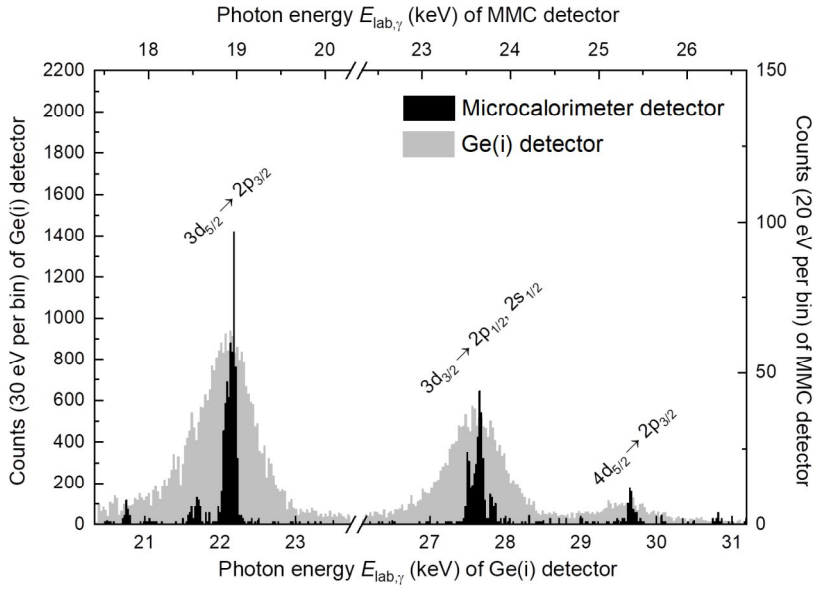

Fig. 5.15: Comparison of the N,M $\rightarrow$ L transitions in He-like uranium recorded in the context of this work by a maXs detector (at 0°) and in a previous measurement using a semiconductor detector [212], edited from [193].

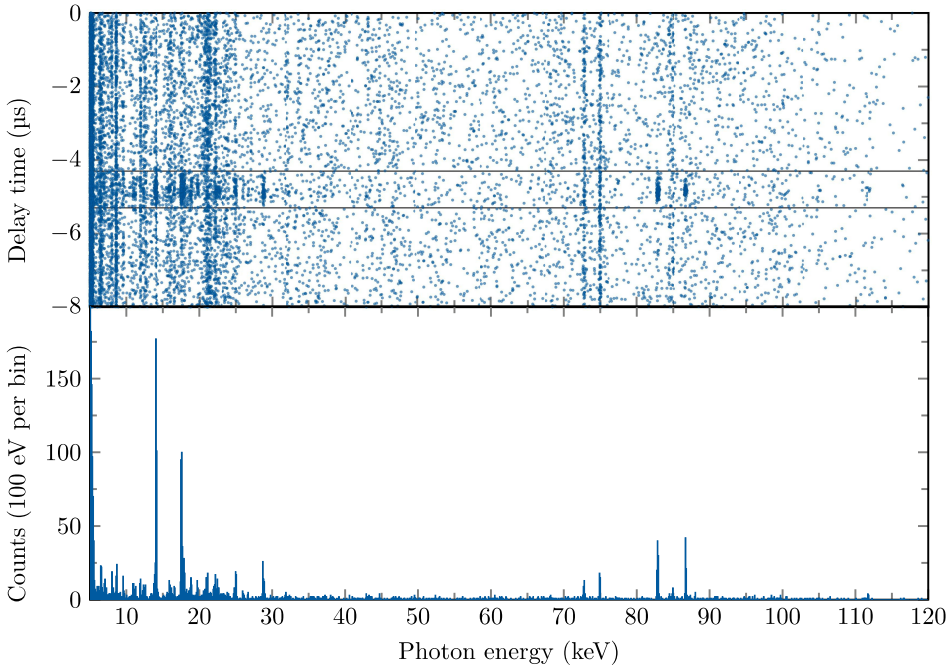

Fig. 5.16: Top) Time difference between the measurement of a photon at the 180° detector and a down-charged ion as a function of photon energy in keV. Bottom) Resulting spectra after all pulse-shape analysis steps.

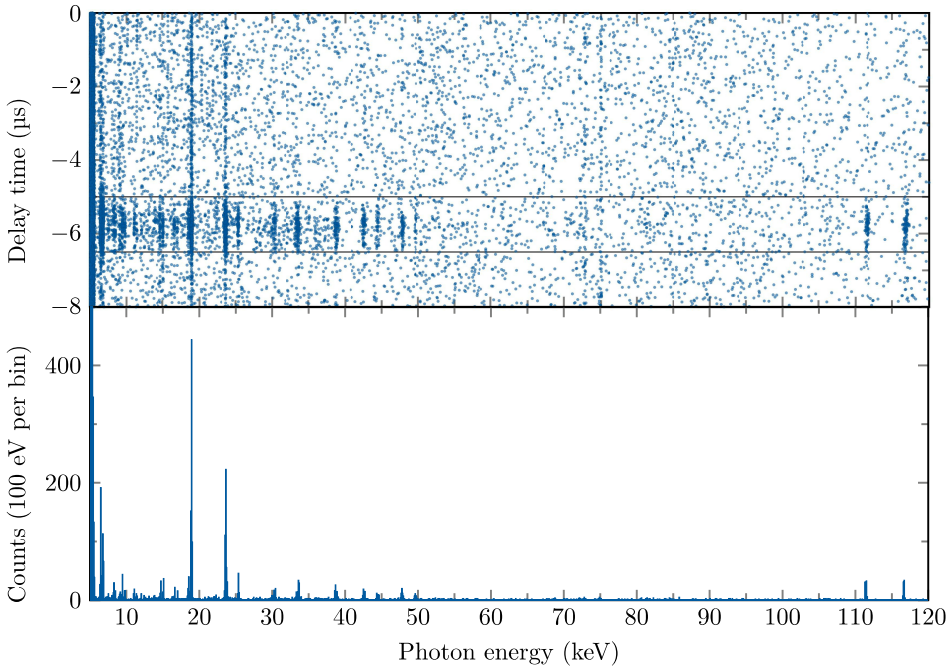

Fig. 5.17: Top) Time difference between the measurement of a photon at the 0° detector and a down-charged ion as a function of photon energy in keV. Bottom) Resulting spectra after all pulse-shape analysis steps.

6. X-ray spectra of He-like uranium: Analysis and results

In this chapter, the analysis and interpretation of the recorded x-ray photons from U^{90+} are discussed. First, the adjustment of a model to the spectral data, by application of a maximum likelihood minimisation is explained. This highly-resolved data, supported by latest theory values for transition energies and rates of relevant $N, M \rightarrow L$ and $L \rightarrow K$ transitions, allow the minimising procedure to yield a very precise estimation of the Doppler factor and hence the ion beam velocity (see section 3.6). This is compared to the ion velocity obtained through the traditional method, which relies on the voltage applied at the electron cooler. Next, two studies are presented: in the first, information on the relative populations of excited states in the N and M shell in U^{90+} were extracted from the $N, M \rightarrow L$ transitions data. This information was used to verify predictions resulting from a theoretical model consisting of RR calculations predicting the initial populations of excited states and an estimation model of the subsequent decay cascades. In the second study, the obtained $L \rightarrow K$ spectra were used for the first theory-supported experimental determination of the E1/M2 branching ratio of the $1s2p_{3/2}\,{}^3P_2$ level in U^{90+}, which is compared to theoretical predictions. Note that at the moment of writing this thesis, the publication of these data in a scientific journal is work in progress. Also, details on the study concerning the Kα transition energies and the ground state ionisation potential of He-like uranium can be found in [141, 131].

6.1 Analysis method

In the following, the data analysis focuses on the peaks within two regions of the U^{90+} spectrum: the $N, M \rightarrow L$ transitions energy region (ranging roughly from 10 keV to

30 keV), and the L → K (referred to as Kα) transitions energy region (at about 100 keV in the emitter frame). Since only peaks were considered that can unambiguously be assigned to specific transitions in U^{90+} a number of small peaks coming from several unresolved close-by transitions with low intensities were excluded. The upper panels of figures 6.1 and 6.2 show the experimental data for N, M → L and L → K transitions, respectively (as step-shaped black lines). The solid and dotted curved lines represent the results of the adjusted spectral model (described below).

Current theoretical data for the rates and energies of transitions originating from excited M and N shell states are listed in table 6.1, and in table 6.2 for the L shell states. The uncertainty for the transition rates can conservatively be estimated to be less than 15% (most being under 3%, and the highest uncertainties are from transitions which are not dominant at their initial states) [261]. The transition energies have a reported uncertainty of about $< \pm 2$ eV (for N, M→ L) and $< \pm 1$ eV (for L → K), respectively, and were used to assign the appropriate transitions to the respective peaks in the upper panels of figures 6.1 and 6.2. While the achieved spectral resolution allowed the observation of some peaks for the first time (see e.g. figure 5.15), it is still not sufficient to disentangle transitions separated by only a few eV. Note that due to the Doppler shift (section 3.6), line separation is additionally reduced for the red-shifted spectrum detected at 180° (visible in e.g. the three central peaks in the upper panel of figure 6.1). Therefore, peaks that are comprised of several close-by transitions were merged into an 'effective' peak in the spectral model. In those cases, the responsible prominent composing transitions share labels in the upper panel of figure 6.1. The respective properties of these effective peaks: their emitter system energy, intensity, and natural line width were calculated using the following formulas, and latest theoretical data on transition rates and energies listed in tables 6.1 and 6.2.

In the spectral model, the observed intensity I of a peak that is related to transitions from an excited initial state i in a final state f is determined by:

$$I = R_{\mathrm{tr,rel},i\to f} \cdot N_i, \tag{39}$$

with N_i being the integrated population of the excited state. The relative transition rate $R_{\mathrm{tr,rel},i\to f}$ is denoted as:

$$R_{\mathrm{tr,rel},i\to f} = \frac{R_{\mathrm{tr},i\to f}}{R_{\mathrm{tr,tot},i}}. \tag{40}$$

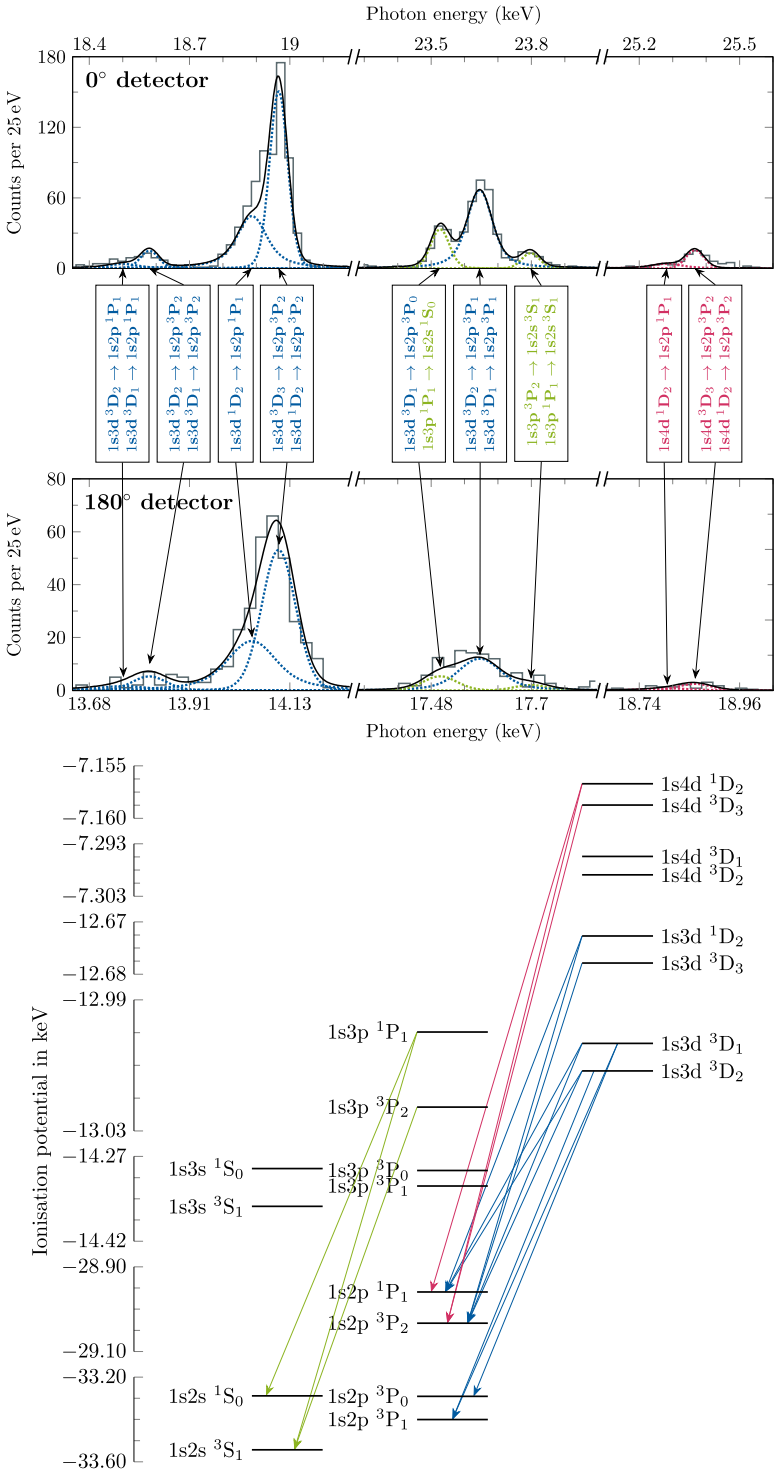

Fig. 6.1: Top) Spectral region of N, M → L transitions: experimental data (black steps) in comparison to the adjusted model (full black line), consisting of various Voigt-shaped peaks (coloured lines) and a constant background. Bottom) Level scheme of states in the L, M, N shells with the transitions that form the peaks in the panel above.

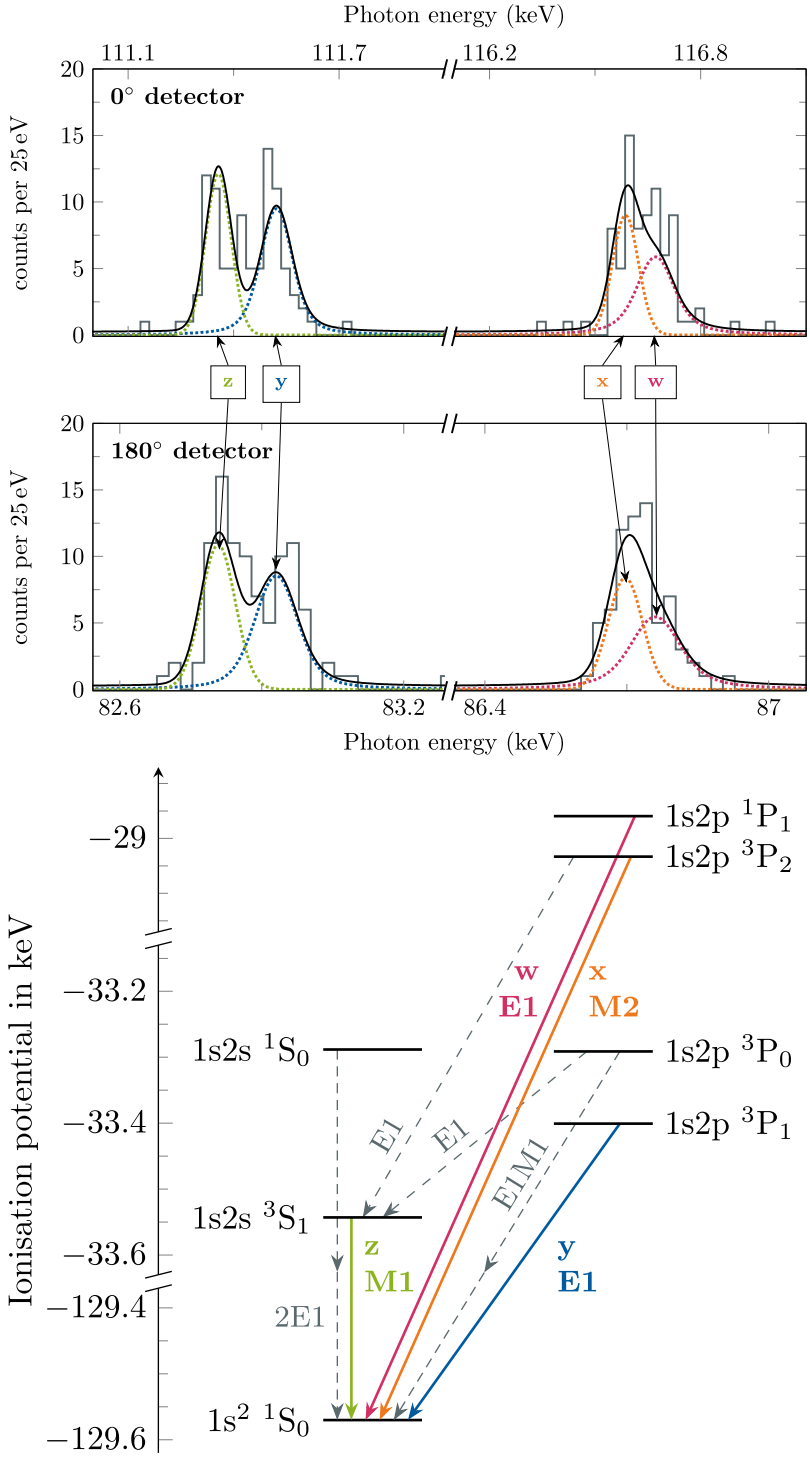

Fig. 6.2: Top) Spectral region of L → K (Kα) transitions: experimental data (black steps) in comparison to the adjusted model (full black line), consisting of various Voigt-shaped peaks (coloured lines) and a constant background. Bottom) Level scheme of states in the K and L shells with the transitions that form the peaks in the panel above.

Table 6.1: Theory values for $N, M \rightarrow M, L, K$ transitions in U^{90+}, relevant to this work. Only transitions with a relative contribution larger than 10^{-3} times the dominant transition rate from a given excited state were taken into account. The † symbol marks energies that were not directly taken from the literature, but calculated from binding energies published in the cited references. See body text for the uncertainties.

transition		type	energy in eV		rate in s^{-1}	
$1s4d\,^1D_2 \rightarrow$	$1s^2\,^1S_0$	E2	122413	[262]	1.58E+14	[263]
	$1s2p\,^3P_2$	E1	21877	[264]	1.42E+14	[264]
	$1s2p\,^1P_1$	E1	21803	[262]	1.27E+15	[262]
	$1s3p\,^3P_2$	E1	5865	[262]†	4.76E+13	[263]
	$1s3p\,^1P_1$	E1	5843	[262]†	4.28E+14	[263]
$1s4d\,^3D_3 \rightarrow$	$1s2s\,^3S_1$	E2	26384	[262]†	1.22E+13	[263]
	$1s2p\,^3P_2$	E1	21874	[262]	1.41E+15	[262]
	$1s3p\,^3P_2$	E1	5863	[262]†	4.75E+14	[263]
$1s3d\,^3D_3 \rightarrow$	$1s2s\,^3S_1$	E2	20865	[262]†	5.47E+13	[263]
	$1s2p\,^3P_2$	E1	16355	[262]	4.36E+15	[262]
$1s3d\,^1D_2 \rightarrow$	$1s^2\,^1S_0$	E2	116896	[262]	2.73E+14	[263]
	$1s2p\,^3P_2$	E1	16361	[262]	4.37E+14	[262]
	$1s2p\,^1P_1$	E1	16287	[262]	3.90E+15	[262]
$1s3d\,^3D_2 \rightarrow$	$1s^2\,^1S_0$	E2	116557	[262]	2.39E+14	[263]
	$1s2p\,^3P_1$	E1	20389	[262]	4.43E+15	[262]
	$1s2p\,^3P_2$	E1	16022	[262]	6.45E+14	[262]
	$1s2p\,^1P_1$	E1	15948	[262]	7.47E+13	[262]
$1s3d\,^3D_1 \rightarrow$	$1s2s\,^3S_1$	E2	20539	[262]†	5.27E+13	[263]
	$1s2p\,^3P_1$	E1	20398	[262]	1.48E+15	[262]
	$1s2p\,^3P_0$	E1	20288	[262]	2.94E+15	[262]
	$1s2p\,^3P_2$	E1	16030	[262]	1.19E+14	[262]
	$1s2p\,^1P_1$	E1	15956	[264]	5.92E+14	[264]
$1s3p\,^1P_1 \rightarrow$	$1s^2\,^1S_0$	E1	116570	[262]	1.46E+16	[263]
	$1s2s\,^3S_1$	E1	20543	[262]	3.73E+14	[262]
	$1s2s\,^1S_0$	E1	20289	[262]	7.76E+14	[262]
$1s3p\,^3P_2 \rightarrow$	$1s^2\,^1S_0$	M2	116547	[262]	7.56E+13	[263]
	$1s2s\,^3S_1$	E1	20520	[262]	1.14E+15	[262]
	$1s3s\,^3S_1$	E1	1341	[263]	1.40E+13	[263]

Table 6.2: Theory values for $L \rightarrow L, K$ transitions in U^{90+}, relevant to this work. Only transitions with a rate larger than 10^{-3} times the dominant transition rate from a given excited state were taken into account. The ‡ symbol marks energies, which were not directly taken from the literature, but calculated from binding energies published in the cited references. See body text for the uncertainties.

transition		type	energy in eV		rate in s^{-1}	
$1s2s\,^1S_0 \rightarrow$	$1s^2\,^1S_0$	2E1	-		7.20E+12	[265]
	$1s2p\,^3P_1$	E1	112.33	[118]‡	1.12E+09	[263]
	$1s2s\,^3S_1$	M1	254.69	[118]‡	1.17E+07	[263]
$1s2s\,^3S_1 \rightarrow$	$1s^2\,^1S_0$	M1	96027.07	[118]‡	1.24E+14	[263]
	$1s^2\,^1S_0$	2E1	-		2.57E+10	[265]
$1s2p\,^3P_0 \rightarrow$	$1s2p\,^3P_1$	M1	109.58	[118]‡	1.64E+07	[263]
	$1s2s\,^3S_1$	E1	251.94	[118]‡	1.17E+10	[263]
	$1s^2\,^1S_0$	E1M1	-		5.54E+09	[266]
$1s2p\,^3P_1 \rightarrow$	$1s^2\,^1S_0$	E1	96169.43	[118]‡	3.06E+16	[263]
$1s2p\,^1P_1 \rightarrow$	$1s^2\,^1S_0$	E1	100610.68	[118]‡	5.13E+16	[263]
	$1s2s\,^1S_0$	E1	4328.92	[118]‡	5.10E+13	[263]
	$1s2s\,^3S_1$	E1	4583.61	[118]‡	3.00E+13	[263]
$1s2p\,^3P_2 \rightarrow$	$1s^2\,^1S_0$	M2	100536.95	[118]‡	2.11E+14	[263]
	$1s2s\,^3S_1$	E1	4509.88	[118]‡	8.65E+13	[263]
	$1s2p\,^3P_1$	M1	4367.52	[118]‡	3.54E+11	[263]

It is the transition rate from i to f, divided by the sum of all relevant transition rates from the same initial state (i.e. taking into account all relevant decay channels of that state). For an effective peak, and all relevant $\{i, f\}$ combinations (of its responsible composing transition peaks), thus follows:

$$I_{\text{eff}} = \sum_{\{i,f\}} R_{\text{tr,rel},i\to f} \cdot N_i. \tag{41}$$

The transition energy of an effective peak is the weighted mean of all involved transition energies:

$$\overline{E}_{\text{eff}} = \frac{\sum_{\{i,f\}} R_{\text{tr,rel},i\to f} \cdot N_i \cdot E_{\text{tr},i\to f}}{I_{\text{eff}}}. \tag{42}$$

With formulas 32 and 34, in a similar way to the treatment of the energy of an effective peak, its natural linewidth can be determined by replacing $E_{\text{tr},i\to f}$ in formula 42 by $\Gamma_{\text{tr},i\to f}$:

$$\overline{\Gamma}_{\text{eff}} = \frac{\sum_{\{i,f\}} R_{\text{tr,rel},i\to f} \cdot N_i \cdot (R_{\text{tr,tot},i} + R_{\text{tr,tot},f}) \cdot \hbar}{I_{\text{eff}}}. \tag{43}$$

With the described treatment of effective peaks, a spectral model was constructed which included for the $\mathrm{N, M \to L}$ transitions, seven effective peaks and two single-transition peaks, and for the $\mathrm{L \to K}$ spectra four single-transition peaks. The free parameters of the spectral model were optimized through an adjustment algorithm (described below).

The adjustment algorithm was implemented using the Python adaptation `iminuit` [267, 268] (developed by Piti Ongmongkolkul) of the `Minuit2` C++ library [269], which is based on the `minuit` algorithm [270]. From this tool-kit, the extended unbinned Maximum-Likelihood (EML) method was applied (see [271]). In contrast to the standard Maximum-Likelihood (ML) method, the EML method relaxes the ML requirement that the integral of the probability density is normalised to 1, so that the peak intensities are treated as free parameters. Therefore, the sum of the intensities of all spectral features is not strictly required to equal the number of detected photons. The adjustment algorithm applies a probability density function, consisting of predefined profiles, which require characteristic parameters as input, set to be either fixed or free. In subsequent iterations, the algorithm then generates a cost function, which minimizes the negative logarithmic likelihood of the experimental data using the EML method by variation of the free parameters, while respecting their predefined conditions. To determine the uncertainties of the free parameters, `iminuit` includes the MINOS algorithm. This

allows to compute 'profile-likelihood' based (generally asymmetric) confidence intervals. Thus, it is able to treat one of the parameters as variable and scans the likelihood along it. Simultaneously, the algorithm minimises the likelihood with respect to all other parameters (see [268]). Note that the uncertainties given by the adjustment algorithm are purely of statistical nature.

To analyse the data of this work, Voigt profiles were chosen (see section 3.7) as probability density functions, together with a constant background. The profiles were implemented using [201]. Each individual Voigt peak required the following parameters: the peak position (here the peak energy), the peak intensity, as well as two width parameters, one for the Lorentzian component, i. e. the natural linewidth, and one for the Gaussian component, i. e. the detector energy resolution. The used input for these four parameters is described in the following.

For the peak positions in the emitter frame, corresponding to the photon energies, the theory values from tables 6.1 and 6.2 were taken. For effective peaks, they were calculated from those values using formula 42. The energies were then Doppler shifted into the laboratory system according to formula 28, introducing the beta value of the ion beam velocity, which was treated as a free parameter.

For the $\mathrm{N, M} \rightarrow \mathrm{L}$ transitions, the observed intensities were expressed through the formulas 39 and 41, with the transition rates (listed in table 6.1) as fixed, and the initial populations of the relevant excited states as free parameters. Thus, the adjustment procedure yields an estimate of the initial population of these excited states. Importantly, for the relevant excited states in the M and N shells, there are no significant intra-shell transitions, which redistribute electrons among them. Thus, the nine peaks in the upper panel of figure 6.1 depend on eight excited states. However, in the L shell, there is an E1 transition ($1s2p\,{}^3P_0 \rightarrow 1s2s\,{}^3S_1$), which significantly contributes to the population of the $1s2s\,{}^3S_1$ state. Thus, the initial population of five states determines the intensities of the four observed Kα transitions. As a consequence, it is not possible to reconstruct the population of excited L states from the observed Kα intensities, in the same way as for the M and N shell. Instead, the intensities of the four transitions themselves were used as free parameters for the minimisation, so their relative magnitudes could be compared to theory predictions. For each peak, the detector specific energy-dependant photopeak efficiency (section 5.2.4) was taken into account. In addition, the spectral model of the 180° detector was weighted with a factor f_I to account for any intensity

difference of this detector compared to the 0° detector. This can be due to different reasons. The most important are expected to be that: i) roughly one fourth of the pixels from the 180° detector had a malfunction going into the experiment, and ii) the Lorentz-transformed solid angle coverage yields a factor 0.74 for 180° and 1.34 for 0°.

For the Lorentzian component, the natural linewidths were calculated with formula 34, or for the effective peaks, with formula 43, using transition rates from tables 6.1 and 6.2. For the Gaussian component, i.e. the energy resolution of each detector, a linear dependence on the incident photon energy was assumed in the analysis:

$$r_{E,\mathrm{det}}(E_\gamma) = b_{\mathrm{det}} + (f_{\mathrm{det}} \cdot E_\gamma), \tag{44}$$

where b_{det} denotes a baseline energy resolution, and f_{det} a gradient factor. Both parameters were treated as free parameters for each of the two detectors. The linear assumption accounted for the fact that an imperfect correction of the temperature-dependent gain factor (discussed in section 5.3.3) would result in a deterioration of the spectral resolution, proportional to the photon energy. Indeed, for the 0° detector data, where the temperature information was unstable, such an effect is visible in the results (see table 6.3). In summary, the adjustment algorithm was provided with twenty free parameters: the ion velocity β, the intensity weighting factor f_I, the background intensity at each detector $I_{\mathrm{bg},0}$ and $I_{\mathrm{bg},180}$, the gradient factors f_0 and f_{180}, the baseline energies b_0 and b_{180}, eight populations $N_{\mathrm{p1-8}}$, and four intensities $I_{\mathrm{p9-12}}$.

The results of the combined analysis model of the experimental data for both detectors are illustrated in the upper panels of figure 6.1 and 6.2, for the $\mathrm{N, M \rightarrow L}$ and $\mathrm{L \rightarrow K}$ transitions, respectively. The total resulting function is depicted by a black curved line. The individual Voigt profiles of the peaks and effective peaks are depicted by colored dashed curved lines. The lower panels of the described figures show the responsible electron transitions, using the identical color scheme than used in the labels in the upper panels.

The upper panels of figures 6.1 and 6.2, respectively, show that reasonable agreement between the adjustment model and the experimental data was found. In table 6.3, the corresponding energy resolution results for each detector are presented, together with two examples of resulting energy resolutions at different energies, each chosen as an example energy typical for either the $\mathrm{N, M \rightarrow L}$, or the $\mathrm{L \rightarrow K}$ energy region.

Table 6.3: Parameters describing the detector energy resolutions, resulting from the adjustment of the spectral model to the recorded x-ray spectra of U^{90+}, according to formula 44 for each detector, with exemplary resolution values for typical energies of the $N, M \rightarrow L$ and the $L \rightarrow K$ energy region.

parameter	0° detector		180° detector	
f_{det}:	$2.7^{+1.1}_{-1.0} \cdot 10^{-4}$		$0.0^{+6.2}_{-0.0} \cdot 10^{-5}$	
b_{det}:	56.0 ± 4.0	eV FWHM	85.0 ± 5.0	eV FWHM
$r_{E,\mathrm{det}}(E_\gamma = 20\,\mathrm{keV})$:	≈ 61.4	eV FWHM	≈ 85.0	eV FWHM
$r_{E,\mathrm{det}}(E_\gamma = 111\,\mathrm{keV})$:	≈ 86.0	eV FWHM	≈ 85.0	eV FWHM

6.2 Result: Intrinsic Doppler correction

The conventional method to estimate the ion beam velocity, relies on a measurement of the externally applied voltage of the electron cooler (see section 3.6). For the 2021 beam time, that measurement found an electron cooler voltage of 5634.5(2.0) V. Taking into account the the space charge correction of the electron beam (see section 3.4 and [177]) results in a net acceleration voltage of 5609(2) V. By using formula 19, this corresponds to an ion beam velocity of $\beta = 0.146960(26)$. This method carries a sizeable systematic uncertainty due to the unknown contact potential between the surfaces of the cathode and the collector of the electron cooler, which for metal is conservatively estimated to be ± 2 V.

The analysis of the highly-resolved data of broad spectral range, recorded with the new experimental approach, enables for the first time the conduction of an intrinsic Doppler correction for a heavy ion storage ring experiment. Since the data were measured close to 0° and 180°, the Doppler shift is almost independent of the actual value of the observation angle (see section 3.6). Thus, the recorded spectra make it possible to directly determine the ion beam velocity through the aforementioned spectral model, resulting in $\beta = 0.147034(31)$. The uncertainty given by the adjustment algorithm is of statistical nature (see section 6.1). The beta value can be converted into an estimate of the acceleration voltage in the electron cooler using formula 19, resulting in $U = 5615(2)$ V. Table 6.4 shows a comparison of the results of both correction methods, and (for completeness' sake) also lists the corresponding γ-factor and the kinetic energy, calculated from the obtained values.

The comparison shows that, despite the very low photon count during the experiment,

Table 6.4: Resulting values of the ion beam velocity β, the γ-factor, the kinetic energy E_{kin}, and the corresponding voltage, extracted through different methods directly from the corresponding Doppler correction method (marked with †), or calculated from their respective result.

parameter	intrinsic determination		voltage divider	
β:	†0.147034(31)		0.146960(26)	
γ:	†1.0109880(47)		1.0109767(40)	
E_{kin}:	10.2365(4.4)	MeV/u	10.2260(3.7)	MeV/u
U:	5614.8(2.4)	V	†5609.0(2.0)	V

the statistical uncertainty (which also includes thermal fluctuations of the detectors) of the novel spectroscopic method is already close to the systematic uncertainty of the conventional method. The next step, was the identification and investigation of the systematic uncertainties of the novel method, that presumably describe that the uncertainty regions just do not overlap. The intrinsic estimation of the ion beam velocity from the observed Doppler shift strongly depends on an accurate knowledge of the line positions (peak energies) in the emitter frame. However, as stated in the captions of tables 6.1 and 6.2, the uncertainty of the available theory data is up to $\pm 2\,\mathrm{eV}$. And for a 20 keV photon (a typical energy for the Balmer-like region) the deviation of the ion beam velocities obtained from the two methods also amounts to the difference in the Doppler shift of about 2 eV. Another potential reason for the deviation are flaws in the energy calibration of the detectors, caused by the influence of signal digitisation artefacts on the spectral performance of the ADC-channels. In the literature, this is referred to as Integrated Non-Linearity (INL) of the ADCs. It describes the event, that for an ADC, a certain measured voltage is always mapped to the wrong bin (in contrast to an ideal ADC). The results of this work motivated an investigation of this effect by Daniel Müller (see [161]). In addition, the INL of ADCs continues to be subject of ongoing investigation.

In contrast to the hard-to-control uncertainties associated with the geometry of the experimental setup (for observation angles different from 0° and 180°) or the surface characteristics of cathode and collector anode of electron coolers, the aforementioned systematic effects are expected to be controllable following further investigation and improvement of the approach, e.g. by implementation of correction algorithms. Those improvements will be put to the test, together with studies to further identify and

quantise causes in a follow-up experiment (see chapter 7 for more details). Nevertheless, the here presented results successfully show that the new experimental approach indeed allows to conduct an intrinsic Doppler correction using the spectroscopic data. With enough photon counts and improvements regarding the experimental approach, it seems reasonable to predict that it should further reduce the uncertainty of the ion beam velocity. Thus, the intrinsic Doppler correction should become a valuable tool to verify or even exceed the conventional method, for which an improvement is not to be expected in the near future. Thus, the results highlight the important potential of the presented approach for all future similar heavy ion x-ray spectroscopy experiments where the Doppler correction is of concern.

6.3 Result: Relative M and N populations following radiative recombination

The visible $\mathrm{N, M \rightarrow L}$ transition peaks (see upper panel of figure 6.1) enable the experimental study of relative populations of excited U^{90+} states. For that purpose, the adjustment algorithm, supported by current theoretical predictions regarding transition rates, allows to extract information on the relative populations of excited states (see section 6.1), from which the transitions that were responsible for the observed photons originated. The resulting relative populations of the analysis are compared to theoretical predictions. Due to the scarcity of experimental and theoretical data for such heavy complex many-body systems, precise predictions for the populations are not available yet. Nevertheless, current theories allow a rough estimation at least, which is explained below.

The theoretical predictions were provided by Binghui Zhu, who combined a treatment of the initial population by the RR process with a calculation of the subsequent decay cascades (see [228, 256]). The model, originally developed for bare ions, was extended to also be applicable to initially H-like ions by approximately accounting for an additional electron in the ground state. The calculation of the direct RR population, as well as of the transition cascade, was separated into a non-relativistic treatment for $n > 10$ and a relativistic treatment for the more strongly bound states $n \leqslant 10$. For $n > 10$, RR was calculated using the recursive method introduced by Alan Burgess [191], with $Z = 91$ to approximately account for the shielding by the additional electron in the

ground state. Also for $n > 10$, the radiative rates for modeling the decay cascades were calculated through an E1 approximation. For $n \leqslant 10$, the RR process was treated by fully relativistic calculations (see [272]), and the radiative transition rates were calculated using the Flexible Atomic Code (FAC) [273, 274].

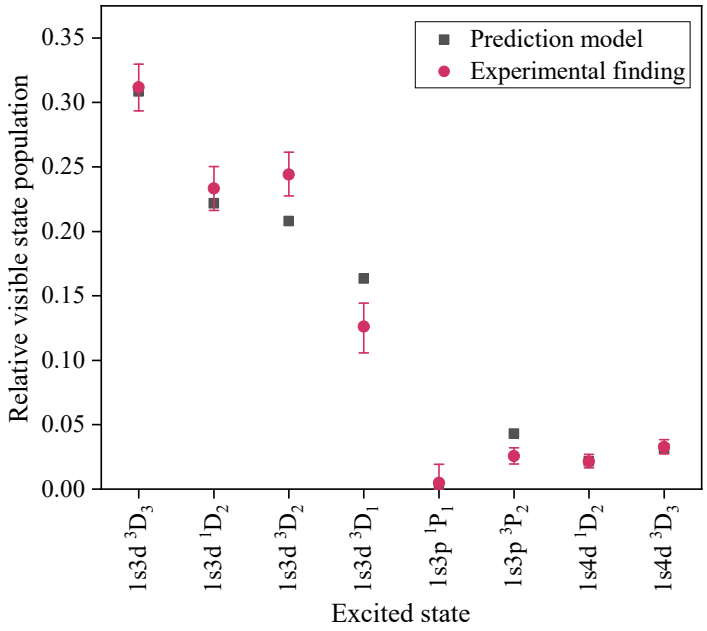

Fig. 6.3: Comparison between experimental findings and theoretical predictions (model presented in [228, 256]) of relative populations of initial states responsible for the observed $\mathrm{N, M} \rightarrow \mathrm{L}$ transitions (see body text for details).

In figure 6.3, the predictions by B. Zhu for the population of the eight excited states, relevant to the peaks observed in figure 6.1, are compared to the outcome of the adjustment procedure described in section 6.1. The figure shows that for most states, there is reasonable agreement between the model predictions and the experimental results. However, the states $1s3d\,^3D_1$, $1s3d\,^3D_2$ and $1s3p\,^3P_2$ show deviations from the experimental findings (roughly between 30 and 40%). Note that the provided values are relative, therefore any deviation of one relative population observed for a specific state has to be compensated by the relative population value/s of one or several other states.

While the experimental uncertainties are provided by the adjustment procedure, for the theory predictions, no uncertainties are given, because the theoretical model is only able to provide a rough estimate. Adding up the uncertainties of all relevant cascade transitions (from high n, l states up to at least $n = 100$) is not feasible, because it would require to obtain and propagate realistic uncertainties for the initial populations

of many thousands of excited states, and for all relevant transition rates. A significant uncertainty regarding the theory predictions cannot be ruled out.

Regarding the experimental uncertainty, the low photon count and detector temperature fluctuations are included in the statistical uncertainty given by the adjustment algorithm (see section 5.3.3). A systematic uncertainty imposed on the peak intensities arises, as for the ion beam velocity uncertainty discussed in section 6.2, from the INL of ADCs causing flaws in the calibration. An imperfect calibration of the energy axis results in shifted, compressed or widened peaks. Consequently, the adjustment algorithm is unable to accurately align the model peak positions with their actual (distorted) locations in the two spectra (at 0° and 180°). This introduces a systematic distortion in the estimated peak intensities. For the same reason, also the transition energy uncertainties from the supporting theory contribute to the overall systematic uncertainty. While for the peak intensities, the influence of the transition rate uncertainties (most being less than 3%, see section 6.1) from the supporting theory on the adjustment algorithm results is also systematic in nature, it is expected to be marginal. The possible causes are under ongoing investigation (also see [141, 131]), like e.g. the role of possible uncompensated temperature effects (inherent to the detectors). While a quantification of all different uncertainty effects is not feasible in this first measurement using the new experimental approach, it allowed their identification. This motivated measures, which are already in preparation for the next experiment, to reduce/eliminate factors that add to the uncertainty (see chapter 7). Moreover, this first ever theory-supported experimental insight into the relative populations of a heavy He-like system allowed a first benchmark of the described prediction model with the heaviest naturally occurring element.

6.4 Result: E1/M2 branching ratio of the 1s2p $^3P_2$ state

The intensity information on $L \rightarrow K$ transition peaks, obtained from the adjustment algorithm, allows another comparison with predictions (in this case of the relative intensity) from the aforementioned theoretical model for RR and transition cascades (section 6.3). Figure 6.4 shows that there is a discrepancy between the data and theory of 15 to 20%. The potential reasons for the deviations and uncertainties are the same as discussed in section 6.3. While there are deviations between the experimental findings

and predictions, there is no specific identifiable outlier. Again, since relative values are given, any deviation of one relative intensity has to be compensated by the relative intensity value/s from one or several other states.

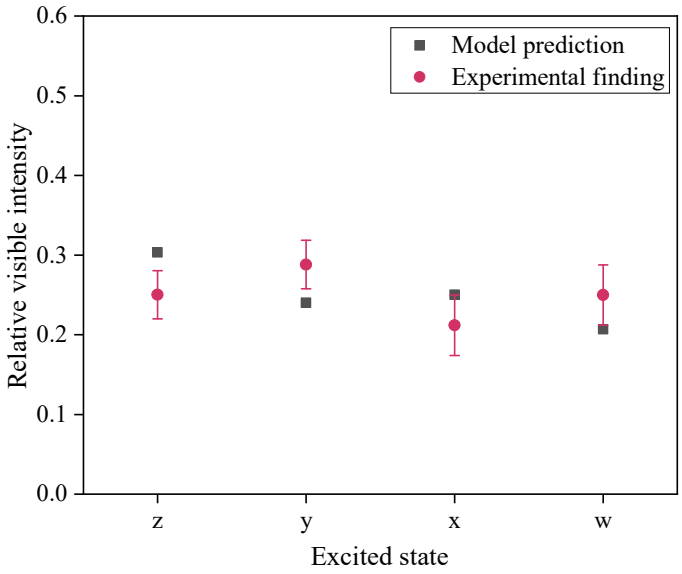

Fig. 6.4: Comparison between experimental findings and theoretical predictions (model presented in [228, 256]) of relative intensities from L shell states into the ground state (see body text for details).

The relative intensities found in this work enable a follow-up study: for the first time in a heavy He-like system, it allows to experimentally investigate the branching ratio of the $1s2p\,^3P_2$ state. This offers a unique opportunity, due to the fact that for transition rates in the 10^{14} to $10^{16}\,s^{-1}$ range a direct study via lifetime measurements tend to be unfeasible for strongly bound states of heavy systems (see section 2.3). Nevertheless, if the theoretical model for treating RR and cascades is sufficiently accurate, the measured intensities x (green line in figure 6.5) and z (orange line in figure 6.5) enable an experimental test of the relative strength of transition rates at least, so of the E1/M2 (blue and orange lines in figure 6.5) branching ratio of the $1s2p\,^3P_2$ state for He-like uranium. In the following, the data are used for such a test, assuming the theory predictions of the initial population of the L shell states are correct. The result then allows a comparison of the found branching ratio to the calculations of W. R. Johnson et al. [127] from 1995, which describe the E1 and the M2 transition rates from the $1s2p\,^3P_2$ state of He-like systems, depicted as a function of Z for $10 \leqslant Z \leqslant 100$ in the left-hand panel of figure 6.6. The theory values for the rates are expected to be accurate to 0.1% or better [127].

The transition rates of the E1 and M2 transitions originating from the $1s2p\,^3P_2$ state and the resulting branching ratio for a heavy Helium-like system have already been picked up as a subject of discussion in [143, 144]. A peculiarity of these two transition rates is that while in the mid-Z range, the M2 branch clearly dominates, for high-Z, it is expected that both transition rates converge towards very similar values, as is visible in the left-hand panel of figure 6.6. Thus, for U^{90+}, the feeding of the $1s2s\,^3S_1$ state by the intra-shell E1 transition from the $1s2s\,^3P_2$ state should significantly enhance the intensity of the subsequent z transition, while at the same time reducing the intensity of the x transition. This can now be verified by using the experimental data. So with the aforementioned assumption that the RR and cascade model is trustworthy and its predicted relative populations of the excited L states are correct, the measured photon intensities x and z allow to extract the E1/M2 branching ratio for the $1s2p\,^3P_2$ state.

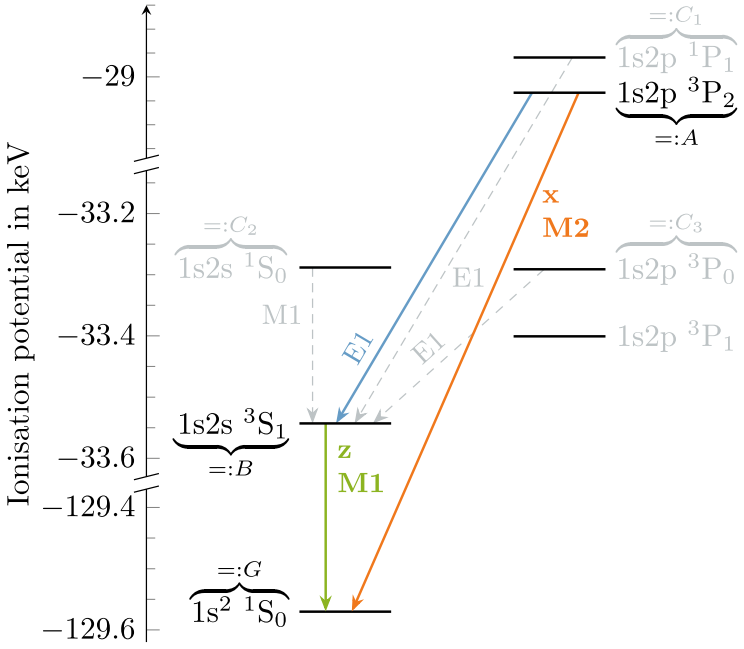

Fig. 6.5: Illustration of the branching decay of the state $1s2p_{3/2}\,^3P_2$ through the E1 and M2 transitions into the excited state $1s2s\,^3S_1$ and the ground-state, respectively. For each state, the letter by which it is referred to in the formulas is also given.

The following formulas, which describe the measured peak intensities x and z, allow to find an expression of the unknown relative rate from the initial state $1s2p\,^3P_2$ (henceforth referred to as A) to the final state $1s2s\,^3S_1$ (henceforth referred to as B) $R_{\mathrm{tr,rel},A\to B}$,

ultimately leading to an equation to find the ratio of E1/M2:

$$x \propto (R_{\mathrm{tr,rel},A\to G}) \cdot N_A = (1 - R_{\mathrm{tr,rel},A\to B}) \cdot N_A. \tag{45}$$

$$z \propto \underbrace{R_{\mathrm{tr,rel},B\to G}}_{\approx 1} \cdot (N_B + R_{\mathrm{tr,rel},A\to B} \cdot N_A + \underbrace{\sum_{m=1}^{3} R_{\mathrm{tr,rel},C_m\to B} \cdot N_{C_m}}_{=:S_{C_\mathrm{m}}}). \tag{46}$$

Formulas 45 and 46 allow to construct an equation to extract the unknown relative transition rate $R_{\mathrm{tr,rel},A\to B}$, only dependent on the theoretical relative populations and the measured photon intensities:

$$\frac{x}{z} = \frac{(1 - R_{\mathrm{tr,rel},A\to B}) \cdot N_A}{(N_B + R_{\mathrm{tr,rel},A\to B} \cdot N_A + S_{C_\mathrm{m}})} \iff R_{\mathrm{tr,rel},A\to B} = \frac{N_A - \frac{x}{z} \cdot (N_B + S_{C_\mathrm{m}})}{N_A \cdot (\frac{x}{z} + 1)}, \tag{47}$$

The expression found in formula 47 can then be inserted in the following equation to determine the E1/M2 branching ratio of $1s2p\,{}^3P_2$:

$$R_{\mathrm{tr,rel},A\to B} = \frac{\mathrm{E1}}{(\mathrm{E1{+}M2})} \iff \frac{\mathrm{E1}}{\mathrm{M2}} = \frac{R_{\mathrm{tr,rel},A\to B}}{1 - R_{\mathrm{tr,rel},A\to B}}. \tag{48}$$

Thus, with formula 48 the experimental data allow to extract the ratio of the E1 and the M2 transitions from the ratio of the x and z peak intensities, resulting in a first theory-supported experimental value for a heavy He-like system for the branching ratio of the $1s2p\,{}^3P_2$ state E1/M2 = 0.47. The experimental uncertainty can be determined through the equation for propagating uncertainties $\Delta f \approx \sqrt{(\frac{df}{dx})^2 \cdot (\Delta x)^2 + (\frac{df}{dz})^2 \cdot (\Delta z)^2}$, using for f the expression for E1/M2 in formula 48 and for $R_{\mathrm{tr,rel},A\to B}$ formula 47, and depending on the findings of x and z, which yields: $\Delta f \approx 0.17$. The theoretical prediction yields E1/M2 ≈ 0.42, and its uncertainty (calculated, using the equation for propagating uncertainties) is negligible (≈ 0.0006). The right-hand panel of figure 6.6 shows that the experimental finding for He-like uranium and the theoretical prediction agree (within the experimental uncertainty). So, the presented first experimental data point for a heavy system verifies the prediction of a convergence of the two transitions for high-Z systems. Improvements and refinements of the experimental method (further discussed in chapter 7), that lead to a reduction of the uncertainties imposed on the peak intensities, will in consequence also reduce the uncertainty of the theory-supported experimental determination of the branching ratio.

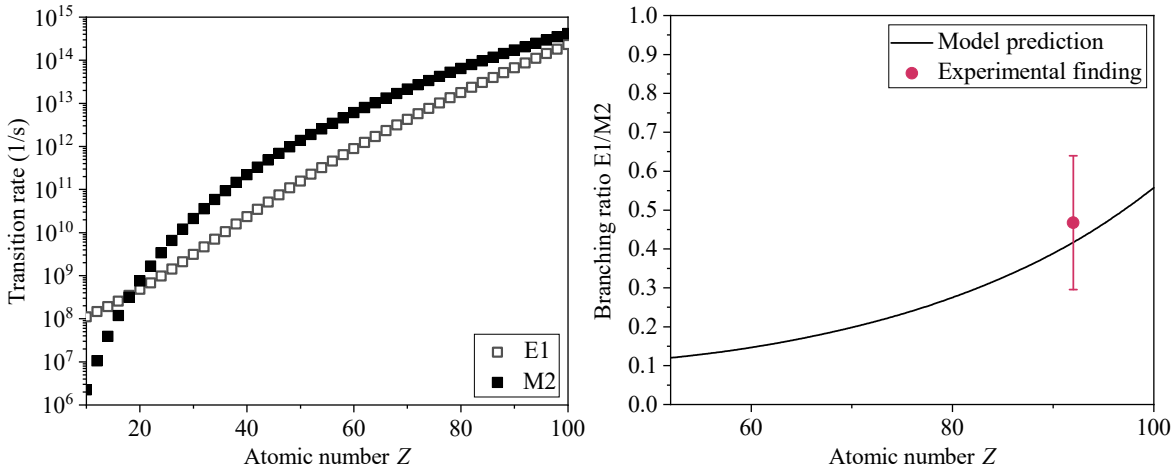

Fig. 6.6: Left) E1 and M2 transition rates of the 1s2p $^3P_2$ state of He-like systems as a function of Z, calculated by W. R. Johnson et al. [127]. The theoretical uncertainty is negligible. Right) Theory supported experimental finding for the E1/M2 branching ratio of He-like systems, compared to the ratio predicted by the rates from [127], shown in the left-hand panel.

7. Conclusion and outlook

The presented new experimental approach allowed to record photons, from radiative transitions in helium-like uranium, that had energies ranging from a few keV to above 100 keV with an unprecedented spectral resolution of better than 100 eV FWHM. The timing features of the novel detector technology were exploited to enable for the first time a coincidence technique with MMC detectors. Thus, a nearly 100% suppression of the radiation background was achieved, yielding very clean spectra of the U^{90+} transitions. The highly-resolved data in combination with the newly available 0° and 180° observation angles at the electron cooler of CRYRING@ESR enabled to conduct the first ever high-precision x-ray spectroscopy storage ring measurement with intrinsic Doppler correction. This allowed to eliminate hard-to-control systematic effects related to the observation angle as well as the ion beam velocity, which have always hampered this kind of storage ring experiments. The ion beam velocities (on which the Doppler factor depends) yielded by the intrinsic and conventional (via electron-cooler voltage) methods, are 0.147034(31) (statistical uncertainty given) and 0.146960(26) (systematic uncertainty given), respectively. Despite the low photon counts (due to the challenges explained below), the statistical uncertainty of the novel method is already of the same magnitude than the systematic uncertainty of the conventional method. While the uncertainty regions are not overlapping, this is presumably explained due to systematic uncertainties of the novel method (due to challenges imposed on the calibration caused by INL effects of the ADCs, and/or due to the uncertainty of the used theory data for the transition energies of up to ±2 eV. However, the overall systematic uncertainty is expected to be significantly reduced in a follow-up measurement described below).

Moreover, the broad spectral range of the used MMC detectors and their high energy resolution laid the foundation for two further studies. One presented a first insight into relative state-populations of several excited N and M states in He-like uranium,

allowing to benchmark a theory model for RR into predominantly high n, l states and the subsequent decay cascades. For most investigated states in the M and N shells reasonable agreement was found. The second study used the obtained $\mathrm{L} \rightarrow \mathrm{K}$ data to verify the E1/M2 branching ratio of the $1s2p\,^3P_2$ state of He-like uranium predicted by W. R. Johnson et al., confirming a ratio of roughly 42% (within the experimental uncertainty), and thus a convergence of the involved E1 and M2 transitions for high-Z systems.

The experimental challenges, observed deviations and their possible causes were discussed in this work. They are under ongoing investigation, but already motivated several improvements of the experimental approach. In the next measurement, the MMC detectors with 50 µm gold absorbers will be replaced by a new generation of MMCs, fabricated with 100 µm gold absorbers. The volume increase results in a significant higher stopping power (by roughly a factor 2). The photopeak efficiency is expected to increase by even more than a factor 2, since in addition to the increased stopping power, the loss due to escape events is reduced. Typically, a volume increase of the absorber results in a larger heat capacity at the cost of energy resolution. However, the group constructing the detectors determined that the energy resolution is not necessarily decreasing with the new absorbers, since the 50 µm gold absorbers were not operating at their physical limit. After refinement of the absorber fabrication process, the group is positive that the energy resolution could even be higher with the 100 µm gold absorbers than achieved with the 50 µm gold absorbers. Furthermore, the used pulse shape analysis filter has proven to be sub-optimal and will therefore be replaced by the 'optimal filter'. Also, the 180° cryostat-frame will be placed on a granite base (of 1.8 t) to reduce vibrations. The latter two changes should increase the effectiveness of the correction algorithm for detector-inherent non-linear temperature effects, which are further investigated. To get the non-linear behaviour of the ADCs and consequently challenges imposed on the calibration under control, another correction algorithm is currently being implemented. Last but not least, the low beam intensity (and hence the low photon counts) of the experiment presented in this work, was a result of it being one of the first beam times using the new GSI beam control system and the new CRYRING@ESR storage ring, and it was also the first time ever uranium was injected into the CRYRING, and that U^{91+} was decelerated and stored in a ring at an unprecedented energy of 10.225 MeV/u . However, meanwhile the accelerator facility shows improved performance following intense maintenance and hardware updates.

The improvements of the experimental approach will be put to the test in a follow-up experiment, with expected intensity increase. The beam time for this was already granted at the CRYRING@ESR, scheduled for July 2025. The results presented in this work allow a positive expectation for the upcoming experimental outcome. Besides the lessons learned to improve the approach, this work already granted access to gain first insights into the electronic dynamics of the He-like system of the heaviest naturally occurring element. The achievement of intrinsic Doppler correction marks a milestone for precision x-ray spectroscopy of fast-moving ions. Thus, it paves the way for the future spectroscopy storage ring experiments, bringing atomic physics research one step closer to probe 2nd order QED effects in the heaviest atomic systems.

List of abbreviations

ADC Analog-to-Digital Converter
CAD Computer Aided Design
CEM Channel Electron Multiplier
CERN Conseil Européen pour la Recherche Nucléaire
CoReLS Center for Relativistic Laser Science
CRYRING storage ring named after its original accelerator facility in Stockholm, that contained among other things a CRYogenic electron-beam ion source and this storage RING
DAQ Data AcQuisition
DR Dielectronic Recombination
EBIT Electron Beam Ion Trap
ESR 'ExperimentierSpeicherRing' (German for 'experimental storage ring')
FAC Flexible Atomic Code
FAIR 'Facility for Antiproton and Ion Research in Europe'
FOCAL FOcusing Compensated Asymmetric Laue
FWHM Full Width at Half Maximum
GIST Gwangju Institute of Science and Technology
GSI 'Gesellschaft für SchwerIonenforschung' (German for 'society for heavy ion research')
HESR 'HochEnergieSpeicherRing' (German for 'high energy storage ring')
HIRFL Heavy Ion Research Facility in Lanzhou
HITRAP Highly charged Ion TRAP
INL Integrated Non-Linearity
LEP Large Electron–Positron collider
LHC Large Hadron Collider
LIF Laser-Induced Fluorescence

MAF Moving Average Filter

maXs Micro-calorimeter Arrays for high resolution X-ray Spectroscopy

MBS Multi Branch System

MMC Metallic Magnetic microCalorimeter

MWD Moving Window Deconvolution

MWPC MultiWire Proportional Counter

NEG Non-Evaporable Getter

NRC Non-Radiative electron Capture

PPC PowerPC

QED Quantum ElectroDynamics

REC Radiative Electron Capture

RMBPT Relativistic Many-Body Perturbation Theory

RR Radiative Recombination

SIS100 SchwerIonenSynchrotron (German for 'heavy ion synchrotron') with a maximum magnetic rigidity of 100 Tm

SIS18 SchwerIonenSynchrotron (German for 'heavy ion synchrotron') with a maximum magnetic rigidity of 18 Tm

SOG Sum Of Gaussians

SPARC Stored Particles Atomic physics Research Collaboration

SQUID Superconducting QUantum Interference Device

TDC Time-to-Digital Converter

TES Transition-Edge-Sensor

UNILAC UNIversal Linear ACcelerator

VME Versa Module Eurocard

VULOM VME Universal LOgic Module

Bibliography

[1] J. J. Thomson. XXIV. On the structure of the atom: An investigation of the stability and periods of oscillation of a number of corpuscles arranged at equal intervals around the circumference of a circle; with application of the results to the theory of atomic structure. *The London, Edinburgh, and Dublin Philosophical Magazine and Journal of Science*, 7(39):237–265, 1904. doi:10.1080/14786440409463107.

[2] E. Rutherford. LXXIX. The scattering of α and β particles by matter and the structure of the atom. *The London, Edinburgh, and Dublin Philosophical Magazine and Journal of Science*, 21(125):669–688, 1911. doi:10.1080/14786440508637080.

[3] N. Bohr. I. On the constitution of atoms and molecules. *The London, Edinburgh, and Dublin Philosophical Magazine and Journal of Science*, 26(151):1–25, 1913. doi:10.1080/14786441308634955.

[4] N. Bohr. II. On the theory of the decrease of velocity of moving electrified particles on passing through matter. *The London, Edinburgh, and Dublin Philosophical Magazine and Journal of Science*, 25(145):10–31, 1913. doi:10.1080/14786440108634305.

[5] N. Bohr. LXXIII. On the constitution of atoms and molecules. *The London, Edinburgh, and Dublin Philosophical Magazine and Journal of Science*, 26(155): 857–875, 1913. doi:10.1080/14786441308635031.

[6] A. Sommerfeld. Zur Theorie der Balmerschen Serie. volume 3 of *Sitzungsberichte der mathematisch-physikalischen Klasse der K.B. Akademie der Wissenschaften zu München*, pages 425–458. Verlag der Königlich Bayerischen Akademie der Wissenschaften, 1915. [English reprint: A. Sommerfeld. On the theory of the Balmer series. *EPJ H*, 39:157–177 (2014). doi:10.1140/epjh/e2013-40053-8].

[7] A. Sommerfeld. Die Feinstruktur der Wasserstoff- und der Wasserstoff-ähnlichen Linien. volume 3 of *Sitzungsberichte der mathematisch-physikalischen Klasse der K.B. Akademie der Wissenschaften zu München*, pages 459–500. Verlag der Königlich Bayerischen Akademie der Wissenschaften, 2015. [English reprint: A. Sommerfeld. The fine structure of hydrogen and hydrogen-like lines. *EPJ H*, 39:179–204 (2014). doi:10.1140/epjh/e2013-40054-0].

[8] A. Sommerfeld. Zur Quantentheorie der Spektrallinien. *Annalen der Physik*, 356 (17):1–94, 1916. doi:10.1002/andp.19163561702.

[9] E. Schrödinger. Quantisierung als Eigenwertproblem (Erste Mitteilung). *Annalen der Physik*, 384(4):361–376, 1926. doi:10.1002/andp.19263840404.

[10] E. Schrödinger. Quantisierung als Eigenwertproblem (Zweite Mitteilung). *Annalen der Physik*, 384(6):489–527, 1926. doi:10.1002/andp.19263840602.

[11] E. Schrödinger. Quantisierung als Eigenwertproblem (Dritte Mitteilung). *Annalen der Physik*, 385(13):437–490, 1926. doi:10.1002/andp.19263851302.

[12] E. Schrödinger. Quantisierung als Eigenwertproblem (Vierte Mitteilung). *Annalen der Physik*, 386(18):109–139, 1926. doi:10.1002/andp.19263861802.

[13] H. Geiger and E. Marsden. On a diffuse reflection of the α-particles. *Proceedings of the Royal Society of London. Series A, Containing Papers of a Mathematical and Physical Character*, 82(557):495–500, 1909. doi:10.1098/rspa.1909.0054. [Communicated by E. Rutherford].

[14] A. Brunning. The history of the atom – theories and models, 2016. URL `https://www.compoundchem.com/2016/10/13/atomicmodels/`. [Accessed on: 05.02.2025].

[15] W. E. Lamb Jr. and R. C. Retherford. Fine structure of the hydrogen atom by a microwave method. *Physical Review*, 72(3):241–243, 1947. doi:10.1103/PhysRev.72.241.

[16] P. Indelicato. QED tests with highly charged ions. *Journal of Physics B: Atomic, Molecular and Optical Physics*, 52(23):232001, 2019. doi:10.1088/1361-6455/ab42c9.

[17] P. Kusch and H. M. Foley. The magnetic moment of the electron. *Physical Review*, 74(3):250–263, 1948. doi:10.1103/PhysRev.74.250.

[18] H. A. Bethe. The electromagnetic shift of energy levels. *Physical Review*, 72(4): 339–341, 1947. doi:10.1103/PhysRev.72.339.

[19] R. P. Feynman. Space-time approach to quantum electrodynamics. *Physical Review*, 76(6):769–789, 1949. doi:10.1103/PhysRev.76.769.

[20] R. P. Feynman. The theory of positrons. *Physical Review*, 76(6):749–759, 1949. doi:10.1103/PhysRev.76.749.

[21] J. Schwinger. On quantum-electrodynamics and the magnetic moment of the electron. *Physical Review*, 73(4):416–417, 1948. doi:10.1103/PhysRev.73.416.

[22] J. Schwinger. Quantum electrodynamics. I. A covariant formulation. *Physical Review*, 74(10):1439–1461, 1948. doi:10.1103/PhysRev.74.1439.

[23] J. Schwinger. Quantum electrodynamics. II. Vacuum polarization and self-energy. *Physical Review*, 75(4):651–679, 1949. doi:10.1103/PhysRev.75.651.

[24] J. Schwinger. Quantum electrodynamics. III. The electromagnetic properties of the electron—Radiative corrections to scattering. *Physical Review*, 76(6):790–817, 1949. doi:10.1103/PhysRev.76.790.

[25] S. Tomonaga. On a relativistically invariant formulation of the quantum theory of wave fields. *Progress of Theoretical Physics*, 1(2):27–42, 1946. doi:10.1143/PTP.1.27. [Appeared originally in Japanese in: S. Tomonaga. Bull. I. P. C. R. (Riken-iho), 22:545, 1943.].

[26] Z. Koba, T. Tati, and S. Tomonaga. On a relativistically invariant formulation of the quantum theory of wave fields. II: Case of interacting electromagnetic and electron fields. *Progress of Theoretical Physics*, 2(3):101–116, 1947. doi:10.1143/ptp/2.3.101.

[27] F. J. Dyson. The radiation theories of Tomonaga, Schwinger, and Feynman. *Physical Review*, 75(3):486–502, 1949. doi:10.1103/PhysRev.75.486.

[28] F. J. Dyson. The S matrix in quantum electrodynamics. *Physical Review*, 75(11): 1736–1755, 1949. doi:10.1103/PhysRev.75.1736.

[29] F. J. Dyson. Divergence of perturbation theory in quantum electrodynamics. *Physical Review*, 85(4):631–632, 1952. doi:10.1103/PhysRev.85.631.

[30] R. P. Feynman. *QED: The strange theory of light and matter*. Princeton University Press, 1988. ISBN 978-0-691-02417-2.

[31] T. Sailer, V. Debierre, Z. Harman, F. Heiße, C. König, J. Morgner, B. Tu, A. V. Volotka, C. H. Keitel, K. Blaum, and S. Sturm. Measurement of the bound-electron g-factor difference in coupled ions. *Nature*, 606(7914):479–483, 2022. doi:10.1038/s41586-022-04807-w.

[32] D. Hanneke, S. Fogwell, and G. Gabrielse. New measurement of the electron magnetic moment and the fine structure constant. *Physical Review Letters*, 100 (12):120801, 2008. doi:10.1103/PhysRevLett.100.120801.

[33] T. Aoyama, M. Hayakawa, T. Kinoshita, and M. Nio. Tenth-order QED contribution to the electron g-2 and an improved value of the fine structure constant. *Physical Review Letters*, 109(11):111807, 2012. doi:10.1103/PhysRevLett.109.111807.

[34] L. Morel, Z. Yao, P. Cladé, and S. Guellati-Khélifa. Determination of the fine-structure constant with an accuracy of 81 parts per trillion. *Nature*, 588(7836): 61–65, 2020. doi:10.1038/s41586-020-2964-7.

[35] J. Biesheuvel, J.-Ph Karr, L. Hilico, K. S. E. Eikema, W. Ubachs, and J. C. J. Koelemeij. Probing QED and fundamental constants through laser spectroscopy of vibrational transitions in HD^+. *Nature Communications*, 7(1):10385, 2016. doi:10.1038/ncomms10385.

[36] R. J. Rengelink, Y. van der Werf, R. P. M. J. W. Notermans, R. Jannin, K. S. E. Eikema, M. D. Hoogerland, and W. Vassen. Precision spectroscopy of helium in a magic wavelength optical dipole trap. *Nature Physics*, 14(11):1132–1137, 2018. doi:10.1038/s41567-018-0242-5.

[37] J. W. Yoon, Y. G. Kim, I. W. Choi, J. H. Sung, H. W. Lee, S. K. Lee, and C. H. Nam. Realization of laser intensity over 10^{23} W/cm^2. *Optica*, 8(5):630–635, 2021. doi:10.1364/OPTICA.420520.

[38] W. Heisenberg and H. Euler. Folgerungen aus der Diracschen Theorie des Positrons. *Zeitschrift für Physik*, 98(11):714–732, 1936. doi:10.1007/BF01343663.

[39] J. Schwinger. On gauge invariance and vacuum polarization. *Physical Review*, 82 (5):664–679, 1951. doi:10.1103/PhysRev.82.664.

[40] M. Buchanan. Past the Schwinger limit. *Nature Physics*, 2(11):721–721, 2006. doi:10.1038/nphys448.

[41] T. Beier. The g_j factor of a bound electron and the hyperfine structure splitting in hydrogenlike ions. *Physics Reports*, 339(2):79–213, 2000. doi:10.1016/S0370-1573(00)00071-5.

[42] R. Loetzsch, H. F. Beyer, L. Duval, U. Spillmann, D. Banaś, P. Dergham, F. M. Kröger, J. Glorius, R. E. Grisenti, M. Guerra, A. Gumberidze, R. Heß, P.-M. Hillenbrand, P. Indelicato, P. Jagodzinski, E. Lamour, B. Lorentz, S. Litvinov, Yu. A. Litvinov, J. Machado, N. Paul, G. G. Paulus, N. Petridis, J. P. Santos, M. Scheidel, R. S. Sidhu, M. Steck, S. Steydli, K. Szary, S. Trotsenko, I. Uschmann, G. Weber, Th. Stöhlker, and M. Trassinelli. Testing quantum electrodynamics in extreme fields using helium-like uranium. *Nature*, 625(7996):673–678, 2024. doi:10.1038/s41586-023-06910-y.

[43] H. F. Beyer, H.-J. Kluge, and V. P. Shevelko. *X-ray radiation of highly charged ions*. Springer-Verlag Berlin Heidelberg, 1997. ISBN 978-3-540-63185-9. doi:10.1007/978-3-662-03495-8.

[44] R. E. Marrs. Production of U^{92+} with an electron beam ion trap (invited). *Review of Scientific Instruments*, 67(3):941–944, 1996. doi:10.1063/1.1146646.

[45] C. Doppler. Über das farbige Licht der Doppelsterne und einiger anderer Gestirne des Himmels. volume 2 of *Abhandlungen der königlichen böhmischen Gesellschaft der Wissenschaften*, pages 465–482. Königliche böhmische Gesellschaft der Wissenschaften, 1842.

[46] T. Gassner, M. Trassinelli, R. Heß, U. Spillmann, D. Banaś, K.-H. Blumenhagen, F. Bosch, C. Brandau, W. Chen, Chr. Dimopoulou, E. Förster, R. E. Grisenti, A. Gumberidze, S. Hagmann, P.-M. Hillenbrand, P. Indelicato, P. Jagodzinski, T. Kämpfer, Chr. Kozhuharov, M. Lestinsky, D. Liesen, Yu. A. Litvinov, R. Loetzsch, B. Manil, R. Märtin, F. Nolden, N. Petridis, M. S. Sanjari, K. S. Schulze, M. Schwemlein, A. Simionovici, M. Steck, Th. Stöhlker, C. I. Szabo, S. Trotsenko, I. Uschmann, G. Weber, O. Wehrhan, N. Winckler, D. F. A. Winters, N. Winters,

E. Ziegler, and H. F. Beyer. Wavelength-dispersive spectroscopy in the hard x-ray regime of a heavy highly-charged ion: The 1s lamb shift in hydrogen-like gold. *New Journal of Physics*, 20(7):073033, 2018. doi:10.1088/1367-2630/aad01d.

[47] R. Loetzsch, H. F. Beyer, L. Duval, U. Spillmann, D. Banaś, P. Dergham, F. M. Kröger, J. Glorius, R. E. Grisenti, M. Guerra, A. Gumberidze, R. Heß, P.-M. Hillenbrand, P. Indelicato, P. Jagodzinski, E. Lamour, B. Lorentz, S. Litvinov, Yu A. Litvinov, J. Machado, N. Paul, G. G. Paulus, N. Petridis, J. P. Santos, M. Scheidel, R. S. Sidhu, M. Steck, S. Steydli, K. Szary, S. Trotsenko, I. Uschmann, G. Weber, Th Stöhlker, and M. Trassinelli. Testing quantum electrodynamics in extreme fields using helium-like uranium. *Nature*, 625(7996):673–678, 2024. doi:10.1038/s41586-023-06910-y.

[48] R. Lötzsch. Private communication, 2025.

[49] D. Hengstler, M. Keller, C. Schötz, J. Geist, M. Krantz, S. Kempf, L. Gastaldo, A. Fleischmann, T. Gassner, G. Weber, R. Märtin, Th. Stöhlker, and C. Enss. Towards FAIR: First measurements of metallic magnetic calorimeters for high-resolution x-ray spectroscopy at GSI. *Physica Scripta*, 2015(T166):014054, 2015. doi:10.1088/0031-8949/2015/T166/014054.

[50] Th. Stöhlker, Yu. A. Litvinov, A. Bräuning-Demian, M. Lestinsky, F. Herfurth, R. Maier, D. Prasuhn, R. Schuch, and M. Steck. SPARC collaboration: New strategy for storage ring physics at FAIR. *Hyperfine Interactions*, 227(1):45–53, 2014. doi:10.1007/s10751-014-1047-2.

[51] Stockholm University. History, manne siegbahn laboratory 1937-2011 [online], 2014-12-10. URL `https://www.msi.se/MSL_files/history.htm`.

[52] J. L. Marshall. Spectroscopy, 2019 international year of the periodic table (online). *Chem 13 News Magazine*, 2019. URL `https://uwaterloo.ca/chem13-news-magazine/october-2019/feature/spectroscopy`. [Accessed on: 01.10.2024].

[53] J. J. Balmer. Notiz über die Spectrallinien des Wasserstoffs. *Annalen der Physik*, 261(5):80–87, 1885. doi:10.1002/andp.18852610506.

[54] J. R. Rydberg. *Researches sur la constitution des spectres d'émission des éléments chimiques*, volume 23, Nr. 11 of *Kongliga Svenska Vetenskaps-Akademiens Handlingar*. Kongl. Boktryckeriet P. A. Norstedt & Söner, 2nd edition, 1889. URL `https://lucris.lub.lu.se/ws/portalfiles/portal/39556483/rydberg_1889_reduced_archived.pdf`.

[55] J. R. Rydberg. XXXIV. On the structure of the line-spectra of the chemical elements. *The London, Edinburgh, and Dublin Philosophical Magazine and Journal of Science*, 29(179):331–337, 1890. doi:10.1080/14786449008619945.

[56] H. Kragh. Concept and controversy: Jean Becquerel and the positive electron. *Centaurus*, 32(2):203–240, 1989. doi:10.1111/j.1600-0498.1989.tb00845.x.

[57] R. Laming. LXXVI. On the primary forces of electricity. *The London, Edinburgh, and Dublin Philosophical Magazine and Journal of Science*, 12(77):486–498, 1838. doi:10.1080/14786443808649498.

[58] J. J. Thomson. XL. Cathode rays. *The London, Edinburgh, and Dublin Philosophical Magazine and Journal of Science*, 44(269):293–316, 1897. doi:10.1080/14786449708621070.

[59] N. Bohr. *Rydberg's discovery of the spectral laws*. C.W.K. Gleerup (Lund), 1954. URL `https://portal.research.lu.se/en/publications/rydbergs-discovery-of-the-spectral-laws`.

[60] W. Ritz. Magnetische Atomfelder und Serienspektren. *Annalen der Physik*, 330 (4):660–696, 1908. doi:10.1002/andp.19083300403.

[61] M. Eckert. Die Geburt der modernen Atomtheorie. *Physik in unserer Zeit*, 44(4): 168–173, 2013. doi:10.1002/piuz.201301338.

[62] N. Bohr and L. Rosenfeld. *On the constitution of atoms and molecules*. Munksgaard, 1963. [Reprint of the papers of 1913 with introduction by L. Rosenfeld].

[63] J. W. Nicholson. The constitution of the solar corona. II. *Monthly Notices of the Royal Astronomical Society*, 72(8):677–693, 1912. doi:10.1093/mnras/72.8.677.

[64] H. Kragh. The genesis of Dirac's relativistic theory of electrons. *Archive for History of Exact Sciences*, 24(1):31–67, 1981. doi:10.1007/BF00327714.

[65] A. Kojevnikov. Dirac's quantum electrodynamics. In Y. Balashov and V. Vizgin, editors, *Einstein Studies in Russia*, volume 10 of *Einstein Studies*, pages 229–259. Birkhäuser Boston Basel Berlin, 2002. ISBN 978-0-8176-4263-1.

[66] O. Klein. Quantentheorie und fünfdimensionale Relativitätstheorie. *Zeitschrift für Physik*, 37(12):895–906, 1926. doi:10.1007/BF01397481.

[67] W. Gordon. Der Comptoneffekt nach der Schrödingerschen Theorie. *Zeitschrift für Physik*, 40(1):117–133, 1926. doi:10.1007/BF01390840.

[68] G. E. Uhlenbeck and S. Goudsmit. Spinning electrons and the structure of spectra. *Nature*, 117(2938):264–265, 1926. doi:10.1038/117264a0.

[69] C. G. Darwin. The electron as a vector wave. *Proceedings of the Royal Society of London. Series A, Containing Papers of a Mathematical and Physical Character*, 116(773):227–253, 1927. doi:10.1098/rspa.1927.0134.

[70] W. Pauli Jr. Zur Quantenmechanik des magnetischen Elektrons. *Zeitschrift für Physik*, 43(9):601–623, 1927. doi:10.1007/BF01397326.

[71] P. A. M. Dirac. The quantum theory of the electron. *Proceedings of the Royal Society of London. Series A, Containing Papers of a Mathematical and Physical Character*, 117(778):610–624, 1928. doi:10.1098/rspa.1928.0023.

[72] H. A. Bethe and E. E. Salpeter. *Quantum mechanics of one- and two-electron atoms*. Springer-Verlag Berlin Heidelberg, 1957. ISBN 978-3-662-12869-5. doi:10.1007/978-3-662-12869-5.

[73] W. E. Lamb Jr. and R. C. Retherford. Fine structure of the hydrogen atom. Part I. *Physical Review*, 79(4):549–572, 1950. doi:10.1103/PhysRev.79.549.

[74] W. E. Lamb Jr. and R. C. Retherford. Fine structure of the hydrogen atom. Part II. *Physical Review*, 81(2):222–232, 1951. doi:10.1103/PhysRev.81.222.

[75] W. E. Lamb Jr. Fine structure of the hydrogen atom. III. *Physical Review*, 85(2): 259–276, 1952. doi:10.1103/PhysRev.85.259.

[76] W. E. Lamb Jr. and R. C. Retherford. Fine structure of the hydrogen atom. IV. *Physical Review*, 86(6):1014–1022, 1952. doi:10.1103/PhysRev.86.1014.

[77] V. A. Yerokhin and V. M. Shabaev. Lamb shift of $n = 1$ and $n = 2$ states of hydrogen-like atoms, $1 \leqslant Z \leqslant 110$. *Journal of Physical and Chemical Reference Data*, 44(3):033103, 2015. doi:10.1063/1.4927487.

[78] M. O. Herdrich. *Anwendung kryogener Kalorimeter für hoch aufgelöste Präzisions-Röntgenspektroskopie*. PhD thesis, Friedrich-Schiller-Universität Jena, 2024. URL `https://repository.gsi.de/record/348991?ln=de`.

[79] G. E. Brown, J. S. Langer, and G. W. Schaefer. Lamb shift of a tightly bound electron I. Method. *Proceedings of the Royal Society of London. Series A. Mathematical and Physical Sciences*, 251(1264):92–104, 1997. doi:10.1098/rspa.1959.0092. [Communicated by R. E. Peierls].

[80] G. E. Brown and D. F. Mayers. Lamb shift of a tightly bound electron II. Calculation for the K-electron in mercury. *Proceedings of the Royal Society of London. Series A. Mathematical and Physical Sciences*, 251(1264):105–109, 1997. doi:10.1098/rspa.1959.0093.

[81] P. J. Mohr. Self-energy radiative corrections in hydrogen-like systems. *Annals of Physics*, 88(1):26–51, 1974. doi:10.1016/0003-4916(74)90398-4.

[82] P. J. Mohr. Numerical evaluation of the $1S_{1/2}$-state radiative level shift. *Annals of Physics*, 88(1):52–87, 1974. doi:10.1016/0003-4916(74)90399-6.

[83] K. T. Cheng and W. R. Johnson. Self-energy corrections to the k-electron binding in heavy and superheavy atoms. *Physical Review A*, 14(6):1943–1948, 1976. doi:10.1103/PhysRevA.14.1943.

[84] P. J. Mohr. Self-energy of the $n = 2$ states in a strong Coulomb field. *Physical Review A*, 26(5):2338–2354, 1982. doi:10.1103/PhysRevA.26.2338.

[85] P. J. Mohr. Self-energy correction to one-electron energy levels in a strong Coulomb field. *Physical Review A*, 46(7):4421–4424, 1992. doi:10.1103/PhysRevA.46.4421.

[86] P. J. Mohr and Y.-K. Kim. Self-energy of excited states in a strong Coulomb field. *Physical Review A*, 45(5):2727–2735, 1992. doi:10.1103/PhysRevA.45.2727.

[87] P. Indelicato and P. J. Mohr. 6s and 8d state self-energy for hydrogen-like ions and new results on the self-energy screening. *Hyperfine Interactions*, 114(1):147–153, 1998. doi:10.1023/A:1012622505367.

[88] É.-O. Le Bigot, P. Indelicato, and P. J. Mohr. QED self-energy contribution to highly excited atomic states. *Physical Review A*, 64(5):052508, 2001. doi:10.1103/PhysRevA.64.052508.

[89] E. A. Uehling. Polarization effects in the positron theory. *Physical Review*, 48(1): 55–63, 1935. doi:10.1103/PhysRev.48.55.

[90] E. H. Wichmann and N. M. Kroll. Vacuum polarization in a strong Coulomb field. *Physical Review*, 101(2):843–859, 1956. doi:10.1103/PhysRev.101.843.

[91] W. H. Furry. A symmetry theorem in the positron theory. *Physical Review*, 51 (2):125–129, 1937. doi:10.1103/PhysRev.51.125.

[92] G. W. F. Drake and R. A. Swainson. Bethe logarithms for hydrogen up to n=20 , and approximations for two-electron atoms. *Physical Review A*, 41(3):1243–1246, 1990. doi:10.1103/PhysRevA.41.1243.

[93] U. D. Jentschura and P. J. Mohr. Calculation of hydrogenic Bethe logarithms for Rydberg states. *Physical Review A*, 72(1):012110, 2005. doi:10.1103/PhysRevA.72.012110.

[94] P. J. Mohr, B. N. Taylor, and D. B. Newell. CODATA recommended values of the fundamental physical constants: 2010. *Reviews of Modern Physics*, 84(4): 1527–1605, 2012. doi:10.1103/RevModPhys.84.1527.

[95] K. Pachucki and U. D. Jentschura. Two-loop Bethe-logarithm correction in hydrogenlike atoms. *Physical Review Letters*, 91(11):113005, 2003. doi:10.1103/PhysRevLett.91.113005.

[96] U. D. Jentschura. Two-loop Bethe logarithms for non-S levels. *Physical Review A*, 74(6):062517, 2006. doi:10.1103/PhysRevA.74.062517.

[97] V. A. Yerokhin, P. Indelicato, and V. M. Shabaev. Two-loop self-energy correction in high-Z hydrogenlike ions. *Physical Review Letters*, 91(7):073001, 2003. doi:10.1103/PhysRevLett.91.073001.

[98] V. A. Yerokhin, P. Indelicato, and V. M. Shabaev. Two-loop QED corrections with closed fermion loops. *Physical Review A*, 77(6):062510, 2008. doi:10.1103/PhysRevA.77.062510.

[99] I. Angeli and K. P. Marinova. Table of experimental nuclear ground state charge radii: An update. *Atomic Data and Nuclear Data Tables*, 99(1):69–95, 2013. doi:10.1016/j.adt.2011.12.006.

[100] I. Angeli. A consistent set of nuclear rms charge radii: properties of the radius surface $R(N,Z)$. *Atomic Data and Nuclear Data Tables*, 87(2):185–206, 2004. doi:10.1016/j.adt.2004.04.002.

[101] L. C. Maximon and R. A. Schrack. The form factor of the Fermi model spatial distribution. *Journal of Research of the National Bureau of Standards Section B Mathematics and Mathematical Physics*, 70B(1):85, 1966. doi:10.6028/jres.070B.007.

[102] I. Sick. Model-independent nuclear charge densities from elastic electron scattering. *Nuclear Physics A*, 218(3):509–541, 1974. doi:10.1016/0375-9474(74)90039-6.

[103] H. De Vries, C. W. De Jager, and C. De Vries. Nuclear charge-density-distribution parameters from elastic electron scattering. *Atomic Data and Nuclear Data Tables*, 36(3):495–536, 1987. doi:10.1016/0092-640X(87)90013-1.

[104] G. Fricke, C. Bernhardt, K. Heilig, L. A. Schaller, L. Schellenberg, E. B. Shera, and C. W. Dejager. Nuclear ground state charge radii from electromagnetic interactions. *Atomic Data and Nuclear Data Tables*, 60(2):177–285, 1995. doi:10.1006/adnd.1995.1007.

[105] Y. Tanaka, R. M. Steffen, E. B. Shera, W. Reuter, M. V. Hoehn, and J. D. Zumbro. Systematics of ground-state quadrupole moments of odd-A deformed nuclei determined with muonic M x rays. *Physical Review C*, 29(5):1830–1838, 1984. doi:10.1103/PhysRevC.29.1830.

[106] J. D. Zumbro, E. B. Shera, Y. Tanaka, C. E. Bemis Jr., R. A. Naumann, M. V. Hoehn, W. Reuter, and R. M. Steffen. $E2$ and $E4$ deformations in ^{233,234,235,238}U. *Physical Review Letters*, 53(20):1888–1892, 1984. doi:10.1103/PhysRevLett.53.1888.

[107] M. W. Johnson, E. B. Shera, M. V. Hoehn, R. A. Naumann, J. D. Zumbro, and C. E. Bemis. ^{241}Am and ^{243}Am charge distributions from muonic x-ray spectroscopy and the quadrupole moment of the ^{240}Am fission isomer. *Physics Letters B*, 161(1):75–78, 1985. doi:10.1016/0370-2693(85)90612-4.

[108] J. D. Zumbro, R. A. Naumann, M. V. Hoehn, W. Reuter, E. B. Shera, C. E. Bemis, and Y. Tanaka. E2 and E4 deformations in ^{232}Th and ^{239,240,242}Pu. *Physics Letters B*, 167(4):383–387, 1986. doi:10.1016/0370-2693(86)91285-2.

[109] S. A. Blundell, W. R. Johnson, and J. Sapirstein. Improved many-body perturbation-theory calculations of the $n = 2$ states of lithiumlike uranium. *Physical Review A*, 41(3):1698–1700, 1990. doi:10.1103/PhysRevA.41.1698.

[110] Y. S. Kozhedub, O. V. Andreev, V. M. Shabaev, I. I. Tupitsyn, C. Brandau, C. Kozhuharov, G. Plunien, and Th. Stöhlker. Nuclear deformation effect on the binding energies in heavy ions. *Physical Review A*, 77(3):032501, 2008. doi:10.1103/PhysRevA.77.032501.

[111] G. Plunien and G. Soff. Nuclear-polarization contribution to the Lamb shift in actinide nuclei. *Physical Review A*, 51(2):1119–1131, 1995. doi:10.1103/PhysRevA.51.1119.

[112] N. Yamanaka, A. Haga, Y. Horikawa, and A. Ichimura. Nuclear polarization in hydrogenlike heavy ions. *Physical Review A*, 63(6):062502, 2001. doi:10.1103/PhysRevA.63.062502.

[113] G. Breit and G. E. Brown. Effect of nuclear motion on the fine structure of hydrogen. *Physical Review*, 74(10):1278–1284, 1948. doi:10.1103/PhysRev.74.1278.

[114] P. J. Mohr. Energy levels of hydrogen-like atoms predicted by quantum electrodynamics, $10 \leqslant Z \leqslant 40$. *Atomic Data and Nuclear Data Tables*, 29(3):453–466, 1983. doi:10.1016/S0092-640X(83)80002-3.

[115] W. R. Johnson and G. Soff. The lamb shift in hydrogen-like atoms, $1 \leqslant Z \leqslant 110$. *Atomic Data and Nuclear Data Tables*, 33(3):405–446, 1985. doi:10.1016/0092-640X(85)90010-5.

[116] A. N. Artemyev, V. M. Shabaev, V. A. Yerokhin, G. Plunien, and G. Soff. QED calculation of the $n = 1$ and $n = 2$ energy levels in He-like ions. *Physical Review A*, 71(6):062104, 2005. doi:10.1103/PhysRevA.71.062104.

[117] A. V. Malyshev, R. V. Popov, V. M. Shabaev, and N. A. Zubova. Nuclear recoil effect on the binding energies in highly charged He-like ions. *Journal of Physics*

B: Atomic, Molecular and Optical Physics, 51(8):085001, 2018. doi:10.1088/1361-6455/aab29f.

[118] Y. S. Kozhedub, A. V. Malyshev, D. A. Glazov, V. M. Shabaev, and I. I. Tupitsyn. QED calculation of electron-electron correlation effects in heliumlike ions. *Physical Review A*, 100(6):062506, 2019. doi:10.1103/PhysRevA.100.062506.

[119] H. Persson, S. Salomonson, P. Sunnergren, and I. Lindgren. Two-electron Lamb-shift calculations on heliumlike ions. *Physical Review Letters*, 76(2):204–207, 1996. doi:10.1103/PhysRevLett.76.204.

[120] A. N. Artemyev, T. Beier, G. Plunien, V. M. Shabaev, G. Soff, and V. A. Yerokhin. Vacuum-polarization screening corrections to the energy levels of heliumlike ions. *Physical Review A*, 62(2):022116, 2000. doi:10.1103/PhysRevA.62.022116.

[121] V. A. Yerokhin and V. M. Shabaev. Two-loop self-energy correction in H-like ions. *Physical Review A*, 64(6):062507, 2001. doi:10.1103/PhysRevA.64.062507.

[122] A. Gumberidze. *Experimental studies of the ground state QED corrections in H- and He-like uranium*. PhD thesis, Johann Wolfgang Goethe-Universität Frankfurt am Main, 2003. URL `https://web-docs.gsi.de/~stoe_exp/theses/theses.php`.

[123] O. Jitrik and C. F. Bunge. Atomic transition probabilities for Hydrogen-like atoms. URL `https://www.fisica.unam.mx/research/tables/spectra/1el/index.shtml`. [Accessed on: 28.01.2025].

[124] O. Jitrik and C. F. Bunge. Transition probabilities for hydrogen-like atoms. *Journal of Physical and Chemical Reference Data*, 33(4):1059–1070, 2004. doi:10.1063/1.1796671.

[125] O. Jitrik and C. F. Bunge. Salient features of electric and magnetic multipole transition probabilities of hydrogen-like systems. *Physica Scripta*, 2004. doi:10.1238/Physica.Regular.069a00196.

[126] R. V. Popov and A. V. Maiorova. Relativistic calculations of one-photon transition probabilities in hydrogen-like ions. *Optics and Spectroscopy*, 122(3):366–396, 2017. doi:10.1134/S0030400X1703016X.

[127] W. R. Johnson, D. R. Plante, and J. Sapirstein. Relativistic calculations of transition amplitudes in the helium isoelectronic sequence. In B. Bederson and H. Walther, editors, *Advances in atomic, molecular, and optical physics*, volume 35, pages 255–329. Academic Press, 1995. ISBN 978-0-12-003835-0. doi:10.1016/S1049-250X(08)60165-2.

[128] D. B. Thorn, G. V. Brown, J. H. T. Clementson, H. Chen, M. Chen, P. Beiersdorfer, K. R. Boyce, C. A. Kilbourne, F. S. Porter, and R. L. Kelley. High-resolution spectroscopy of K-shell praseodymium with a high-energy microcalorimeter. *Canadian Journal of Physics*, 86(1):241–244, 2008. doi:10.1139/p07-134.

[129] J. P. Briand, P. Chevallier, P. Indelicato, K. P. Ziock, and D. D. Dietrich. Observation and measurement of $n = 2 \rightarrow \mathrm{n} = 1$ transitions of hydrogenlike and heliumlike uranium. *Physical Review Letters*, 65(22):2761–2764, 1990. doi:10.1103/PhysRevLett.65.2761.

[130] J. H. Lupton, D. D. Dietrich, C. J. Hailey, R. E. Stewart, and K. P. Ziock. Measurements of the ground-state Lamb shift and electron-correlation effects in hydrogenlike and heliumlike uranium. *Physical Review A*, 50(3):2150–2154, 1994. doi:10.1103/PhysRevA.50.2150.

[131] Ph. Pfäfflein, G. Weber, S. Allgeier, Z. Andelkovic, S. Bernitt, A. I. Bondarev, A. Borovik, L. Duval, A. Fleischmann, O. Forstner, M. Friedrich, J. Glorius, A. Gumberidze, Ch. Hahn, F. Herfurth, D. Hengstler, M. O. Herdrich, P.-M. Hillenbrand, A. Kalinin, M. Kiffer, F. M. Kröger, M. Kubullek, P. Kuntz, M. Lestinsky, Yu. A. Litvinov, B. Löher, E. B. Menz, T. Over, N. Petridis, S. Ringleb, R. S. Sidhu, U. Spillmann, S. Trotsenko, A. Warczak, B. Zhu, Ch. Enss, and Th. Stöhlker. Quantum electrodynamics in strong electromagnetic fields: Substate resolved Kα transition energies in heliumlike uranium. *Physical Review Letters*, 134(15):153001, 2025. doi:10.1103/PhysRevLett.134.153001.

[132] C. T. Chantler, M. N. Kinnane, J. D. Gillaspy, L. T. Hudson, A. T. Payne, L. F. Smale, A. Henins, J. M. Pomeroy, J. N. Tan, J. A. Kimpton, E. Takacs, and K. Makonyi. Testing three-body quantum electrodynamics with trapped Ti^{20+} ions: Evidence for a Z-dependent divergence between experiment and calculation. *Physical Review Letters*, 109(15):153001, 2012. doi:10.1103/PhysRevLett.109.153001.

[133] S. W. Epp. Comment on "Testing three-body quantum electrodynamics with trapped Ti^{20+} ions: Evidence for a Z-dependent divergence between experiment and calculation". *Physical Review Letters*, 110(15):159301, 2013. doi:10.1103/PhysRevLett.110.159301.

[134] C. T. Chantler, M. N. Kinnane, J. D. Gillaspy, L. T. Hudson, A. T. Payne, L. F. Smale, A. Henins, J. M. Pomeroy, J. A. Kimpton, E. Takacs, and K. Makonyi. Chantler et al. Reply:. *Physical Review Letters*, 110(15):159302, 2013. doi:10.1103/PhysRevLett.110.159302.

[135] A. T. Payne, C. T. Chantler, M. N. Kinnane, J. D. Gillaspy, L. T. Hudson, L. F. Smale, A. Henins, J. A. Kimpton, and E. Takacs. Helium-like titanium x-ray spectrum as a probe of QED computation. *Journal of Physics B: Atomic, Molecular and Optical Physics*, 47(18):185001, 2014. doi:10.1088/0953-4075/47/18/185001.

[136] K. Kubiček, P. H. Mokler, V. Mäckel, J. Ullrich, and J. R. Crespo López-Urrutia. Transition energy measurements in hydrogenlike and heliumlike ions strongly supporting bound-state QED calculations. *Physical Review A*, 90(3):032508, 2014. doi:10.1103/PhysRevA.90.032508.

[137] C. T. Chantler, A. T. Payne, J. D. Gillaspy, L. T. Hudson, L. F. Smale, A. Henins, J. A. Kimpton, and E. Takacs. X-ray measurements in helium-like atoms increased discrepancy between experiment and theoretical QED. *New Journal of Physics*, 16(12):123037, 2014. doi:10.1088/1367-2630/16/12/123037.

[138] S. W. Epp, R. Steinbrügge, S. Bernitt, J. K. Rudolph, C. Beilmann, H. Bekker, A. Müller, O. O. Versolato, H.-C. Wille, H. Yavaş, J. Ullrich, and J. R. Crespo López-Urrutia. Single-photon excitation of Kα in heliumlike Kr^{34+}: Results supporting quantum electrodynamics predictions. *Physical Review A*, 92(2): 020502, 2015. doi:10.1103/PhysRevA.92.020502.

[139] P. Beiersdorfer and G. V. Brown. Experimental study of the x-ray transitions in the heliumlike isoelectronic sequence: Updated results. *Physical Review A*, 91(3): 032514, 2015. doi:10.1103/PhysRevA.91.032514.

[140] J. Machado, C. I. Szabo, J. P. Santos, P. Amaro, M. Guerra, A. Gumberidze, G. Bian, J. M. Isac, and P. Indelicato. High-precision measurements of $n = 2 \rightarrow$

$n = 1$ transition energies and level widths in He- and Be-like argon ions. *Physical Review A*, 97(3):032517, 2018. doi:10.1103/PhysRevA.97.032517.

[141] Ph. Pfäfflein. *Determination of the Kα transition energies in helium-like uranium*. PhD thesis, Friedrich-Schiller-Universität Jena, 2025. [Upload forthcoming 2026].

[142] G. Weber. *Untersuchung zur Anisotropie und linearen Polarisation radiativer Prozesse in energiereichen Ion-Atom-Stößen*. PhD thesis, Ruperto-Carola-University of Heidelberg, 2010. URL `https://archiv.ub.uni-heidelberg.de/volltextserver/10759/`.

[143] J. Eichler and Th. Stöhlker. Radiative electron capture in relativistic ion–atom collisions and the photoelectric effect in hydrogen-like high-Z systems. *Physics Reports*, 439(1):1–99, 2007. doi:10.1016/j.physrep.2006.11.003.

[144] Th. Stöhlker. *Atomphysik sehr starker Zentralfelder: Die Röntgenstrahlung der schwersten Ein-und Zwei-Elektronensysteme*. Habilitationsschrift, Johann Wolfgang Goethe-Universität Frankfurt, Germany, 1998.

[145] S. Chu, J. D. Graybeal, G. S. Hurst, and J. O. Stoner. 'spectroscopy'. encyclopedia britannica [online], 2025. URL `https://www.britannica.com/science/spectroscopy`. [Accessed on: 05.02.2025].

[146] A. Einstein. Über einen die Erzeugung und Verwandlung des Lichtes betreffenden heuristischen Gesichtspunkt. *Annalen der Physik*, 322(6):132–148, 1905. doi:10.1002/andp.19053220607.

[147] M. J. Berger, J. H. Hubbell, S. M. Seltzer, J. Chang, J. S. Coursey, R. Sukumar, D. S. Zucker, and K. Olsen. XCOM: Photon cross sections database, NIST standard reference database 8 (XGAM) [online], 2010. URL `https://www.nist.gov/pml/xcom-photon-cross-sections-database`. [Accessed on: 21.04.2024].

[148] W. H. Bragg and W. L. Bragg. The reflection of X-rays by crystals. *Proceedings of the Royal Society of London. Series A, Containing Papers of a Mathematical and Physical Character*, 88(605):428–438, 1913. doi:10.1098/rspa.1913.0040.

[149] G. W. Fraser, A. F. Abbey, A. Holland, K. McCarthy, A. Owens, and A. Wells. The x-ray energy response of silicon part A. Theory. *Nuclear Instruments and*

Methods in Physics Research Section A: Accelerators, Spectrometers, Detectors and Associated Equipment, 350(1):368–378, 1994. doi:10.1016/0168-9002(94)91185-1.

[150] M. O. Herdrich. *Photonen- und Elektronen-Emission von relativistischen Schwerionen beim Durchgang durch Materie.* Master's thesis, Friedrich-Schiller-Universität Jena, 2016. URL `https://www.hi-jena.de/fileadmin/content/publications/mherdrich_msc.pdf`.

[151] A. Fleischmann, C. Enss, and G. M. Seidel. Metallic magnetic calorimeters. In C. Enss, editor, *Cryogenic Particle Detection*, pages 151–216. Springer-Verlag Berlin Heidelberg, 2005. ISBN 978-3-540-20113-7. doi:10.1007/10933596_4.

[152] S. M. Girvin and K. Yang. *Modern condensed matter physics.* Cambridge University Press, 2019. ISBN 9781107137394. doi:10.1017/9781316480649.

[153] P. Debye. Zur Theorie der spezifischen Wärmen. *Annalen der Physik*, 344(14): 789–839, 1912. doi:10.1002/andp.19123441404.

[154] D. McCammon, W. Cui, M. Juda, P. Plucinsky, J. Zhang, R. L. Kelley, S. S. Holt, G. M. Madejski, S. H. Moseley, and A. E. Szymkowiak. Cryogenic microcalorimeters for high resolution spectroscopy: current status and future prospects. *Nuclear Physics A*, 527:821–824, 1991. doi:10.1016/0375-9474(91)90238-2.

[155] L. Lesyna, D. Di Marzio, S. Gottesman, and M. Kesselman. Advanced x-ray detectors for the analysis of materials. *Journal of Low Temperature Physics*, 93 (3):779–784, 1993. doi:10.1007/BF00693512.

[156] E. Silver, M. LeGros, N. Madden, J. Beeman, and E. Haller. High-resolution, broad-band microcalorimeters for x-ray microanalysis. *X-Ray Spectrometry*, 25(3):115–122, 1996. doi:10.1002/(SICI)1097-4539(199605)25:3<115::AID-XRS140>3.0.CO;2-S.

[157] D. A. Wollman, K. D. Irwin, G. C. Hilton, L. L. Dulcie, D. E. Newbury, and J. M. Martinis. High-resolution, energy-dispersive microcalorimeter spectrometer for x-ray microanalysis. *Journal of Microscopy*, 188(3):196–223, 1997. doi:10.1046/j.1365-2818.1997.2670824.x. [Upload (online) in: 2003].

[158] S. R. Bandler, J. S. Adams, J. A. Chervenak, A. M. Datesman, M. E. Eckart, F. M. Finkbeiner, R. L. Kelley, C. A. Kilbourne, G. Betancourt-Martinez, A. R. Miniussi,

F. S. Porter, J. E. Sadleir, K. Sakai, S. J. Smith, T. R. Stevenson, N. A. Wakeham, E. J. Wassell, W. Yoon, D. Becker, D. Bennett, W. B. Doriese, J. W. Fowler, J. D. Gard, G. C. Hilton, B. Mates, K. M. Morgan, C. D. Reintsema, D. Swetz, J. N. Ullom, S. Chaudhuri, K. D. Irwin, S.-J. Lee, and A. Vikhlinin. Development of x-ray microcalorimeter imaging spectrometers for the X-ray Surveyor mission concept. In J.-W. A. den Herder, T. Takahashi, and M. Bautz, editors, *Space Telescopes and Instrumentation 2016: Ultraviolet to Gamma Ray*, volume 9905, pages 192–203. SPIE, 2016. doi:10.1117/12.2232156.

[159] F. Toschi, B. Maier, G. Heine, T. Ferber, S. Kempf, M. Klute, and B. von Krosigk. Optimum filter-based analysis for the characterization of a high-resolution magnetic microcalorimeter. *Physical Review D*, 109(4):043035, 2024. doi:10.1103/PhysRevD.109.043035.

[160] G. Angloher, S. Banik, G. Benato, A. Bento, A. Bertolini, R. Breier, C. Bucci, J. Burkhart, L. Canonica, A. D'Addabbo, S. Di Lorenzo, L. Einfalt, A. Erb, F. v. Feilitzsch, N. Ferreiro Iachellini, S. Fichtinger, D. Fuchs, A. Fuss, A. Garai, V. M. Ghete, S. Gerster, P. Gorla, P. V. Guillaumon, S. Gupta, D. Hauff, M. Ješkovský, J. Jochum, M. Kaznacheeva, A. Kinast, H. Kluck, H. Kraus, A. Langenkämper, M. Mancuso, L. Marini, L. Meyer, V. Mokina, A. Nilima, M. Olmi, T. Ortmann, C. Pagliarone, L. Pattavina, F. Petricca, W. Potzel, P. Povinec, F. Pröbst, F. Pucci, F. Reindl, J. Rothe, K. Schäffner, J. Schieck, D. Schmiedmayer, S. Schönert, C. Schwertner, M. Stahlberg, L. Stodolsky, C. Strandhagen, R. Strauss, I. Usherov, F. Wagner, M. Willers, V. Zema, and CRESST Collaboration. Results on sub-GeV dark matter from a 10 eV threshold CRESST-III silicon detector. *Physical Review D*, 107(12):122003, 2023. doi:10.1103/PhysRevD.107.122003.

[161] D. A. Müller. *Mitigation of signal digitisation artefacts on the spectral performance of metallic magnetic calorimeters.* Master's thesis, Friedrich-Schiller-Universität Jena, 2024. [Upload forthcoming 2025].

[162] H.-D. Betz, G. Hortig, E. Leischner, Ch. Schmelzer, B. Stadler, and J. Weihrauch. The average charge of stripped heavy ions. *Physics Letters*, 22(5):643–644, 1966. doi:10.1016/0031-9163(66)90690-1.

[163] W. H. Barkas. *Nuclear Research Emulsions: Particle behavior and emulsion*

applications, edited by D.A. Evans, volume 15. Academic Press, 1963. ISBN 978-0-12-078302-1.

[164] J. L. Gervasoni and S. Cruz-Jiménez. Bohr's adiabatic criterion and effective charge of heavy ions. *Radiation Physics and Chemistry*, 48(4):433–436, 1996. doi:10.1016/0969-806X(96)00001-1.

[165] J. P. Rozet, C. Stéphan, and D. Vernhet. ETACHA: A program for calculating charge states at GANIL energies. *Nuclear Instruments and Methods in Physics Research Section B: Beam Interactions with Materials and Atoms*, 107(1-4):67–70, 1996. doi:10.1016/0168-583X(95)00800-4.

[166] C. Scheidenberger, Th. Stöhlker, W. E. Meyerhof, H. Geissel, P. H. Mokler, and B. Blank. Charge states of relativistic heavy ions in matter. *Nuclear Instruments and Methods in Physics Research Section B: Beam Interactions with Materials and Atoms*, 142(4):441–462, 1998. doi:10.1016/S0168-583X(98)00244-4.

[167] O. B. Tarasov and D. Bazin. LISE++: Design your own spectrometer. *Nuclear Physics A*, 746:411–414, 2004. doi:10.1016/j.nuclphysa.2004.09.063.

[168] M. W. Krasny, R. Alemany-Fernández, P. S. Antsiferov, A. Apyan, H. Bartosik, E. G. Bessonov, N. Biancacci, J. Bieron, D. Budker, K. Cassou, F. Castelli, I. Chaikovska, R. Chehab, C. Curatolo, P. Czodrowski, K. Dupraz, K. Dzierzega, B. Goddard, S. Hirlaender, J. M. Jowett, R. Kersevan, M. Kowalska, F. Kroeger, M. Lamont, D. Manglunki, A. Martens, A. V. Petrenko, V. Petrillo, W. Placzek, S. Pustelny, M. Schaumann, L. Serafini, V. P. Shevelko, Th. Stöhlker, G. Weber, Y. K. Wu, C. Yin Vallgren, F. Zimmermann, M. S. Zolotorev, and F. Zomer. The CERN Gamma Factory Initiative: An ultra-high intensity Gamma source. In T. Satogata, V. R. W. Schaa, S. Koscielniak, and J. Thomson, editors, *Proceedings of the 9th International Particle Accelerator Conference (IPAC18)*, number 9 in International Particle Accelerator Conference, pages 1780–1783. JACoW Publishing, 2018. ISBN 978-3-95450-184-7. doi:10.18429/JACoW-IPAC2018-WEYGBD3.

[169] W. Placzek, A. Abramov, S. E. Alden, R. Alemany Fernandez, P. S. Antsiferov, A. Apyan, H. Bartosik, E. G. Bessonov, N. Biancacci, J. Bieron, A. Bogacz, A. Bosco, R. Bruce, D. Budker, K. Cassou, F. Castelli, I. Chaikovska, C. Curatolo, P. Czodrowski, A. Derevianko, K. Dupraz, Y. Dutheil, K. Dzierzega, V. Fedosseev,

N. Fuster Martinez, S. M. Gibson, B. Goddard, A. Gorzawski, S. Hirlander, J. Jowett, R. Kersevan, M. Kowalska, M. W. Krasny, F. Kroeger, M. Lamont, T. Lefevre, D. Manglunki, B. Marsh, A. Martens, J. Molson, D. Nutarelli, L. J. Nevay, A. Petrenko, V. Petrillo, S. Radaelli, S. Pustelny, S. Rochester, M. Sapinski, M. Schaumann, L. Serafini, V. P. Shevelko, Th. Stöhlker, A. Surzhikov, I. Tolstikhina, F. Velotti, G. Weber, Y. K. Wu, C. Yin-Vallgren, M. Zanetti, F. Zimmermann, M. S. Zolotorev, and F. Zomer. Gamma Factory at CERN – novel research tools made of light. *Acta Physica Polonica B*, 50(6):1191, 2019. doi:10.5506/APhysPolB.50.1191.

[170] F. M. Kröger, G. Weber, S. Hirlaender, R. Alemany-Fernandez, M. W. Krasny, Th. Stöhlker, I. Y. Tolstikhina, and V. P. Shevelko. Charge-state distributions of highly charged lead ions at relativistic collision energies. *Annalen der Physik*, 534 (3):2100245, 2022. doi:10.1002/andp.202100245.

[171] M. Schaumann, R. Alemany-Fernandez, H. Bartosik, T. Bohl, R. Bruce, G. H. Hemelsoet, S. Hirlaender, J. M. Jowett, V. Kain, M. W. Krasny, J. Molson, G. Papotti, M. Solfaroli Camillocci, H. Timko, and J. Wenninger. First partially stripped ions in the LHC ($^{208}Pb^{81+}$). *Journal of Physics: Conference Series*, 1350 (1):012071, 2019. doi:10.1088/1742-6596/1350/1/012071.

[172] G. I. Budker. An effective method of damping particle oscillations in proton and antiproton storage rings. *Soviet Atomic Energy*, 22(5):438–440, 1967. doi:10.1007/BF01175204.

[173] H. Poth. Electron cooling: Theory, experiment, application. *Physics Reports*, 196 (3–4):135–297, 1990. doi:10.1016/0370-1573(90)90040-9.

[174] M. Steck, K. Beckert, F. Bosch, H. Eickhoff, B. Franzke, O. Klepper, F. Nolden, H. Reich, B. Schlitt, P. Spädtke, and T. Winkler. Cooled heavy ion beams at the ESR. *Nuclear Physics A*, 626(1):495–498, 1997. doi:10.1016/S0375-9474(97)00574-5.

[175] T. Winkler, K. Beckert, F. Bosch, H. Eickhoff, B. Franzke, F. Nolden, H. Reich, B. Schlitt, and M. Steck. Electron cooling of highly charged ions in the ESR. *Nuclear Physics A*, 626(1):485–489, 1997. doi:10.1016/S0375-9474(97)00572-1.

[176] G. Kilgus, D. Habs, D. Schwalm, A. Wolf, N. R. Badnell, and A. Müller. High-resolution measurement of dielectronic recombination of lithiumlike Cu^{26+}. *Physical Review A*, 46(9):5730–5740, 1992. doi:10.1103/PhysRevA.46.5730.

[177] M. Lestinsky, E. B. Menz, and M. Grieser. Beamcalc web application [online]. URL `http://web-docs.gsi.de/~lestinsk/beamcalc/`. [Accessed on: 2024].

[178] H. Nussbaumer and P. J. Storey. Dielectronic recombination at low temperatures. *Astronomy and Astrophysics*, 126(1):75–79, September 1983. ISSN 0004-6361. URL `https://ui.adsabs.harvard.edu/abs/1983A&A...126...75N`. [Provided by the SAO/NASA Astrophysics Data System].

[179] A. Ichihara, T. Shirai, and J. Eichler. Radiative electron capture in relativistic atomic collisions. *Physical Review A*, 49(3):1875–1884, 1994. doi:10.1103/PhysRevA.49.1875.

[180] H. A. Kramers. XCIII. On the theory of x-ray absorption and of the continuous x-ray spectrum. *The London, Edinburgh, and Dublin Philosophical Magazine and Journal of Science*, 46(275):836–871, 1923. doi:10.1080/14786442308565244.

[181] Th. Stöhlker, C. Kozhuharov, P. H. Mokler, A. Warczak, F. Bosch, H. Geissel, R. Moshammer, C. Scheidenberger, J. Eichler, A. Ichihara, T. Shirai, Z. Stachura, and P. Rymuza. Radiative electron capture studied in relativistic heavy-ion–atom collisions. *Physical Review A*, 51(3):2098–2111, 1995. doi:10.1103/PhysRevA.51.2098.

[182] W. Gordon. Zur Berechnung der Matrizen beim Wasserstoffatom. *Annalen der Physik*, 394(8):1031–1056, 1929. doi:10.1002/andp.19293940807.

[183] J. R. Oppenheimer. On the quantum theory of the capture of electrons. *Physical Review*, 31(3):349–356, 1928. doi:10.1103/PhysRev.31.349.

[184] E. C. G. Stueckelberg and P. M. Morse. Computation of the effective cross section for the recombination of electrons with hydrogen ions. *Physical Review*, 36(1): 16–23, 1930. doi:10.1103/PhysRev.36.16.

[185] W. Wessel. Über den Wirkungsquerschnitt freier Atomkerne. *Annalen der Physik*, 397(5):611–624, 1930. doi:10.1002/andp.19303970506.

[186] M. Stobbe. Zur Quantenmechanik photoelektrischer Prozesse. *Annalen der Physik*, 399(6):661–715, 1930. doi:10.1002/andp.19303990604.

[187] M. Pajek and R. Schuch. Radiative recombination of bare ions with low-energy free electrons. *Physical Review A*, 45(11):7894–7905, 1992. doi:10.1103/PhysRevA.45.7894.

[188] J. Eichler, A. Ichihara, and T. Shirai. Photon angular distributions from radiative electron capture in relativistic atomic collisions. *Physical Review A*, 51(4):3027–3035, 1995. doi:10.1103/PhysRevA.51.3027.

[189] F. Bosch. First experiments at the Darmstadt storage-cooler ring ESR. *Nuclear Instruments and Methods in Physics Research Section A: Accelerators, Spectrometers, Detectors and Associated Equipment*, 314(2):269–276, 1992. doi:10.1016/0168-9002(92)90970-F.

[190] M. Bell and J. S. Bell. Capture of cooling electrons by cool protons. *Particle Accelerators*, 12(CERN-TH-3054):49–52, 1982. URL `https://cds.cern.ch/record/128745`.

[191] A. Burgess. Tables of hydrogenic photoionization cross-sections and recombination coefficients. *Memoirs of the Royal Astronomical Society, Vol. 69, p. 1*, 69: 1, 1965. URL `https://ui.adsabs.harvard.edu/abs/1965MmRAS..69....1B/abstract`.

[192] J. R. Grover. Shell-model calculations of the lowest-energy nuclear excited states of very high angular momentum. *Physical Review*, 157(4):832–847, 1967. doi:10.1103/PhysRev.157.832.

[193] F. M. Kröger, G. Weber, S. Allgeier, Z. Andelkovic, S. Bernitt, A. Borovik Jr., L. Duval, A. Fleischmann, O. Forstner, M. Friedrich, J. Glorius, A. Gumberidze, C. Hahn, F. Herfurth, D. Hengstler, M. O. Herdrich, P.-M. Hillenbrand, A. Kalinin, M. Kiffer, M. Kubullek, P. Kuntz, M. Lestinsky, B. Löher, E. B. Menz, T. Over, N. Petridis, P. Pfäfflein, S. Ringleb, R. S. Sidhu, U. Spillmann, S. Trotsenko, A. Warczak, B. Zhu, C. Enss, and Th. Stöhlker. Towards an intrinsic Doppler correction for x-ray spectroscopy of stored ions at CRYRING@ESR. *Atoms*, 11 (2):22, 2023. doi:10.3390/atoms11020022.

[194] O. Rest, D. Winzen, V. Hannen, and C. Weinheimer. Absolute calibration of a ppm-precise hv divider for the electron cooler of the ion storage ring cryring@esr. In B. Németh, editor, *Proceedings of the 21st International Symposium on High Voltage Engineering*, pages 1500–1512. Springer International Publishing, Cham, 2020. ISBN 978-3-030-31680-8. doi:doi.org/10.1007/978-3-030-31680-8_142.

[195] B. Franzke, K. Beckert, H. Eickhoff, F. Nolden, H. Reich, U. Schaaf, B. Schlitt, A. Schwinn, M. Steck, and Th. Winkler. Schottky mass spectrometry at the experimental storage ring esr. *Physica Scripta*, 1995(T59):176, 1995. doi:10.1088/0031-8949/1995/T59/021.

[196] T. Kühl. Nuclear properties by laser spectroscopy in beams and rings. *Physica Scripta*, 1988(T22):144, 1988. doi:10.1088/0031-8949/1988/T22/022.

[197] S. Schmidt, Ch. Geppert, and Z. Andelkovic for the LIBELLE & SpecTrap Collaborations. Laser spectroscopy methods for probing highly charged ions at GSI. *Hyperfine Interactions*, 227(1):29–43, 2014. doi:10.1007/s10751-014-1048-1.

[198] R. W. Schmieder. Doppler-tuned x-ray spectrometer. *Review of Scientific Instruments*, 45(5):687–701, 1974. doi:10.1063/1.1686714.

[199] L. Fonda, G. C. Ghirardi, and A. Rimini. Decay theory of unstable quantum systems. *Reports on Progress in Physics*, 41(4):587–631, 1978. doi:10.1088/0034-4885/41/4/003.

[200] V. N. Faddeeva and N. M. Terent'ev. *Table of values of the function w(z) = e^{-z^2} (1+2i/$\sqrt{\pi}$ $\int_0^z e^{t^2} dt$) for complex argument, by V. N. Faddeeva and N. M. Terent'ev. edited by V. A. Fok. Translated from the Russian by D. G. Fry.* Pergamon Press, 1961. [Original: Gosudarstv. Izdat. Tehn.-Teor. Lit., Moscow, 268 pp., 1954.].

[201] P. Bell, C. Bousseau, J. Bowhay, M. Brett, R. Gommers, R. Goswami, M. Haberland, P. Nobel, T. Reddy, D. Schmitz, D. Schult, S. Shambaugh, E. A. M. Tuay, and W. Weckesser. scipy.special.voigt_profile, SciPy documentation [online]. URL `https://docs.scipy.org/doc/scipy/reference/generated/scipy.special.voigt_profile.html`. [Accessed on: 15.04.2025].

[202] E. Wilson and B. J. Holzer. Beam dynamics. In S. Myers and H. Schopper, editors, *Particle physics reference library: Accelerators and colliders*, volume 3, pages 15–50. Springer International Publishing, 2020. ISBN 978-3-030-34245-6. doi:10.1007/978-3-030-34245-6_2.

[203] Th. Stöhlker, H. Reich, K. Beckert, F. Bosch, A. Gallus, H. Eickhoff, B. Franzke, T. Kandler, O. Klepper, C. Kozhuharov, G. Menzel, P.H. Mokler, F. Nolden, H. T. Prinz, P. Spädtke, M. Steck, T. Winkler, R. W. Dunford, P. Rymuza, T. Ludziejewski, Z. Stachura, P. Swiat, and A. Warczak. First experiment with decelerated bare uranium ions conducted at the ESR storage ring. *Hyperfine Interactions*, 108(1):29–38, 1997. doi:10.1023/A:1012669503724.

[204] M. Lestinsky, V. Andrianov, B. Aurand, V. Bagnoud, D. Bernhardt, H. Beyer, S. Bishop, K. Blaum, A. Bleile, A. Borovik Jr., F. Bosch, C. J. Bostock, C. Brandau, A. Bräuning-Demian, I. Bray, T. Davinson, B. Ebinger, A. Echler, P. Egelhof, A. Ehresmann, M. Engström, C. Enss, N. Ferreira, D. Fischer, A. Fleischmann, E. Förster, S. Fritzsche, R. Geithner, S. Geyer, J. Glorius, K. Göbel, O. Gorda, J. Goullon, P. Grabitz, R. Grisenti, A. Gumberidze, S. Hagmann, M. Heil, A. Heinz, F. Herfurth, R. Heß, P.-M. Hillenbrand, R. Hubele, P. Indelicato, A. Källberg, O. Kester, O. Kiselev, A. Knie, C. Kozhuharov, S. Kraft-Bermuth, T. Kühl, G. Lane, Yu. A. Litvinov, D. Liesen, X. W. Ma, R. Märtin, R. Moshammer, A. Müller, S. Namba, P. Neumeyer, T. Nilsson, W. Nörtershäuser, G. Paulus, N. Petridis, M. Reed, R. Reifarth, P. Reiß, J. Rothhardt, R. Sanchez, M. S. Sanjari, S. Schippers, H.T. Schmidt, D. Schneider, P. Scholz, R. Schuch, M. Schulz, V. Shabaev, A. Simonsson, J. Sjöholm, Ö. Skeppstedt, K. Sonnabend, U. Spillmann, K. Stiebing, M. Steck, Th. Stöhlker, A. Surzhykov, S. Torilov, E. Träbert, M. Trassinelli, S. Trotsenko, X. L. Tu, I. Uschmann, P. M. Walker, G. Weber, D. F. A. Winters, P. J. Woods, H. Y. Zhao, and Y. H. Zhang. Physics book: CRYRING@ESR. *The European Physical Journal Special Topics*, 225(5):797–882, 2016. doi:10.1140/epjst/e2016-02643-6.

[205] B. Franzke. The heavy ion storage and cooler ring project ESR at GSI. *Nuclear Instruments and Methods in Physics Research Section B: Beam Interactions with Materials and Atoms*, 24-25:18–25, 1987. doi:10.1016/0168-583X(87)90583-0.

[206] J. W. Xia, W. L. Zhan, B. W. Wei, Y. J. Yuan, M. T. Song, W. Z. Zhang, X. D.

Yang, P. Yuan, D. Q. Gao, H. W. Zhao, X. T. Yang, G. Q. Xiao, K. T. Man, J. R. Dang, X. H. Cai, Y. F. Wang, J. Y. Tang, W. M. Qiao, Y. N. Rao, Y. He, L. Z. Mao, and Z. Z. Zhou. The heavy ion cooler-storage-ring project (HIRFL-CSR) at Lanzhou. *Nuclear Instruments and Methods in Physics Research Section A: Accelerators, Spectrometers, Detectors and Associated Equipment*, 488(1):11–25, 2002. doi:10.1016/S0168-9002(02)00475-8.

[207] A. Gumberidze, Th. Stöhlker, D. Banaś, K. Beckert, P. Beller, H. F. Beyer, F. Bosch, X. Cai, S. Hagmann, C. Kozhuharov, D. Liesen, F. Nolden, X. Ma, P. H. Mokler, A. Oršić-Muthig, M. Steck, D. Sierpowski, S. Tashenov, A. Warczak, and Y. Zou. Electron-electron interaction in strong electromagnetic fields: The two-electron contribution to the ground-state energy in He-like uranium. *Physical Review Letters*, 92(20):203004, 2004. doi:10.1103/PhysRevLett.92.203004.

[208] A. Gumberidze, Th. Stöhlker, D. Banaś, K. Beckert, P. Beller, H. F. Beyer, F. Bosch, S. Hagmann, C. Kozhuharov, D. Liesen, F. Nolden, X. Ma, P. H. Mokler, M. Steck, D. Sierpowski, and S. Tashenov. Quantum electrodynamics in strong electric fields: The ground-state lamb shift in hydrogenlike uranium. *Physical Review Letters*, 94(22):223001, 2005. doi:10.1103/PhysRevLett.94.223001.

[209] R. Reuschl. *Untersuchungen zur Lamb-Verschiebung in schweren Ein- und Zwei-Elektronen-Systemen*. PhD thesis, Johann Wolfgang Goethe-Universität Frankfurt am Main, 2008. URL `https://web-docs.gsi.de/~stoe_exp/theses/theses.php`.

[210] R. Reuschl, A. Gumberidze, Th. Stöhlker, C. Kozhuharov, J. Rzadkiewicz, U. Spillmann, S. Tashenov, S. Fritzsche, and A. Surzhykov. The Balmer spectrum of H-like uranium produced by radiative recombination at low velocities. *Radiation Physics and Chemistry*, 75(11):1740–1743, 2006. doi:10.1016/j.radphyschem.2006.05.006.

[211] R. Reuschl, A. Gumberidze, C. Kozhuharov, U. Spillmann, S. Tashenov, Th. Stöhlker, and J. Eichler. State-selective x-ray studies of radiative recombination into bare and H-like uranium at threshold energies. *Physical Review A*, 77(3): 032701, 2008. doi:10.1103/PhysRevA.77.032701.

[212] A. Gumberidze, Th. Stöhlker, D. Banaś, K. Beckert, P. Beller, H. F. Beyer, F. Bosch, X. Cai, S. Hagmann, C. Kozhuharov, D. Liesen, F. Nolden, X. Ma,

P. H. Mokler, M. Steck, D. Sierpowski, S. Tashenov, A. Warczak, and Y. Zou. Precision tests of QED in strong fields: Experiments on hydrogen- and helium-like uranium. *Journal of Physics: Conference Series*, 58:87–92, 2007. doi:10.1088/1742-6596/58/1/013.

[213] H. F. Beyer. Characterization of transmission-type curved-crystal X-ray optics for fast ion-beam spectroscopy. *Nuclear Instruments and Methods in Physics Research Section A: Accelerators, Spectrometers, Detectors and Associated Equipment*, 400 (1):137–148, 1997. doi:10.1016/S0168-9002(97)01007-3.

[214] T. Gassner and H. F. Beyer. Spatial characterization of the internal gas target at the ESR for the FOCAL experiment. *Physica Scripta*, 2015(T166):014052, 2015. doi:10.1088/0031-8949/2015/T166/014052.

[215] T. Gaßner. *High precision x-ray spectroscopy of highly charged heavy ions*. PhD thesis, Friedrich-Schiller-Universität Jena, 2016. URL `https://www.db-thueringen.de/receive/dbt_mods_00031352`. [Published online in 2017].

[216] T. Gassner, A. Gumberidze, M. Trassinelli, R. Heß, U. Spillmann, D. Banaś, K.-H. Blumenhagen, F. Bosch, C. Brandau, W. Chen, Chr. Dimopoulou, E. Förster, R. E. Grisenti, S. Hagmann, P.-M. Hillenbrand, P. Indelicato, P. Jagodzinski, T. Kämpfer, M. Lestinsky, D. Liesen, Yu. A. Litvinov, R. Loetzsch, B. Manil, R. Märtin, F. Nolden, N. Petridis, M. S. Sanjari, K. S. Schulze, M. Schwemlein, A. Simionovici, M. Steck, Th. Stöhlker, C. I. Szabo, S. Trotsenko, I. Uschmann, G. Weber, O. Wehrhan, N. Winckler, D. F. A. Winters, N. Winters, E. Ziegler, and H. F. Beyer. High-resolution wavelength-dispersive spectroscopy of K-shell transitions in hydrogen-like gold. *X-Ray Spectrometry*, 49(1):204–208, 2020. doi:10.1002/xrs.3098. [Published online in 2019].

[217] H. F. Beyer, Th. Stöhlker, D. Banaś, D. Liesen, D. Protić, K. Beckert, P. Beller, J. Bojowald, F. Bosch, E. Förster, B. Franzke, A. Gumberidze, S. Hagmann, J. Hoszowska, P. Indelicato, O. Klepper, H.-J. Kluge, St. König, Chr. Kozhuharov, X. Ma, B. Manil, I. Mohos, A. Oršić-Muthig, F. Nolden, U. Popp, A. Simionovici, D. Sierpowski, U. Spillmann, Z. Stachura, M. Steck, S. Tachenov, M. Trassinelli, A. Warczak, O. Wehrhan, and E. Ziegler. FOCAL: X-ray optics for accurate spectroscopy. *Spectrochimica Acta Part B: Atomic Spectroscopy*, 59(10):1535–1542, 2004. doi:10.1016/j.sab.2004.03.023.

[218] P. Spiller, R. Balss, P. Bartolome, J. Blaurock, U. Blell, O. Boine-Frankenheim, L. Bozyk, M. Chorowski, T. Eisel, M. Frey, T. Giacomini, F. Kaether, H. Khodzhibagiyan, S. Klammes, H. Klingbeil, H.G. Koenig, V. Kornilov, P. Kowina, D. Lens, J.P. Meier, D. Ondreka, I. Petzenhauser, V. Plyusnin, I. Pongrac, N. Pyka, V. Raginel, P. Rottlaender, C. Roux, J. Schmidt, M. Schwickert, K. Sugita, A. Szwangruber, P. Szwangruber, R. Trockel, A. Waldt, H. Welker, S. Wilfert, T. Winkler, and D. Winters. The FAIR heavy ion synchrotron SIS100. *Journal of Instrumentation*, 15(12):T12013–T12013, 2020. doi:10.1088/1748-0221/15/12/T12013.

[219] A. Adonin and R. Hollinger. Progress on MEVVA source VARIS at GSI. *Review of Scientific Instruments*, 89(5):052304, 2018. doi:10.1063/1.5017137.

[220] Ph. Pfäfflein, S. Allgeier, S. Bernitt, A. Fleischmann, M. Friedrich, Ch. Hahn, D. Hengstler, M. O. Herdrich, A. Kalinin, F. M. Kröger, P. Kuntz, M. Lestinsky, B. Löher, E. B. Menz, T. Over, U. Spillmann, G. Weber, B. Zhu, Ch. Enss, and Th. Stöhlker. Integration of maXs-type microcalorimeter detectors for high-resolution x-ray spectroscopy into the experimental environment at the CRYRING@ESR electron cooler. *Physica Scripta*, 97(11):114005, 2022. doi:10.1088/1402-4896/ac93be.

[221] K. Abrahamsson, G. Andler, L. Bagge, E. Beebe, P. Carlé, H. Danared, S. Egnell, K. Ehrnstén, M. Engström, C. J. Herrlander, J. Hilke, J. Jeansson, A. Källberg, S. Leontein, L. Liljeby, A. Nilsson, A. Paal, K.-G. Rensfelt, U. Rosengård, A. Simonsson, A. Soltan, J. Starker, M. af Ugglas, and A. Filevich. CRYRING — a synchrotron, cooler and storage ring. *Nuclear Instruments and Methods in Physics Research Section B: Beam Interactions with Materials and Atoms*, 79(1):269–272, 1993. doi:10.1016/0168-583X(93)95341-2.

[222] Manne Siegbahn Laboratory webpage [online], 2014. URL `https://www.msi.se/`. [Accessed on: 29.04.2025].

[223] H.-J. Kluge, T. Beier, K. Blaum, L. Dahl, S. Eliseev, F. Herfurth, B. Hofmann, O. Kester, S. Koszudowski, C. Kozhuharov, G. Maero, W. Nörtershäuser, J. Pfister, W. Quint, U. Ratzinger, A. Schempp, R. Schuch, Th. Stöhlker, R. C. Thompson, M. Vogel, G. Vorobjev, D. F. A. Winters, and G. Werth. Chapter 7 HITRAP: A facility at GSI for highly charged ions. In S. Salomonson and E. Lindroth, editors,

Advances in quantum chemistry, volume 53 of *Current trends in atomic physics*, pages 83–98. Academic Press, 2008. ISBN 978-0-12-373925-4. doi:10.1016/S0065-3276(07)53007-8.

[224] F. Herfurth, Z. Andelkovic, W. Barth, W. Chen, L. A. Dahl, S. Fedotova, P. Gerhard, M. Kaiser, O. K. Kester, H.-J. Kluge, N. Kotovskiy, M. Maier, B. Maaß, D. Neidherr, W. Quint, U. Ratzinger, A. Reiter, A. Schempp, Th. Stöhlker, H. Vormann, G. Vorobjev, S. Yaramyshev, and collaboration for the HITRAP. The HITRAP facility for slow highly charged ions. *Physica Scripta*, 2015(T166): 014065, 2015. doi:10.1088/0031-8949/2015/T166/014065.

[225] Th. Stöhlker, V. Bagnoud, K. Blaum, A. Blazevic, A. Bräuning-Demian, M. Durante, F. Herfurth, M. Lestinsky, Y. Litvinov, S. Neff, R. Pleskac, R. Schuch, S. Schippers, D. Severin, A. Tauschwitz, C. Trautmann, D. Varentsov, and E. Widmann, on behalf of the APPA Collaborations. APPA at FAIR: From fundamental to applied research. *Nuclear Instruments and Methods in Physics Research Section B: Beam Interactions with Materials and Atoms*, 365:680–685, 2015. doi:10.1016/j.nimb.2015.07.077.

[226] F. M. Kröger, G. Weber, O. Forstner, A. Gumberidze, M. O. Herdrich, M. Lestinsky, A. Kalinin, T. Köhler, E. Menz, P. Pfäfflein, U. Spillmann, and Th. Stöhlker. New setup for x-ray spectroscopy at the CRYRING@ESR electron cooler. In *Helmholtz Institute Jena annual report 2019*, page 45. Helmholtz Institute Jena and GSI Helmholtzzentrum für Schwerionenforschung GmbH, 2020. doi:10.15120/GSI-2020-00954.

[227] SAES. NEXTorr® D1000-StarCell®, pumps manual. [Downloaded in 2024].

[228] B. Zhu, A. Gumberidze, T. Over, G. Weber, Z. Andelkovic, A. Bräuning-Demian, R. J. Chen, D. Dmytriiev, O. Forstner, C. Hahn, F. Herfurth, M. O. Herdrich, P.-M. Hillenbrand, A. Kalinin, F. M. Kröger, M. Lestinsky, Yu. A. Litvinov, E. B. Menz, W. Middents, T. Morgenroth, N. Petridis, Ph. Pfäfflein, M. S. Sanjari, R. S. Sidhu, U. Spillmann, R. Schuch, S. Schippers, S. Trotsenko, L. Varga, G. Vorobyev, and Th. Stöhlker. X-ray emission associated with radiative recombination for Pb^{82+} ions at threshold energies. *Physical Review A*, 105(5):052804, 2022. doi:10.1103/PhysRevA.105.052804.

[229] ASTM International. Escape Peak, NIST OSAC Lexicon [online], 2024. URL https://www.nist.gov/glossary-term/35216. [Accessed on: 06.02.2025].

[230] M. Lestinsky, E. B. Menz, H. Danared, C. Krantz, E. Lindroth, Z. Andelkovic, C. Brandau, A. Bräuning-Demian, S. Fedotova, W. Geithner, F. Herfurth, A. Kalinin, I. Kraus, U. Spillmann, G. Vorobyev, and Th. Stöhlker. First experiments with CRYRING@ESR. *Atoms*, 10(4), 2022. doi:10.3390/atoms10040141.

[231] E. B. Menz. *Preparation and realisation of first dielectronic recombination experiments at CRYRING@ESR.* PhD thesis, Friedrich-Schiller-Universität Jena, 2024. URL https://www.db-thueringen.de/receive/dbt_mods_00064496.

[232] D. Hengstler. *Development and characterization of two-dimensional metallic magnetic calorimeter arrays for the high-resolution x-ray spectroscopy.* PhD thesis, Ruperto-Carola-University of Heidelberg, Germany, 2017. URL http://www.ub.uni-heidelberg.de/archiv/23815.

[233] G. R. Stewart. Measurement of low-temperature specific heat. *Review of Scientific Instruments*, 54(1):1–11, 1983. doi:10.1063/1.1137207.

[234] W. Hahn, M. Loewenhaupt, and B. Frick. Crystal field excitations in dilute rare earth noble metal alloys. *Physica B: Condensed Matter*, 180-181:176–178, 1992. doi:10.1016/0921-4526(92)90698-R.

[235] R. C. Jaklevic, J. Lambe, A. H. Silver, and J. E. Mercereau. Quantum interference effects in Josephson tunneling. *Physical Review Letters*, 12:159–160, 1964. doi:10.1103/PhysRevLett.12.159.

[236] C. Enss, A. Fleischmann, K. Horst, J. Schönefeld, J. Sollner, J. S. Adams, Y. H. Huang, Y. H. Kim, and G. M. Seidel. Metallic magnetic calorimeters for particle detection. *Journal of Low Temperature Physics*, 121(3):137–176, 2000. doi:10.1023/A:1004863823166.

[237] A. Fleischmann. *Magnetische Mikrokalorimeter: Hochauflösende Röntgenspektroskopie mit energiedispersiven Detektoren.* PhD thesis, Ruperto-Carola-University of Heidelberg, Germany, 2003. URL http://www.ub.uni-heidelberg.de/archiv/12877.

[238] A. Burck. *Entwicklung großflächiger magnetischer Kalorimeter zur energieaufgelösten Detektion von Röntgenquanten und hochenergetischen Teilchen.* Diploma thesis, Ruperto-Carola-University of Heidelberg, Germany, 2004. URL `https://www.kip.uni-heidelberg.de/Veroeffentlichungen/details.php?id=1515#start`.

[239] A. Fleischmann n behalf of the SPARC Collaboration. maXs: Cryogenic microcalorimeter arrays for high resolution x-ray spectroscopy experiments at FAIR. Technical report, 2014. URL `https://edms.cern.ch/document/2059592/1`. [Published online in 2016].

[240] C. Pies, S. Schäfer, S. Heuser, S. Kempf, A. Pabinger, J.-P. Porst, P. Ranitsch, N. Foerster, D. Hengstler, A. Kampkötter, T. Wolf, L. Gastaldo, A. Fleischmann, and C. Enss. maXs: Microcalorimeter arrays for high-resolution x-ray spectroscopy at GSI/FAIR. *Journal of Low Temperature Physics*, 167(3):269–279, 2012. doi:10.1007/s10909-012-0557-z.

[241] M. O. Herdrich, A. Fleischmann, D. Hengstler, S. Allgeier, C. Enss, S. Trotsenko, T. Morgenroth, R. Schuch, G. Weber, and Th. Stöhlker. High-precision x-ray spectroscopy of Fe ions in an EBIT using a micro-calorimeter detector: First results. *X-Ray Spectrometry*, 49(1):184–187, 2020. doi:10.1002/xrs.3086.

[242] G. Weber, P. Pfäfflein, F. Kröger, M. O. Herdrich, A. Fleischmann, D. Hengstler, S. Allgeier, M. Friedrich, P. Kuntz, C. Enss, and Th. Stöhlker. Two novel maXs detector systems for the SPARC collaboration. In D. Seipt and A. Klenke, editors, *Helmholtz Institute Jena annual report 2020*, page 47. Helmholtz Institute Jena and GSI Helmholtzzentrum für Schwerionenforschung GmbH, 2021. doi:10.15120/GSI-2021-00839.

[243] S. Kempf, A. Fleischmann, L. Gastaldo, and C. Enss. Physics and applications of metallic magnetic calorimeters. *Journal of Low Temperature Physics*, 193(3): 365–379, 2018. doi:10.1007/s10909-018-1891-6.

[244] P. Pfäfflein, G. Weber, F. M. Kröger, M. O. Herdrich, T. Köhler, A. Fleischmann, D. Hengstler, and Th. Stöhlker. Preparation of the 1s lamb shift measurement in U^{91+}: Experimental setup. In D. Seipt and A. Klenke, editors, *Helmholtz Institute Jena annual report 2020*, page 57. Helmholtz Institute Jena and GSI

Helmholtzzentrum für Schwerionenforschung GmbH, 2021. doi:10.15120/GSI-2021-00839.

[245] S. Allgeier. *Entwicklung und Charakterisierung des metallischen magnetischen Kalorimeterarrays maXs100 zur Röntgenspektroskopie von heliumartigen U^{90+}-Ionen*. PhD thesis, Ruperto-Carola-University of Heidelberg, Germany, 2024. URL `https://archiv.ub.uni-heidelberg.de/volltextserver/35586/`.

[246] Struck Innovative Systeme. Struck SIS3316 16 channel VME digitizer family. URL `https://www.struck.de/sis3316.html`. [Accessed on: 14.05.2024].

[247] N. Kurz and J. Adamczewski-Musch. Multi Branch System (MBS) (online). URL `https://www.gsi.de/en/work/research/experiment_electronics/data_processing/data_acquisition/mbs`. [Accessed on: 14.05.2024].

[248] F. M. Kröger, G. Weber, B. Löher, U. Spillmann, J. Linev, S. Adamczewski-Musch, and Th. Stöhlker. Preparation of the 1s Lamb shift measurement in U^{91+}: Data acquisition and online analysis. In D. Seipt and A. Klenke, editors, *Helmholtz Institute Jena annual report 2020*, page 56. Helmholtz Institute Jena and GSI Helmholtzzentrum für Schwerionenforschung GmbH, 2021. doi:10.15120/GSI-2021-00839.

[249] M. Wiebusch. Design and implementation of a compact analog Constant Fraction Discriminator for high-resolution timing in gamma-ray spectroscopy. *Journal of Instrumentation*, 19(12):C12009, 2024. doi:10.1088/1748-0221/19/12/C12009.

[250] D. A. Gedcke and W. J. McDonald. A constant fraction of pulse height trigger for optimum time resolution. *Nuclear Instruments and Methods*, 55:377–380, 1967. doi:10.1016/0029-554X(67)90145-0.

[251] D. Beck, J. Adamczewski-Musch, J. Bai, R. Bär, J. Frühauf, J. Hoffmann, M. Kreider, N. Kurz, C. Prados, S. Rauch, W. Terpstra, S. Voltz, and M. Zweig. Paving the way for the FAIR general machine timing system. In K. Große, editor, *GSI Scientific Report 2013*, pages 378–379. GSI Helmholtzzentrum für Schwerionenforschung GmbH, 2014. doi:10.15120/GR-2014-1.

[252] N. Kurz, J. Adamczewski-Musch, J. Frühauf, J. Hoffmann, D. Beck, M. Kreider, C. Prados, S. Rauch, W. Terpstra, and M. Zweig. White Rabbit applications for

FAIR experiments. In K. Große, editor, *GSI Scientific Report 2013*, page 380. GSI Helmholtzzentrum für Schwerionenforschung GmbH, 2014. doi:10.15120/GR-2014-1.

[253] B. Löher, A. Charpy, H. T. Johansson, H. Simon, H. T. Törnqvist, the R^{3}B collaboration, and FAIR@GSI division. The DAQ readout library vmelib. In K. Große, editor, *GSI scientific report 2014*, page 192. GSI Helmholtzzentrum für Schwerionenforschung GmbH, 2015. doi:10.15120/GR-2015-1.

[254] H. Simon, H. T. Johansson, A. Charpy, B. Löher, M. Munch, and H. T. Törnqvist. NUstar ReaDout LIBrary - Nurdlib (online). URL `http://web-docs.gsi.de/~land/nurdlib/`. [Accessed on: 15.11.2024].

[255] J. Adamschewski-Musch and S. Linev. The Go4 project page. URL `https://www.gsi.de/en/work/research/experiment_electronics/data_processing/data_analysis/the_go4_home_page`. [Accessed on: 14.05.2024].

[256] B. Zhu. *High resolution for x-ray spectroscopy studies with highly charged heavy ions at the CRYRING@ESR electron cooler*. PhD thesis, Friedrich-Schiller-Universität Jena, 2023. URL `https://nbn-resolving.org/urn:nbn:de:gbv:27-dbt-20230228-143916-003`.

[257] Ph. Pfäfflein, G. Weber, S. Allgeier, S. Bernitt, A. Fleischmann, M. Friedrich, Ch. Hahn, D. Hengstler, M. O. Herdrich, A. Kalinin, F. M. Kröger, P. Kuntz, M. Lestinsky, B. Löher, E. B. Menz, U. Spillmann, B. Zhu, C. Enss, and Th. Stöhlker. Exploitation of the timing capabilities of metallic magnetic calorimeters for a coincidence measurement scheme. *Atoms*, 11(1):5, 2023. doi:10.3390/atoms11010005.

[258] V. I. Stoica. *Digital pulse-shape analysis and controls for advanced detector systems*. PhD thesis, University of Groningen, Netherlands, 2012. URL `https://research.rug.nl/en/publications/digital-pulse-shape-analysis-and-controls-for-advanced-detector-s`.

[259] A. Georgiev, W. Gast, and R. M. Lieder. An analog-to-digital conversion based on a moving window deconvolution. *IEEE Transactions on Nuclear Science*, 41 (4):1116–1124, 1994. doi:10.1109/23.322868.

[260] M. Kavatsyuk, D. Bremer, V. Dormenev, P. Drexler, T. Eissner, W. Erni, E. Guliyev, T. Hennino, B. Krusche, B. Lewandowski, H. Löhner, M. Moritz, R. W. Novotny, K. Peters, J. Pouthas, P. Rosier, M. Steinacher, G. Tambave, and A. Wilms. Performance of the prototype of the electromagnetic calorimeter for PANDA. *Nuclear Instruments and Methods in Physics Research Section A: Accelerators, Spectrometers, Detectors and Associated Equipment*, 648(1):77–91, 2011. doi:10.1016/j.nima.2011.06.044.

[261] A. I. Bondarev. Private communication, 2025.

[262] N. K. Dulaev, M. Y. Kaygorodov, A. V. Malyshev, I. I. Tupitsyn, and V. M. Shabaev. Relativistic calculations of the energies of the low-lying 1sns, 1snp, 1snd states and the probabilities of the one-photon 1snl $\rightarrow$ 1s$n'l'$ transitions in heliumlike uranium. *Optics and Spectroscopy*, 131(3):283–290, 2023. doi:10.61011/EOS.2023.03.56178.4569-22.

[263] A. I. Bondarev. Private communication, 2023.

[264] V. M. Shabaev. Private communication, 2021.

[265] A. V. Volotka, A. Surzhykov, V. M. Shabaev, and G. Plunien. Interelectronic-interaction effects on the two-photon decay rates of heavy He-like ions. *Physical Review A*, 83(6):062508, 2011. doi:10.1103/PhysRevA.83.062508.

[266] L. N. Labzowsky and A. V. Shonin. QED theory of cascades and two-photon transitions and calculation of the $E1 - M1$ transition probability in two-electron highly charged ions. *Physical Review A*, 69(1):012503, 2004. doi:10.1103/PhysRevA.69.012503.

[267] H. Dembinski, P. Ongmongkolkul, C. Deil, D. Menéndez Hurtado, H. Schreiner, M. Feickert, Andrew, C. Burr, J. Watson, F. Rost, A. Pearce, L. Geiger, B. M. Wiedemann, C. Gohlke, Gonzalo, J. Drotleff, J. Eschle, L. Neste, M. E. Gorelli, M. Baak, O. Zapata, and odidev. scikit-hep/iminuit: v2.8.4, 2021. URL `https://zenodo.org/records/5561211`.

[268] H. Dembinski and the iminuit team. 'iminuit' [online]. URL `https://scikit-hep.org/iminuit`. [Accessed on: 16.06.2021].

[269] M. Hatlo, F. James, P. Mato, L. Moneta, M. Winkler, and A. Zsenei. Developments of mathematical software libraries for the LHC experiments. *IEEE Transactions on Nuclear Science*, 52(6):2818–2822, 2005. doi:10.1109/TNS.2005.860152.

[270] F. James and M. Roos. Minuit: A system for function minimization and analysis of the parameter errors and correlations. *Computer Physics Communications*, 10 (6):343–367, 1975. doi:10.1016/0010-4655(75)90039-9.

[271] R. Barlow. Extended maximum likelihood. *Nuclear Instruments and Methods in Physics Research Section A: Accelerators, Spectrometers, Detectors and Associated Equipment*, 297(3):496–506, 1990. doi:10.1016/0168-9002(90)91334-8.

[272] S. Fritzsche, A. Surzhykov, and Th. Stöhlker. Radiative recombination into high-Z few-electron ions: Cross sections and angular distributions. *Physical Review A*, 72(1):012704, 2005. doi:10.1103/PhysRevA.72.012704.

[273] M. F. Gu. Indirect x-ray line-formation processes in iron L-shell ions. *The Astrophysical Journal*, 582(2):1241, 2003. doi:10.1086/344745.

[274] M. F. Gu. The flexible atomic code. *Canadian Journal of Physics*, 86(5):675–689, 2008. doi:10.1139/p07-197.

Statutory Declaration

I hereby solemnly declare that:

1. I have independently prepared and completed the submitted work,
2. without undue assistance from third parties or the use of references not acknowledged in the bibliography of this thesis.
3. Data and ideas which were included directly or indirectly from other sources are cited by referencing the original source.
4. The individuals listed in the acknowledgements supported me in the manner described there. No other individuals were involved in the preparation of this thesis with respect to its content and materials.
5. In particular, I did not receive paid assistance or consulting services from PhD consultants or any other individuals.
6. Nobody has received direct or indirect monetary benefits for work associated with the content of this thesis.
7. This work has not been submitted in its current or any similar form to another examination board.
8. I am aware of the regulations for Doctoral Studies at the Faculty of Physics and Astronomy.

I declare that I have told the truth to the best of my knowledge and understanding and have not concealed anything.

Place, Date	Felix Martin Kröger

Acknowledgements

I want to express my sincere gratitude to all who supported me during my PhD work and thesis, in particular to:

- Prof. Dr. Thomas Stöhlker, my doctor father, who had the idea of this work, supervised my scientific endeavors, supported me in my publications and my thesis and my working contracts, and gave me the opportunity to work with great teams and people at several scientific projects. He also always showed sympathy and humanity towards his students and staff, which was especially important in times of the Corona crisis.
- Dr. Uwe Spillmann, who taught me patiently about data acquisition systems, scientific working and many things going beyond physics, supervised my scientific work in several projects at GSI, and was always a sturdy lighthouse when the experimental weather became stormy.
- Dr. Günter Weber, who supervised me in the experiment preparations and in the data analysis in Jena, taught me a lot about atomic physics, and was a diligent proofreader of my publications and my thesis, as well as a patient listener when I had any physics related questions.
- Thomas Köhler, who taught me the use of CAD software, approved my model of the window chambers, and helped in the coordination with the IOQ workshop.
- Dr. Marc Oliver Herdrich, and Philip Pfäfflein for co-working in the experiment, especially in regards to the raw data analysis, for proofreading my thesis, and for the lively discussions about physical topics.
- Dr. Andrey Bondarev for proofreading parts of my thesis and for providing me, via private communication, like Prof. Dr. V. M. Shabaev, and Dr. Binghui Zhu, with theoretical values which I could use in my analysis, or for the comparison of the experimental data (cited at the relevant places).
- Dr. Sonja Bernitt, Dr. Alexandre Gumberidze, Dr. Anna Majorova, Dr. Daniel Hengstler for proofreading different sections of my thesis, corresponding to their respective expertise.

- All people mentioned above, as well as Dr. Bastian Löher, Dr. Michael Lestinsky, Dr. Sergiy Trotsenko, Dr. Esther Menz, Dr. Oliver Forstner, Wilko Middents, and all other colleagues and work associates, engineers, and beam operators at the HI Jena, IOQ Jena, GSI and of the University in Heidelberg, as well as all external colleagues, who were involved in conducting the experiment. I want to highlight, that the presented experiment was a team effort, which only succeeded due to capable cooperation and coordination of all who were involved.

- Christoph Hahn, Janett Flegel, Sarah Dürer, Jessica Hopfe-Reuter, Lea Wunderlich and all other involved secretary staff at HI Jena, at GSI, and at the Friedrich-Schiller University Jena for their organisational support and patience.

- My family: my sister for proof-reading my thesis, for emotional support, and for teaching me how to walk. My brother for the emotional support, his calm grounding demeanor, and for teaching me patience. My parents for raising me, teaching me correct values, supporting me, and for their love. And my grandparents for their faith in me. You are dear to my heart.

- My friends, especially Alexander, Andy, Florian, Gilles, Guy, Maximilian, Mich, Michel, Marcel, for their friendship, understanding and trust, and emotional support no matter how far apart.

- Special thanks to Dr. S. Hutchinson and Dr. G. Peickert and Dr. A. Lindner for their motivational support, as well as in general to all teachers that taught me what I know today, and to all doctors that took care of my health and well-being, as well as my health care provider and the university and health care systems, which I do not take for granted.

List of peer reviewed publications

- Ph. Pfäfflein, G. Weber, S. Allgeier, Z. Andelkovic, S. Bernitt, A. I. Bondarev, A. Borovik Jr., L. Duval, A. Fleischmann, O. Forstner, M. Friedrich, J. Glorius, A. Gumberidze, Ch. Hahn, F. Herfurth, D. Hengstler, M. O. Herdrich, P.-M. Hillenbrand, A. Kalinin, M. Kiffer, **F. M. Kröger**, et al.. Quantum electrodynamics in strong electromagnetic fields: Substate resolved Kα transition energies in heliumlike uranium. *Physical Review Letters*, 134(15):153001, 2025. doi:10.1103/PhysRevLett.134.153001.

- R. Loetzsch, H. F. Beyer, L. Duval, U. Spillmann, D. Banaś, P. Dergham, **F. M. Kröger** et al.. Testing quantum electrodynamics in extreme fields using heliumlike uranium. *Nature*, 625(7996):673–678, 2024. doi:10.1038/s41586-023-06910-y.

- **F. M. Kröger**, G. Weber, S. Allgeier, Z. Andelkovic, S. Bernitt, A. Borovik Jr. et al.. Towards an intrinsic Doppler correction for x-ray spectroscopy of stored ions at CRYRING@ESR. *Atoms*, 11(2):22, 2023. doi:10.3390/atoms11020022.

- Ph. Pfäfflein, G. Weber, S. Allgeier, S. Bernitt, A. Fleischmann, M. Friedrich, Ch. Hahn, D. Hengstler, M. O. Herdrich, A. Kalinin, **F. M. Kröger** et al.. Exploitation of the timing capabilities of metallic magnetic calorimeters for a coincidence measurement scheme. *Atoms*, 11(1):5, 2023. doi:10.3390/atoms11010005.

- B. Zhu, A. Gumberidze, T. Over, G. Weber, Z. Andelkovic, A. Bräuning-Demian, R. J. Chen, D. Dmytriiev, O. Forstner, Ch. Hahn, F. Herfurth, M. O. Herdrich, P.-M. Hillenbrand, A. Kalinin, **F. M. Kröger** et al.. X-ray emission associated with radiative recombination for Pb^{82+} ions at threshold energies. *Physical Review A*, 105(5):052804, 2022. doi:10.1103/PhysRevA.105.052804.

- Ph. Pfäfflein, S. Allgeier, S. Bernitt, A. Fleischmann, M. Friedrich, Ch. Hahn, D. Hengstler, M. O. Herdrich, A. Kalinin, **F. M. Kröger** et al.. Integration of maXs-type microcalorimeter detectors for high-resolution x-ray spectroscopy into the experimental environment at the CRYRING@ESR electron cooler. *Physica Scripta*, 97(11):114005, 2022. doi:10.1088/1402-4896/ac93be.

- **F. M. Kröger**, G. Weber, S. Hirlaender, R. Alemany-Fernandez, M. W. Krasny, Th. Stöhlker, I. Y. Tolstikhina, V. P. Shevelko. Charge-State Distributions of

highly charged lead ions at relativistic collision energies. *Annalen der Physik*, 534(3):2100245, 2022. doi:10.1002/andp.202100245.

- **F. M. Kröger**, G. Weber, M. O. Herdrich, J. Glorius, C. Langer, Z. Slavkovská, L. Bott, C. Brandau et al.. Electron capture of Xe^{54+} in collisions with H_2 molecules in the energy range between 5.5 and 30.9 MeV/u. *Physical Review A*, 102(4):042825, 2020. doi:PhysRevA.102.042825.

- **F. M. Kröger**, G. Weber, V. P. Shevelko, S. Hirlaender, M. W. Krasny, Th. Stöhlker. Charge state tailoring of relativistic heavy ion beams for the Gamma Factory project at CERN. *X-Ray Spectrometry*, 49(1):25, 2020. doi:10.1002/xrs.3039.

For more information see **ORCID ID:** 0000-0002-1633-8044.